

(12) LEVEL II

AD-E300 884P

AD A088368

**HIGH EXPLOSIVE SIMULATION OF  
A NUCLEAR SURFACE BURST.**

**A Feasibility Study.**

Physics International Company  
2700 Merced Street  
San Leandro, California 94577

30 Jun 1979

Final Report Period 1 Mar 1977-30 Jun 1979.

CONTRACT No/ DNA 001-77-C-0150

APPROVED FOR PUBLIC RELEASE;  
DISTRIBUTION UNLIMITED.

THIS WORK SPONSORED BY THE DEFENSE NUCLEAR AGENCY  
UNDER RDT&E RMSS CODE B344077464 Y99QAXSP07035 H2590D.

Prepared for  
Director  
DEFENSE NUCLEAR AGENCY  
Washington, D. C. 20305

DTIC  
ELECTE  
AUG 27 1980

B

80 8 13 070

Destroy this report when it is no longer needed. Do not return to sender.

PLEASE NOTIFY THE DEFENSE NUCLEAR AGENCY,  
ATTN: TISI, WASHINGTON, D.C. 20305, IF  
YOUR ADDRESS IS INCORRECT, IF YOU WISH TO  
BE DELETED FROM THE DISTRIBUTION LIST, OR  
IF THE ADDRESSEE IS NO LONGER EMPLOYED BY  
YOUR ORGANIZATION.



UNCLASSIFIED

SECURITY CLASSIFICATION OF THIS PAGE (When Data Entered)

| REPORT DOCUMENTATION PAGE  |                       | READ INSTRUCTIONS<br>BEFORE COMPLETING FORM  |
|--|-----------------------|--|
| 1. REPORT NUMBER<br>DNA 5016F ✓  | 2. GOVT ACCESSION NO. | 3. RECIPIENT'S CATALOG NUMBER  |
| 4. TITLE (and Subtitle)<br>HIGH EXPLOSIVE SIMULATION OF A NUCLEAR<br>SURFACE BURST<br>A Feasibility Study  |                       | 5. TYPE OF REPORT & PERIOD COVERED<br>Final Report for Period<br>1 Mar 77-30 Jun 79          |
| 7. AUTHOR(s)<br>J. M. Thomsen<br>R. H. Franzen<br>D. L. Orphal   |                       | 6. PERFORMING ORG. REPORT NUMBER<br>PIFR-1035 (DNA 5016F)                                    |
| 9. PERFORMING ORGANIZATION NAME AND ADDRESS<br>Physics International Company ✓<br>2700 Merced Street<br>San Leandro, California 94577  |                       | 8. CONTRACT OR GRANT NUMBER(s)<br><br>DNA 001-77-C-0150 ✓                                    |
| 11. CONTROLLING OFFICE NAME AND ADDRESS<br>Director<br>Defense Nuclear Agency<br>Washington, D.C. 20305  |                       | 10. PROGRAM ELEMENT, PROJECT, TASK<br>AREA & WORK UNIT NUMBERS<br><br>Subtask Y99QAXSD070-35 |
| 14. MONITORING AGENCY NAME & ADDRESS (if different from Controlling Office)  |                       | 12. REPORT DATE<br>30 June 1979  |
|  |                       | 13. NUMBER OF PAGES<br>206   |
|  |                       | 15. SECURITY CLASS (of this report)<br><br>UNCLASSIFIED                                      |
|  |                       | 15a. DECLASSIFICATION DOWNGRADING<br>SCHEDULE  |
| 16. DISTRIBUTION STATEMENT (of this Report)<br><br>Approved for public release; distribution unlimited.  |                       |  |
| 17. DISTRIBUTION STATEMENT (of the abstract entered in Block 20, if different from Report)   |                       |  |
| 18. SUPPLEMENTARY NOTES<br>This work sponsored by the Defense Nuclear Agency under RDT&E RMSS Code<br>B344077464 Y99QAXSD07035 H2590D.   |                       |  |
| 19. KEY WORDS (Continue on reverse side if necessary and identify by block number)<br>ANFO Experiments                      Explosive Effects<br>Nuclear Effects Simulation           Mine Throw Technique<br>Airblast                                  Airblast Induced Motions<br>Ground Coupling                        Computer Calculations   |                       |  |
| 20. ABSTRACT (Continue on reverse side if necessary and identify by block number)<br>✓ The feasibility of designing and constructing a high explosive source which faithfully reproduces the direct- and airblast-induced ground motions resulting from a 1-kt nuclear surface burst has been investigated. A preliminary charge design incorporating subsurface and surface high explosive charges was developed, and shown to theoretically reproduce the desired simulation conditions. The subsurface charge employs techniques first used in the MINE THROW I simulation of the JOHNIE BOY nuclear event. The surface charge → <i>see v</i> |                       |  |

DD FORM 1 JAN 73 1473

EDITION OF 1 NOV 65 IS OBSOLETE

UNCLASSIFIED

SECURITY CLASSIFICATION OF THIS PAGE (When Data Entered)

UNCLASSIFIED

SECURITY CLASSIFICATION OF THIS PAGE(When Data Entered)

20. ABSTRACT (Continued)

consists of an elevated disc of explosive (ANFO) with a thickness varying from 1 m to 0.1 m with a total diameter of about 40 m. Detonation spacings and an initiation system for this novel charge design were investigated. A complete fieldable charge was not constructed because of difficulties in experimentally determining the detonation properties of thin sheets of ANFO. Steps leading to a future fieldable charge which simulate airblast, ground motion, and cratering effects of a 1-kt nuclear surface burst are made, based on the results of this initial effort.

↑

UNCLASSIFIED

SECURITY CLASSIFICATION OF THIS PAGE(When Data Entered)

## PREFACE

The work in this report was performed from January, 1977 to October 1978 under contract to the Strategic Structures Division (SPSS) of the Defense Nuclear Agency. The contract was monitored first by Major George Goss and later by CDR Thomas Deevy.

The authors wish to thank the following Physics International personnel for their participation in this multifaceted program: C. Vincent, J. Kochly, P. Cayere, B. Drake, F. Milistefr and R. Funston for instrumentation support, P. Vigil for Tracy Test Site support, K. Abbott, R. Brown, S. Hancock and S. Ruhl for calculational support, and F. Sauer for providing technical direction and review of the final report.

|                                 |               |  |
|---------------------------------|---------------|--|
| ACCESSION for                   |               |  |
| NTIS                            | White Section | <input checked="checked" type="checkbox"/> |
| DDC                             | Buff Section  | <input type="checkbox"/>                   |
| UNANNOUNCED                     |               | <input type="checkbox"/>                   |
| JUSTIFICATION _____             |               |  |
| BY _____                        |               |  |
| DISTRIBUTION/AVAILABILITY CODES |               |  |
| Dist.                           | AVAIL.        | and/or SPECIAL                             |
| A                               |               |  |

# TABLE OF CONTENTS

|  | <u>Page</u> |
|--|-------------|
| Preface  |             |
| List of Illustrations  | 3           |
| List of Tables   | 8           |
| SECTION 1 INTRODUCTION   | 11          |
| SECTION 2 SURFACE CHARGE CONCEPT AND PRELIMINARY INVESTIGATION                               | 18          |
| 2.1 Brief Description of the Charge Design Process   | 19          |
| 2.2 Results of the Preliminary Investigation   | 21          |
| 2.3 Summary of Key Unknowns  | 61          |
| SECTION 3 FURTHER INVESTIGATION OF TECHNICAL FEASIBILITY                                     | 63          |
| 3.1 Early Thin ANFO Investigation  | 63          |
| 3.2 Final Thin ANFO Experiment   | 92          |
| 3.3 Initiation System  | 114         |
| 3.4 Low Overpressure Airblast Characteristics  | 119         |
| SECTION 4 HE SIMULATION OF DIRECTLY COUPLED ENERGY FROM A NUCLEAR EVENT                      | 132         |
| 4.1 Two-dimensional Calculation of JANGLE S  | 132         |
| 4.2 HE Simulation of Direct- and Cratering-induced Ground Motions                            | 158         |
| SECTION 5 SUMMARY AND RECOMMENDATIONS  | 168         |
| REFERENCES   | 171         |
| APPENDIX OVERPRESSURE WAVEFORMS AND OVERPRESSURE IMPULSE FROM STANDARD SOURCE AIRBLAST TESTS | 173         |

## LIST OF ILLUSTRATIONS

| <u>Figure</u> |   | <u>Page</u> |
|---------------|---|-------------|
| 1-1           | High Explosive Simulation of Nuclear Detonations  | 12          |
| 1-2           | MINE THROW I--Direct- and Cratering-induced Ground Motion, Cratering, and Ejecta                        | 14          |
| 1-3           | Concept for Applying the Close-in Airblast Overpressures to the Ground                                  | 16          |
| 2-1           | HE Results Required for Surface Charge Design from Experiments and/or Calculations                      | 20          |
| 2-2           | General Calculational Geometry for Standard Source One-dimensional HE Calculations using Plane Symmetry | 23          |
| 2-3           | Peak Pressure versus V/A from One-dimensional ANFO Calculations   | 26          |
| 2-4           | Total Impulse Delivered to the Ground versus A (V=0) (from one-dimensional calculations)                | 28          |
| 2-5           | Closure Time, TOA', versus V from One-dimensional Standard Source Calculations (ANFO/VOID/RIGID Boundry | 30          |
| 2-6           | ANFO Air Shock TOA in Air from One-dimensional Calculation  | 31          |
| 2-7           | Airblast Peak Pressure versus Range from a 1-kt Nuclear Surface Burst                                   | 33          |
| 2-8           | Airblast Time-of-arrival for 1-kt Nuclear Surface Burst   | 34          |
| 2-9           | Airblast Impulse versus Range from a 1-kt Nuclear Surface Burst   | 35          |
| 2-10          | Detonation Trajectory for Undiluted 94/6 ANFO   | 38          |
| 2-11          | Explosive Thickness versus Range, Charge Design 1A  | 40          |

| <u>Figure</u> |   | <u>Page</u> |
|---------------|---|-------------|
| 2-12          | Standard Source Charge Design 1A (note expanded vertical scale)   | 41          |
| 2-13          | Charge Design 1A  | 43          |
| 2-14          | Initiation Time versus Range, Charge Design 1A  | 44          |
| 2-15          | Calculations Examining Infinite and 3(A+V) Detonator Spacing; Peak Pressure at Ground Surface versus Range  | 47          |
| 2-16          | Calculations Examining Infinite, 1(A+V) and 2(A+V) Detonator Spacing; Peak Pressure at Ground Surface versus Range  | 48          |
| 2-17          | Effect of Detonator Spacing on Impulse, Spacing = 2(A+V), Calculation No. 3   | 49          |
| 2-18          | Concept of Initiation Geometry  | 51          |
| 2-19          | Two-dimensional Charge Performance Calculation; Computed Time-of-arrival at the Ground Surface versus Range compared with 1-kt Nuclear Time-of-arrival            | 54          |
| 2-20          | Two-dimensional Charge Performance Calculation; Computed Overpressure versus Range at the Ground Surface compared with 1-kt Nuclear Overpressures                 | 55          |
| 2-21          | Two-dimensional Charge Performance Calculation; Computed Total Impulse versus Range at the Ground Surface at Five Times, compared with Total 1-kt Nuclear Impulse | 56          |
| 2-22          | Typical Panel for Supporting ANFO   | 59          |
| 2-23          | Conceptual Layout of Standard Source Charge   | 60          |
| 3-1           | Thin Film ANFO with TOA Pins and Booster  | 65          |
| 3-2           | Instrumented Witness Plate, Shot 23   | 67          |
| 3-3           | Ionization Pin System   | 69          |
| 3-4           | Time-of-arrival Pin System  | 70          |
| 3-5           | P.C.B. Pressure Recording System  | 71          |
| 3-6           | Carbon Stress Gage Recording System   | 72          |
| 3-7           | Calibration Curves for Copper Crush Balls   | 74          |



| <u>Figure</u> |   | <u>Page</u> |
|---------------|---|-------------|
| 3-8           | Experimental Setup, Shot 13   | 75          |
| 3-9           | Propagation Velocity in ANFO versus Distance from Booster, Tests 4, 5, and 6                          | 78          |
| 3-10          | Detonation Velocity in ANFO versus Distance from Booster, Tests 7-11                                  | 80          |
| 3-11          | Detonation Velocity in ANFO Charge, Tests 16B and 16C (aluminized ANFO)                               | 85          |
| 3-12          | Detonation Velocity in ANFO versus Distance from Booster, Tests 21, 22, and 24                        | 86          |
| 3-13          | TOA Data from Pins on and above the Segmented Aluminum Plate, Test 25                                 | 88          |
| 3-14          | Geometries for Thin ANFO Calculations   | 91          |
| 3-15          | Side-on Photograph of the Setup of the Final Thin ANFO Experiment                                     | 93          |
| 3-16          | Final Thin ANFO Segmented Aluminum Plate  | 94          |
| 3-17          | Standard Source Background Grid   | 96          |
| 3-18          | Fast Camera Frame 1 ( $t=0 \mu s$ ) Side-on Setup View of Thin ANFO, Test 26                          | 98          |
| 3-19          | Fast Camera, Frame 6 ( $t=150 \mu s$ ) Showing Early Spherical Expansion of ANFO Detonation Products  | 99          |
| 3-20          | Fast Camera Frame 8 ( $t=200 \mu s$ )   | 100         |
| 3-21          | Fast Camera Frame 11 ( $t=275 \mu s$ ) Showing Initial Formation of Mach Stem along Aluminum Plate    | 102         |
| 3-22          | Fast Camera Frame 14 ( $t=350 \mu s$ ), Showing Further Mach Stem Development beneath the ANFO Charge | 103         |
| 3-23          | Fast Camera Frame 16 ( $t=400 \mu s$ )  | 104         |
| 3-24          | TOA versus Range in Thin ANFO Test 26   | 107         |
| 3-25          | TOA in ANFO Test 26 (average of three pin lines)  | 108         |
| 3-26          | Comparison of Average ANFO Pin Data in Charge with Data from Framing Camera Photographs               | 110         |

| <u>Figure</u> |  | <u>Page</u> |
|---------------|--|-------------|
| 3-27          | Data Digitized from Framing Camera Photos along Lines 3 and 4, near the Aluminum Plate   | 111         |
| 3-28          | Comparison of Gage and Framing Camera TOA Data near the Aluminum Plate   | 112         |
| 3-29          | Concept of Initiation Geometry   | 115         |
| 3-30          | Initiation System Test Layout  | 117         |
| 3-31          | Design of Model Standard Source Surface Charge Using Layers of EL506C-1 Sheet Explosive  | 122         |
| 3-32          | Model Standard Source Charge, Test 19  | 123         |
| 3-33          | Comparison of Test 18 and Test 19 Measured Peak Overpressures with Predictions   | 129         |
| 3-34          | Comparison of Expected and Measured Positive Phase Impulse ( $I^+$ ), Tests 18 and 19  | 130         |
| 4-1           | Initial Geometry and Euler Zoning for JANGLE S 2DELK Calculation   | 134         |
| 4-2           | Shock Arrival Time in the Vicinity of the JANGLE S Nuclear Source, Based on One-dimensional Calculations                                     | 137         |
| 4-3           | Initial Coupled Lagrange/Euler Grid for the JANGLE S 2DELK Calculation   | 140         |
| 4-4           | Schematic of CIST-15 Hydrostat   | 143         |
| 4-5           | Schematic of CIST-15 Yield Surface   | 146         |
| 4-6           | CIST-15 Hydrostatic Compressibility Curve  | 148         |
| 4-7           | Comparison of CIST-5 and CIST-15 Compressibility Curves  | 150         |
| 4-8           | PICES 2DELK Vector Velocity and Material Boundary Plot from JANGLE S Calculation   | 152         |
| 4-9           | The Intersection of the Hugoniot Curves for the CIST-15 Soil and ANFO Yields a Pressure of 7.2 GPa for the Reflection of the Detonation Wave | 154         |
| 4-10          | The 7.2 GPa Contour for the Nuclear Source Calculation   | 155         |

| <u>Figure</u> |   | <u>Page</u> |
|---------------|---|-------------|
| 4-11          | Arrival Time and Impulse along Smoothed 7.2 GPa Contour from JANGLE S Nuclear Source Calculation                      | 156         |
| 4-12          | Geometry of Design 1  | 159         |
| 4-13          | Comparison of the Impulse for Designs 1, 2, 3, and 4 with the Desired Impulse Curve                                   | 160         |
| 4-14          | Geometry of Design 2  | 162         |
| 4-15          | Geometry of Design 3  | 163         |
| 4-16          | Comparison of the Impulse versus Time Curves for the Nuclear Source Calculation and Design 3 on the Axis of Symmetry  | 164         |
| 4-17          | Comparison of the Impulse versus Time Curves for the Nuclear Source Calculation and Design 3 at $\theta = 70$ degrees | 165         |
| 4-18          | Geometry of Design 4  | 167         |

## LIST OF TABLES

| <u>Table</u> |   | <u>Page</u> |
|--------------|---|-------------|
| 2-1          | JWL Parameters for Ideal ANFO   | 22          |
| 2-2          | Results of Standard Source One-dimensional Calculations                           | 24          |
| 2-3          | Table of 1-kt Nuclear Airblast Conditions to a Range of 25 m                      | 36          |
| 2-4          | Summary of Two-dimensional Detonator Spacing Calculations Performed               | 46          |
| 2-5          | Standard Source Detonator and Booster Timing                                      | 52          |
| 3-1          | Thin ANFO Experiments - Summary Table   | 76          |
| 3-2          | Copper Crush Gage Results: Test 13  | 82          |
| 3-3          | Copper Crush Gage Results: Test 15 (Diluted Nitromethane)                         | 82          |
| 3-4          | Time-of-arrival in Test 26, Data from Fast Camera Photographs                     | 105         |
| 3-5          | TOA Pin Data in Thin ANFO, Test 26  | 106         |
| 3-6          | Summary of TOA Measurements On and Near the Segmented Aluminum Plate, Test 26     | 113         |
| 3-7          | Data Summary Initiation System Tests  | 118         |
| 3-8          | Dimensions and Design of the Scale Model Standard Source Surface Charge (Test 19) | 121         |
| 3-9          | Experiment Plan for Tests 18 and 19   | 125         |
| 3-10         | Experiment Plan for Test 20   | 126         |
| 3-11         | Summary Results for 10.5 kg Nitromethane Charge (Test 18)                         | 127         |

| <u>Table</u> |   | <u>Page</u> |
|--------------|---|-------------|
| 3-12         | Summary Results for 10.5 kg Model Charge (Test 19)                                    | 128         |
| 4-1          | Initial Conditions for Materials in JANGLE S Calculation                              | 136         |
| 4-2          | Summary of Euler Rezones Performed in the 2DELK JANGLE S Calculation                  | 139         |
| 4-3          | CIST Model Constants for Event 15, Used to Describe the Alluvium at the JANGLE S Site | 147         |
| 4-4          | Coordinates, Impulse, and Arrival Time along the Smoothed 7.2 GPa Contour - JANGLE S  | 157         |

## SECTION 1

### INTRODUCTION

Since the advent of the Atmospheric Nuclear Test Ban Treaty, the Defense Nuclear Agency and the Armed Service Laboratories have relied on chemical explosives as energy sources for the proof testing of structures and military equipment against the nuclear airblast and ground shock environment. The phenomenological investigation of nuclear effects, especially investigations concerning cratering and ground motion, have also relied upon chemical explosives to simulate the nuclear source. In both usages, simulation implies replication of only the nuclear effects of interest. This is illustrated in Figure 1-1. How well high explosive (HE) simulation sources replicate the airblast from nuclear weapons can be readily evaluated since considerable data exist for atmospheric nuclear tests made prior to the Nuclear Test Ban Treaty. In addition, both high explosive and nuclear airblast effects have been studied calculationaly in considerable detail.

In May 1970, Physics International Company (PI) proposed a method of using chemical explosives to reproduce the crater, ejecta, and the cratering related and direct-induced ground motions of a nuclear near-surface burst. This method became known as the MINE THROW technique.

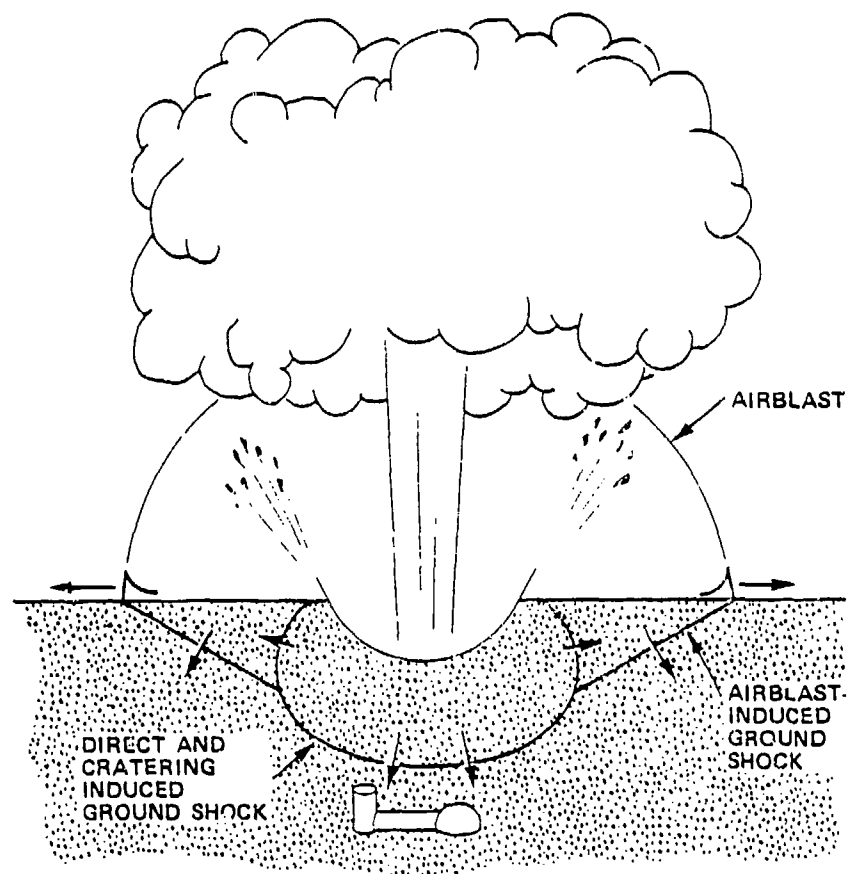


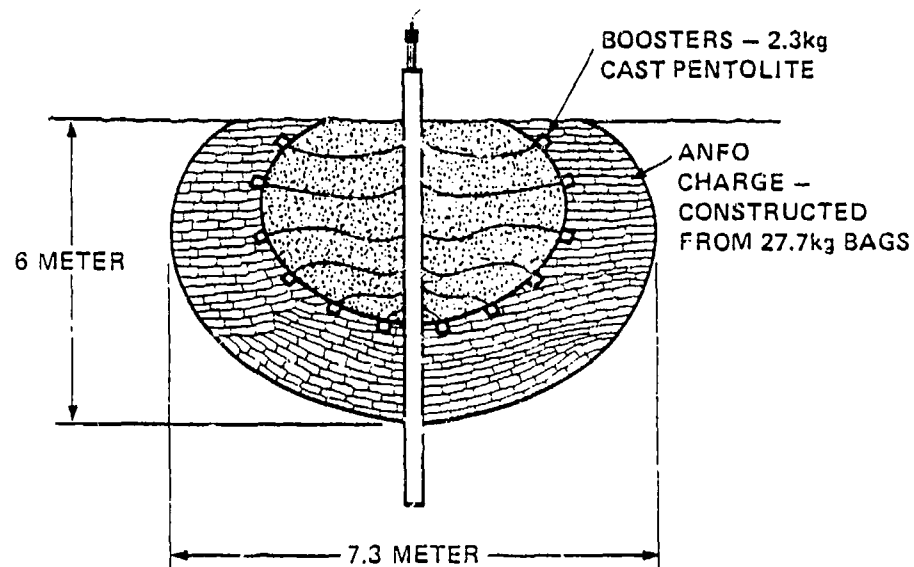
Figure 1-1 High explosive simulation of nuclear detonations.

The first test of this technique was the MINE THROW I event. This event had as its objective the reproduction of the crater and the cratering-related ground motions produced by the JOHNNIE BOY nuclear event, a 500 ton nuclear explosion buried at 58.5 cm in Area 18 alluvium at the Nevada Test Site. No attempt was made to match the JOHNNIE BOY airblast environment on MINE THROW I because the coupled airblast energy did not appear to be significant. It was postulated that the crater formation for this event was dominated by the direct-induced motions and would not be severely influenced by the difference in airblast between the JOHNNIE BOY event and MINE THROW I.

The specific technique for designing the MINE THROW I experiment was as follows: The contour of constant peak pressure corresponding to the detonation pressure of the explosive used was obtained from the finite difference calculations of the JOHNNIE BOY event. At each point along that contour, both the pressure as a function of time,  $P(t)$ , and the time integral of  $P(t)$ , or specific impulse, were determined from these calculations. An explosive charge was then shaped in such a way that it reproduced the nuclear pressure history (approximately) and the total specific impulse along this contour. In practice, an iterative series of finite difference HE calculations were performed, tailoring the HE to produce the same boundary and initial conditions along the above described contour.

The final charge configuration is shown in Figure 1-2. A comparison of the final craters for MINE THROW I and JOHNNIE BOY showed an agreement in volume and shape within 11 percent. - Although JOHNNIE BOY had only a few ground motion gages, and these





**STATUS:** FULL SCALE FIELD SIMULATION OF 0.5 kt JOHNNIE BOY NUCLEAR EVENT SUCCESSFULLY CONDUCTED ON DECEMBER 15, 1971

**RESULTS:** JOHNNIE BOY DIRECT AND CRATERING-INDUCED GROUND MOTION AND FINAL CRATER WELL SIMULATED. NO ATTEMPT TO SIMULATE AIRBLAST-INDUCED GROUND MOTION

Figure 1-2 MINE THROW I--Direct and cratering-induced ground motion, cratering, and ejecta.

were placed at large radii from the source, the corresponding gages on MINE THROW I showed very similar displacements and ground motion waveforms (Reference 1).

The results show that the MINE THROW technique is a valid technique for reproducing the direct-induced ground motion and cratering resulting from a near surface nuclear burst of a known degree of coupling.

Subsequent to the MINE THROW I experiment, PI performed calculations (Reference 2) on an explosive configuration which would simulate the cratering and the direct-induced ground motion on the CACTUS event, a 17 kt above-surface nuclear explosion at the Pacific Proving Ground. In this case, the relative airblast-induced motions were much larger than for JOHNNIE BOY. It became clear from these calculations that the airblast-induced motions on the horizontal plane added a significant impulse that should be included in the simulation technique. Thus, for target response tests, investigating the the effects of airblast, and airblast-induced ground motions, there are important phenomenological reasons why a standard nuclear simulation technique should include the proper pressure profiles and timing of the close-in airblast.

In March 1976, Physics International Company proposed a method for applying the required close-in airblast loading to the ground surface in conjunction with the MINE THROW technique in order to better simulate the cratering-induced and airblast-induced ground motions. This technique is shown in Figure 1-3. The MINE THROW charge is coupled at its edges to the surface HE

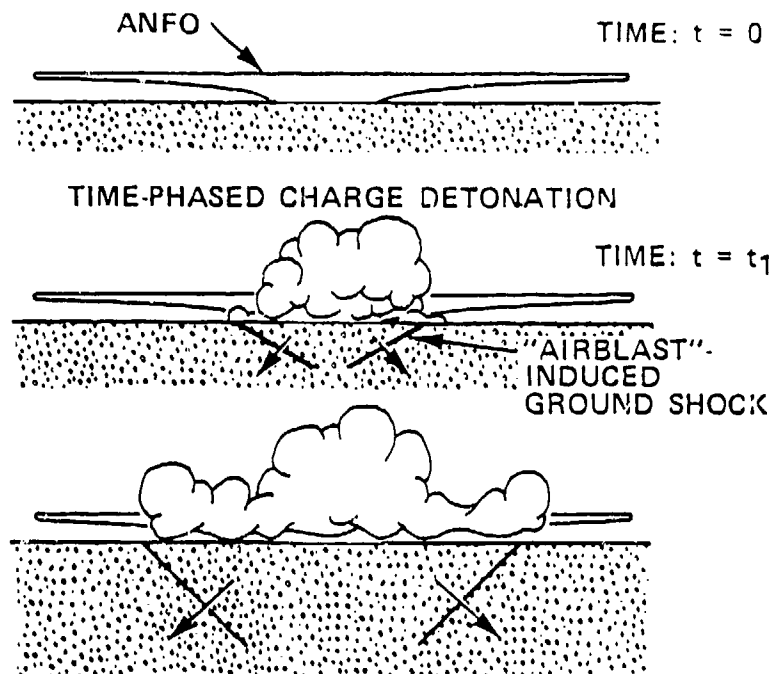


Figure 1-3 Concept for applying the close-in airblast overpressures to the ground.

charge which extends in a thin sheet above the ground surface. The subsurface charge design is accomplished by using the technology developed for MINE THROW I.

The surface charge design required development of a new technology. This effort has been underway for about two years. During that time a series of one- and two-dimensional calculations were performed to establish the design elements such as the explosive thickness, the standoff distance, and initiation pattern for an ANFO surface explosive charge. As a result of that work, a preliminary surface charge design was developed. This work is reported in Section 2.

To design an initial field experiment to test the concept, a follow-on effort was then performed to investigate specific design details. The details of greatest concern are discussed at the end of Section 2, followed by a comprehensive discussion of work performed in Section 3. Also, it was desirable to design the MINE THROW, or subsurface charge for a specific past nuclear event so that this charge could be integrated with the surface charge, simulating the specified nuclear effects of the nuclear event and making it a concept validation test. Work performed in support of this effort is presented in Section 4.

Because of unexpected difficulties in obtaining needed experimental data on the ANFO, it was not possible to develop an improved design for the surface charge. Thus, the full validation test remains to be designed. A summary of work performed, and some recommendations as to how the validation test can be designed are included in Section 5.

## SECTION 2

### SURFACE CHARGE CONCEPT AND PRELIMINARY INVESTIGATION

The surface charge concept is an extension of the MINE THROW design in that it is designed to match specified nuclear effects at a specified contour, or interface. It is specifically desired that a reasonable approximation to the nuclear surface burst airblast at the ground surface be obtained within the region occupied by the final crater. These nuclear effects include:

1. The correct time of arrival of the airblast
2. The correct peak pressure as a function of range
3. The correct impulse as a function of range

It is also desirable, but not required, that the airblast at greater ranges from the ground zero (down to approximately 10 psi) be a reasonable approximation to a nuclear surface burst. This section discusses briefly how the surface charge is designed to meet the above requirements, and the results of a calculational effort which was performed to generate a preliminary design for a 1-kt surface burst.

Since this preliminary design was based entirely on calculations, many important details of the charge design were not specified. These could only be answered by a dedicated experimental program. Section 2.3 reviews the most critical design items which remained after completion of this preliminary investigation.

## 2.1 BRIEF DESCRIPTION OF THE CHARGE DESIGN PROCESS

Nuclear airblast conditions of peak pressure,  $P$ , total impulse,  $I$ , and time of arrival, TOA, along the ground surface are obtained either from nuclear data or from empirical models such as those developed by Brode (Reference 3). For a given yield, the above conditions can be accurately described as functions of range,  $r$ , from the source. These are the conditions which must be matched in the high explosive simulation. It was shown early in the program that these nuclear conditions could be adequately simulated by a "sheet" charge of high explosive located above the ground surface. The radial extent of the sheet, and its thickness and elevation above the ground surface, must be specified. These can be determined, once a particular type of high explosive has been chosen, by calculations and/or experiments.

The required HE results are shown in Figure 2-1, where  $V$  is the distance of the charge above the ground surface, and  $A$  is the total charge thickness. It was shown very early in the program that for a reasonable range of  $V$  and  $A$ , the peak pressure,  $P'$ , could be adequately represented as a function of  $V/A$ , while the impulse,  $I'$ , was directly related to  $A$ . The time of arrival of the airblast wave at the surface, TOA, is directly related to  $V+A$ .

Once these HE results are known, it is a straightforward procedure to develop the basic charge design to accomplish the simulation of the baseline nuclear conditions. By setting

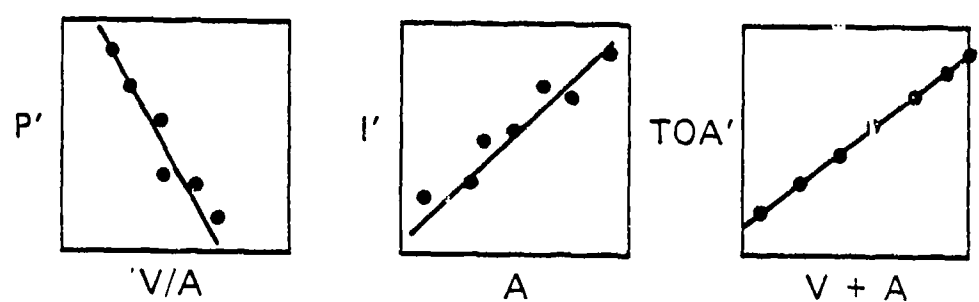


Figure 2-1 HE results required for surface charge design from experiments and/or calculations.

$P' = P$  one is able to obtain  $V/A$  as a function of range, while setting  $I' = I$  gives  $A$  versus range. Knowing both  $V/A$  and  $A$  completely specifies the charge design. What remains is to determine when the HE charge is detonated as a function of range. This is obtained by subtracting  $TOA'$  from  $TOA$ .

Over the intended range of simulation, this procedure will lead to a high explosive charge design which, when executed in the field, will match the close-in airblast from a nuclear detonation at the ground surface. This close-in airblast generates the correct boundary condition for the airblast-induced ground motion, which will vary at different sites because of changes in the subsurface geology.

## 2.2 RESULTS OF THE PRELIMINARY INVESTIGATION

This section shows how the charge design process outlined in Section 2.1 is actually performed. First, the results of some one-dimensional HE calculations and computational analyses are described. These efforts lead to the derivation of the preliminary charge dimensions. Some results from two-dimensional calculations investigating detonator spacing requirements are then presented. A fully two-dimensional calculation using the preliminary charge dimensions and the necessary detonator spacing is then described in detail. Finally, the preliminary STANDARD SOURCE charge design is presented and discussed in detail.

2.2.1 One-Dimensional HE Calculations. This section describes the results of some one-dimensional calculations performed to determine the relationship between the thickness of



the explosive sheet, A, and its standoff distance above the ground surface, V, on the parameters of interest, namely the peak pressure, the total impulse, and the TOA at the ground surface. The explosive considered in these calculations was ANFO.

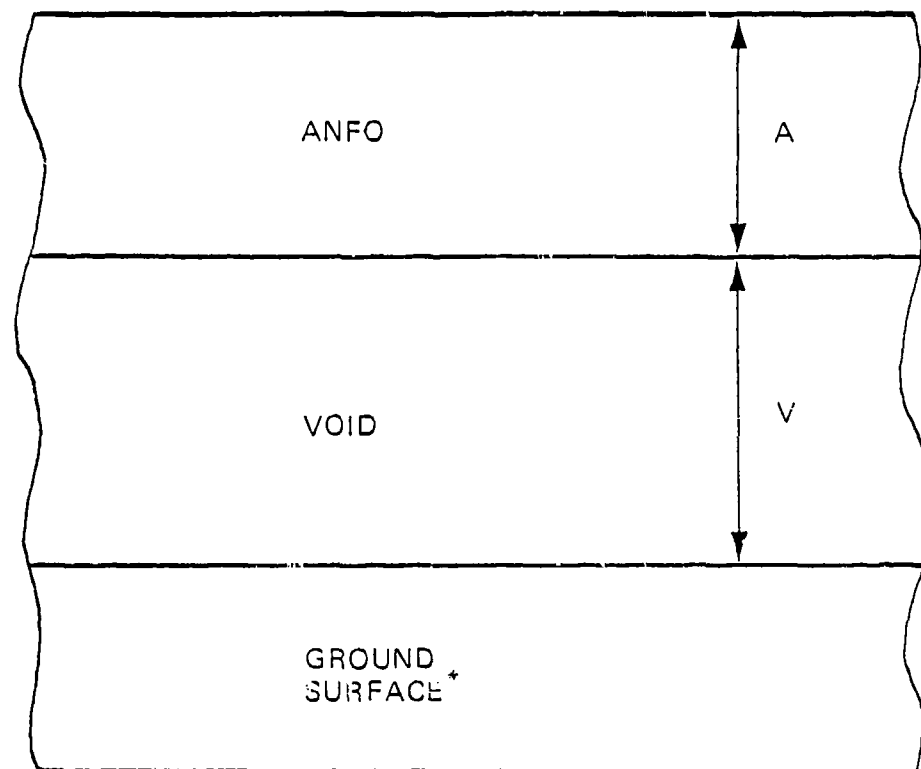
Figure 2-2 shows the general calculational geometry for these calculations. In all cases, the air in the standoff volume was modeled as a void. The ground surface in the calculations was modeled either as a rigid boundary or as an alluvial-type soil. The alluvial soil model used was the CIST-15 model (Reference 4), discussed in detail in Section 4. The ANFO was modeled as an ideal explosive using the JWL high-explosive equation-of-state (Reference 5). The JWL constants used in the calculations are given in Table 2-1 (Reference 6).

TABLE 2-1

JWL PARAMETERS FOR IDEAL ANFO

|          |   |                                    |          |   |           |
|----------|---|------------------------------------|----------|---|-----------|
| $\rho_0$ | = | 0.782 Mg/M <sup>3</sup>            | A        | = | 0.7519    |
| $P_{CJ}$ | = | 5.5 GPa                            | B        | = | -0.008175 |
| D        | = | 5.0 mm/ $\mu$ s                    | $R_1$    | = | 4.1       |
| $E_0$    | = | $2.9 \times 10^9$ J/m <sup>3</sup> | $R_2$    | = | 1.25      |
| $r$      | = | 2.554                              | $\omega$ | = | 0.44      |

Table 2-2 contains a summary of the calculations performed, and the essential results of these calculations in terms of peak pressure  $P'$ , impulse,  $I'$ , and the closure or contact time of the ANFO explosive gases with the ground surface,  $TOA'$ . The ANFO explosive slabs were modeled with three thicknesses: 1 meter,



\* GROUND SURFACE MODELED AS EITHER  
A RIGID BOUNDARY OR AS A SOIL (CIST-15 MODEL)

Figure 2-2 General calculational geometry for standard source one-dimensional HE calculations using plane symmetry.

TABLE 2-2  
RESULTS OF STANDARD SOURCE ONE-DIMENSIONAL CALCULATIONS

| ANFO THICKNESS, A<br>(m) | VOID THICKNESS, V<br>(m) | V/A | P'<br>(GPa) | $\int P' dt - I'$<br>(kPa-sec) | TOA'<br>(ms) |
|--------------------------|--------------------------|-----|-------------|--------------------------------|--------------|
|--------------------------|--------------------------|-----|-------------|--------------------------------|--------------|

RIGID GROUND SURFACE MODEL

|     |      |      |       |       |       |
|-----|------|------|-------|-------|-------|
| 1   | 0    | 0    | 10.09 | >1610 | --    |
| 1   | 0.25 | 0.25 | 2.78  | >1410 | 0.281 |
| 1   | 0.5  | 0.5  | 1.58  | >1380 | 0.332 |
| 1   | 1    | 1    | 0.93  | >1350 | 0.425 |
| 1   | 2    | 2    | 0.56  | >1320 | 0.602 |
| 1   | 3    | 3    | 0.41  | >1290 | 0.773 |
| 1   | 4    | 4    | 0.33  | >1260 | 0.942 |
| 1   | 5    | 5    | 0.28  | >1240 | 1.108 |
| 1   | 10   | 10   | 0.16  | >1150 | 1.925 |
| 0.3 | 0    | 0    | 10.09 | 521   | --    |
| 0.3 | 0.9  | 3    | 0.43  | > 437 | 0.744 |
| 0.3 | 1.5  | 5    | 0.29  | > 430 | 0.337 |
| 0.3 | 2.4  | 8    | 0.20  | > 420 | 0.485 |
| 0.3 | 3    | 10   | 0.16  | > 412 | 0.582 |
| 0.1 | 0    | 0    | 10.12 | 169   | --    |
| 0.1 | 0.3  | 3    | 0.42  | 143   | 0.078 |
| 0.1 | 3    | 30   | 0.06  | > 132 | 0.512 |

CIST-15 SOIL GROUND SURFACE MODEL

|   |     |     |      |       |    |
|---|-----|-----|------|-------|----|
| 1 | 0   | 0   | 6.15 | >1430 | -- |
| 1 | 0.5 | 0.5 | 1.10 | >1400 | -- |
| 1 | 1   | 1   | 0.74 | >1390 | -- |
| 1 | 3   | 3   | 0.36 | >1400 |    |
| 1 | 10  | 10  | 0.14 | >1330 | -- |

0.3 meter, and 0.1 meter. These calculations were performed in order to determine the relationship between the ANFO slab thickness and the total impulse, and also to verify that the maximum pressure at the ground surface was a function only of the ratio (V/A) of the void thickness to the ANFO thickness. The calculations using the CIST-15 model for the ground surface were performed only at a thickness of 1 meter.

Figure 2-3 shows the peak pressure calculated at the ground surface as a function of V/A. For the rigid boundary calculations, and for values of V/A from 0.25 to 30.0, a fit to the data gives

$$P' = 0.96 (V/A)^{-0.77} \quad (2.1)$$

where P' is in GPa. A similar, but slightly different relationship is found for the CIST-15 calculations, where V/A is varied between 0.5 and 10.0. It was found that these were well represented by the equation (see Figure 2-3):

$$P' = 0.75 (V/A)^{-0.69} \text{ GPa.} \quad (2.2)$$

Thus, it was verified that for an adequately wide range of values of both V and A, the peak pressure at the ground surface was a function only of the ratio V/A. Although this type of relationship is not required to define the STANDARD SOURCE charge dimensions, it does simplify the charge design process.

It was intuitively felt that the total impulse delivered through the ground surface, for reasonable standoff distances,

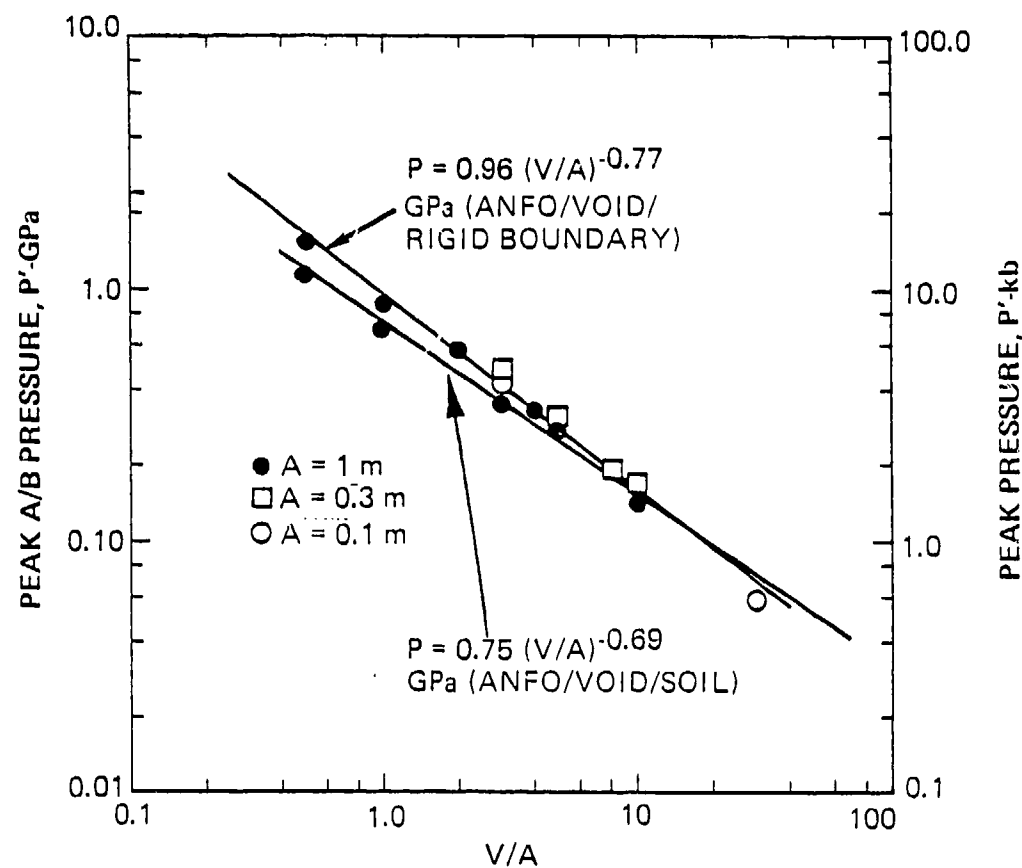


Figure 2-3 Peak pressure versus V/A from one-dimensional ANFO calculations.

would be only a function of the ANFO thickness itself.

Figure 2-4 plots the specific impulse,  $I'$ , versus  $A$ , for the case of zero standoff distance. For the 1-meter-thick ANFO slab, specific impulse had not achieved its final value in the 28 ms simulated in the calculations. Taking this into account, the computational results suggest that

$$I' \text{ (kPa-sec)} = 1730 A(m). \quad (2.3)$$

Thus, for the case of no standoff, a 1-meter-thick ANFO slab will deliver an impulse of 1730 kPa-sec to the ground surface. This value is consistent with previous results, such as those obtained during the MINE THROW simulation of JOHNNIE BOY (Reference 1). All of the calculations using realistic standoff distances were simulated only to a real time of 28 ms. Although the total impulse was delivered in only a few of the calculations, it was found that the specific impulse delivered during this time was only slightly dependent upon standoff distance, since the greater the standoff, the longer the time before the explosive gases contacted the ground surface. For the calculations using the rigid boundary representation of the ground surface, the total impulse was adequately represented by Equation 2.3. For the calculations using the CIST-15 soil representation of the ground surface, it was found that the total impulse was better represented by

$$I' \text{ (kPa-sec)} = 1500 A(m). \quad (2.4)$$

Thus, the use of a realistic soil equation of state slightly lowers the total impulse delivered to the ground surface.

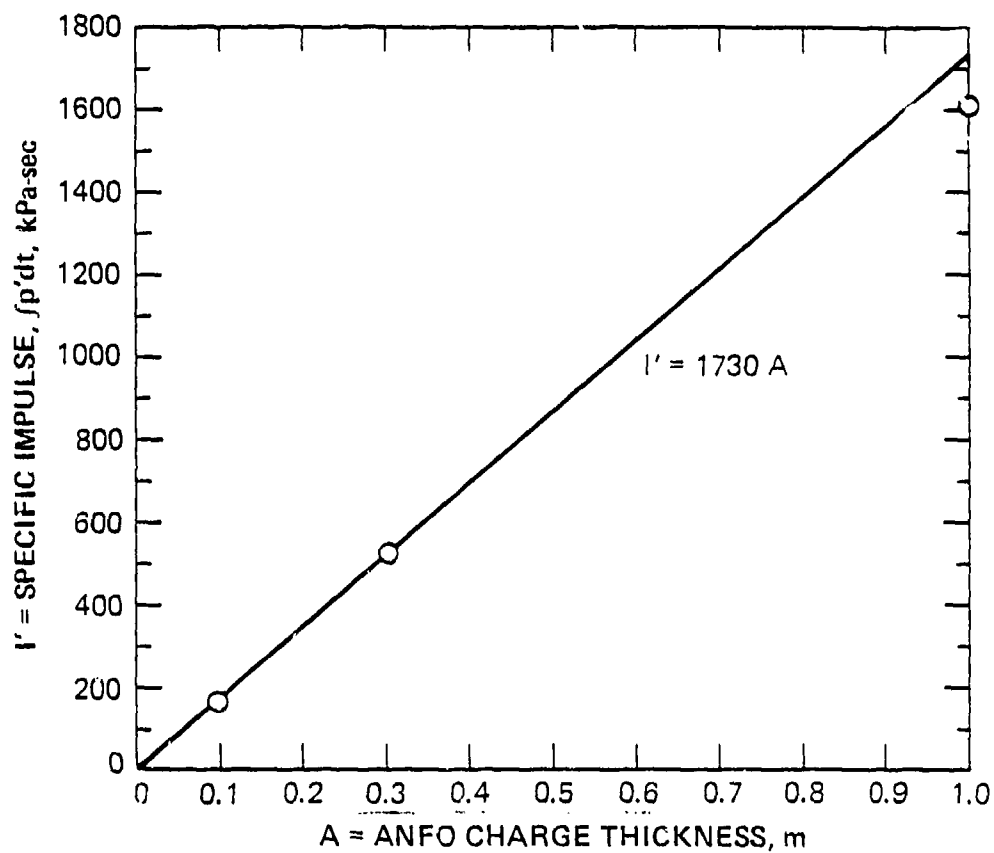


Figure 2-4 Total impulse delivered to the ground versus A (V=0) (from one dimensional calculations).

Figure 2-5 is a plot of the time of arrival of the explosive gases at the rigid boundary, TOA' versus the void thickness V. Data are shown for all three ANFO thicknesses studied. The data are consistent with a "closure velocity" of about 5.8 m/ms. The differences in intercepts for the different ANFO thicknesses reflect the time required for the detonation wave to reach the front surface of the ANFO slab. The detonation velocity in the ANFO was 5.1 m/ms. Therefore, for a 1-meter-thick slab, the detonation wave arrives at the front surface at about 0.2 ms. Similarly, for a 0.3-meter-thick ANFO slab, the front surface begins to move at about 0.06 ms following the initiation of the detonation at the rear surface. For the 0.1-meter-thick slab, the front surface begins to move about 0.02 ms after rear surface initiation. The closure time results for the one-dimensional calculation using the CIST-15 soil equation of state ground surface are not reported or plotted because they are exactly the same as those for the rigid boundary calculations.

It was recognized that using a void to represent the air within the standoff distance would lead to too large a closure velocity. To determine a more representative closure velocity, another one-dimensional calculation was performed. This calculation contained a 1-meter-thick ANFO slab surrounded by air. A realistic equation of state was used for the air. Figure 2-6 plots the air shock time of arrival versus the distance from the ANFO front surface. The propagation velocity of the air shock is nearly constant, at about 5.3 m/ms. As expected, this was slightly slower than the closure velocity obtained in the previous charge design calculations.



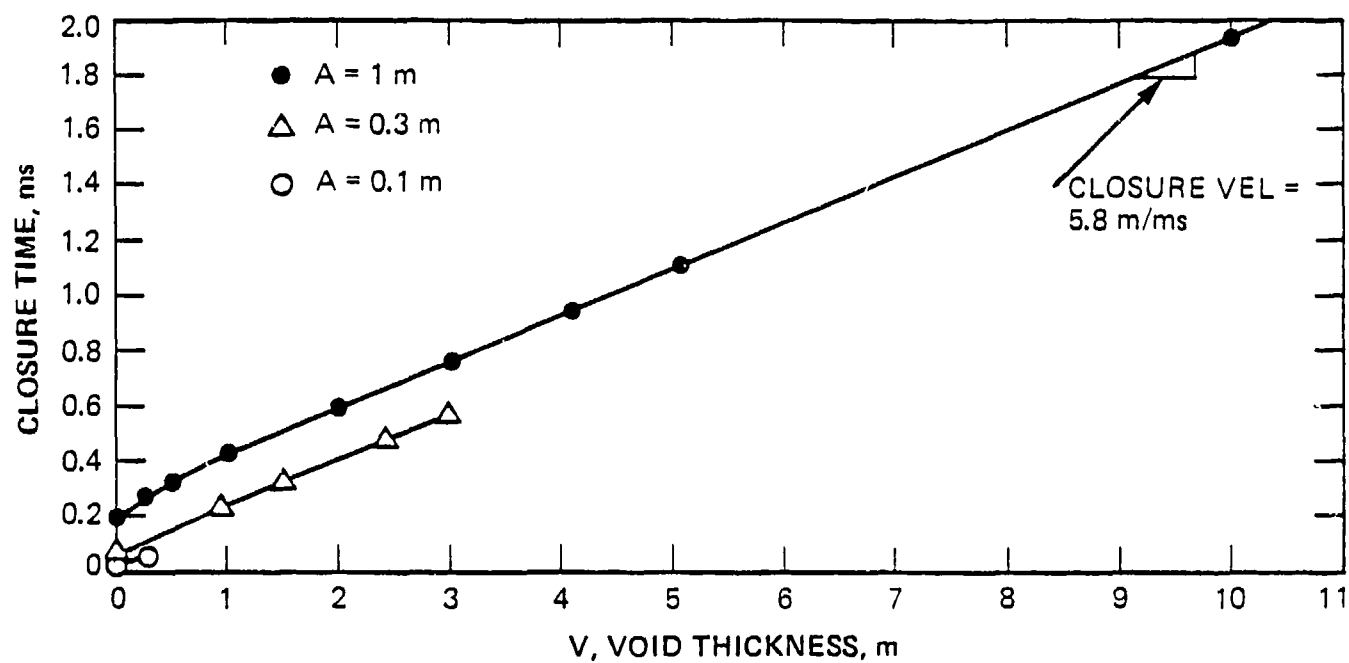


Figure 2-5 Closure time,  $TOA'$ , versus  $V$  from one-dimensional standard source calculations (ANFO/VOID/RIGID boundary).

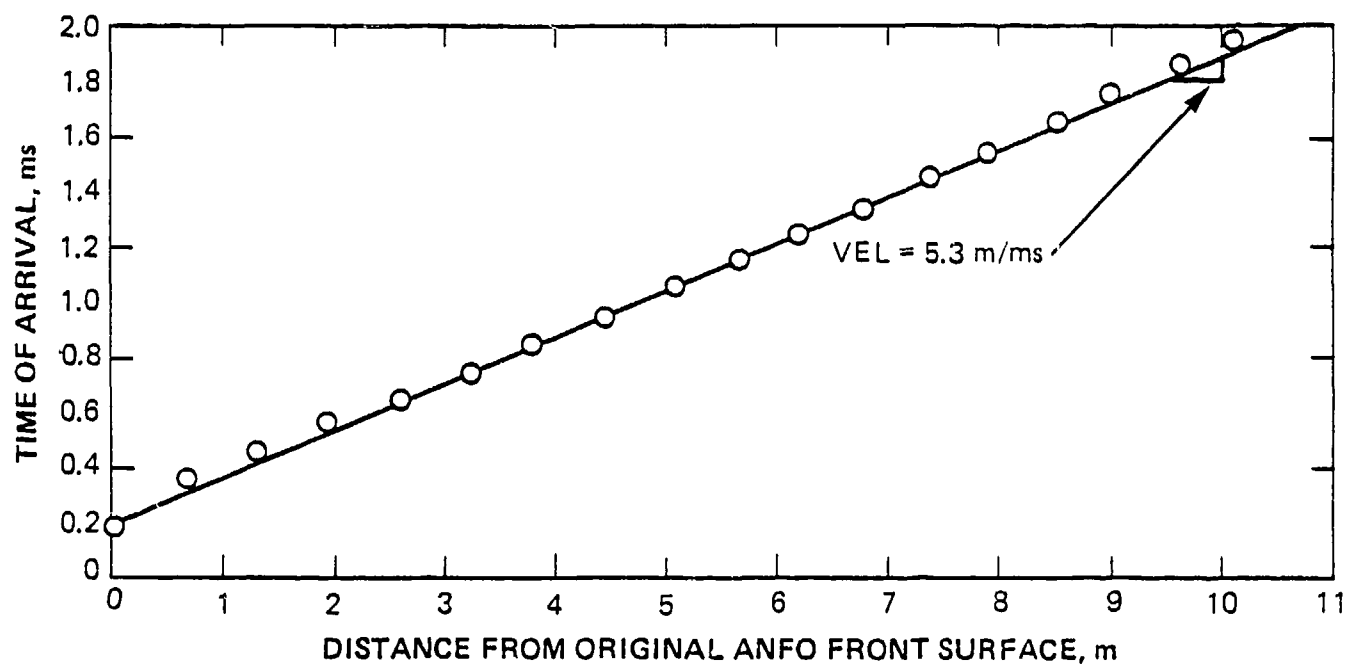


Figure 2-6 ANFO air shock TOA in air from one-dimensional calculation.

2.2.2 Nuclear Airblast Conditions. This section contains the data used to derive the nuclear conditions to be matched in the HE simulation. They include the peak airblast overpressure,  $P$ , the total impulse of the positive phase,  $I$ , and the airblast time of arrival, TOA. These were obtained from formulas presented by Brode (Reference 3), using a yield of 1.0 kt.

The peak overpressure versus range is shown in Figure 2-7. This is well represented by a simple functional form, as shown in the figure. Figure 2-8 presents the airblast TOA as a function of range. Figure 2-9 presents the total positive phase impulse,  $I$ , as a function of range. Table 2-3 presents the nuclear airblast conditions from a range of 4 meters to 25 meters.

2.2.3 Preliminary STANDARD SOURCE Charge Dimensions. Using the results of Sections 2.2.1 and 2.2.2, a candidate charge design could be developed. Before this design was developed, an attempt was made to account for the non-ideal nature of ANFO. This was done by uniformly lowering the HE peak pressures,  $P'$ , developed in Section 2.2.2. Then the procedure described in Section 2.1 was applied. This charge design was referred to as "first order corrected" STANDARD SOURCE charge design (Charge Design A).

The work of McKay, et al., (Reference 7) strongly suggested that an ANFO detonation gradually progressed to steady state over a distance of 1 to 1.5 meters. Thus, for ANFO thicknesses less than 1 meter, the detonation velocity, and hence the detonation pressure, were less than those attained under Chapman-Jouget (C-J) conditions. TOA data within an ANFO charge, are shown in

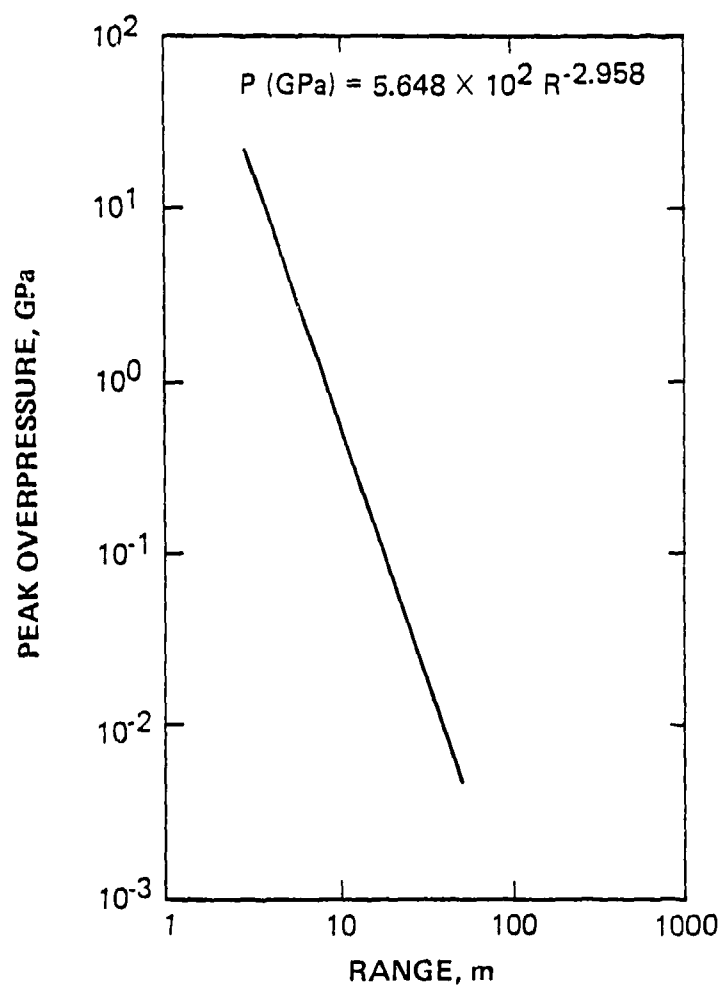


Figure 2-7 Airblast peak pressure versus range from a 1-kt nuclear surface burst.

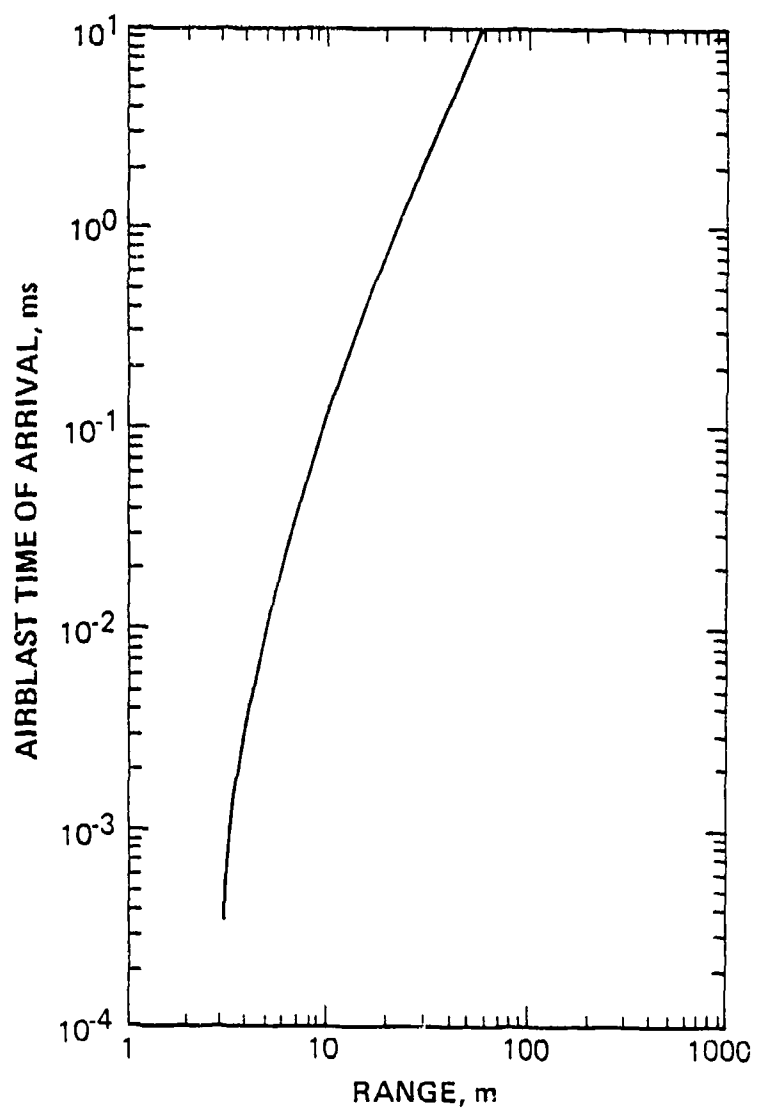


Figure 2-8 Airblast time-of-arrival for 1-kt nuclear surface burst.

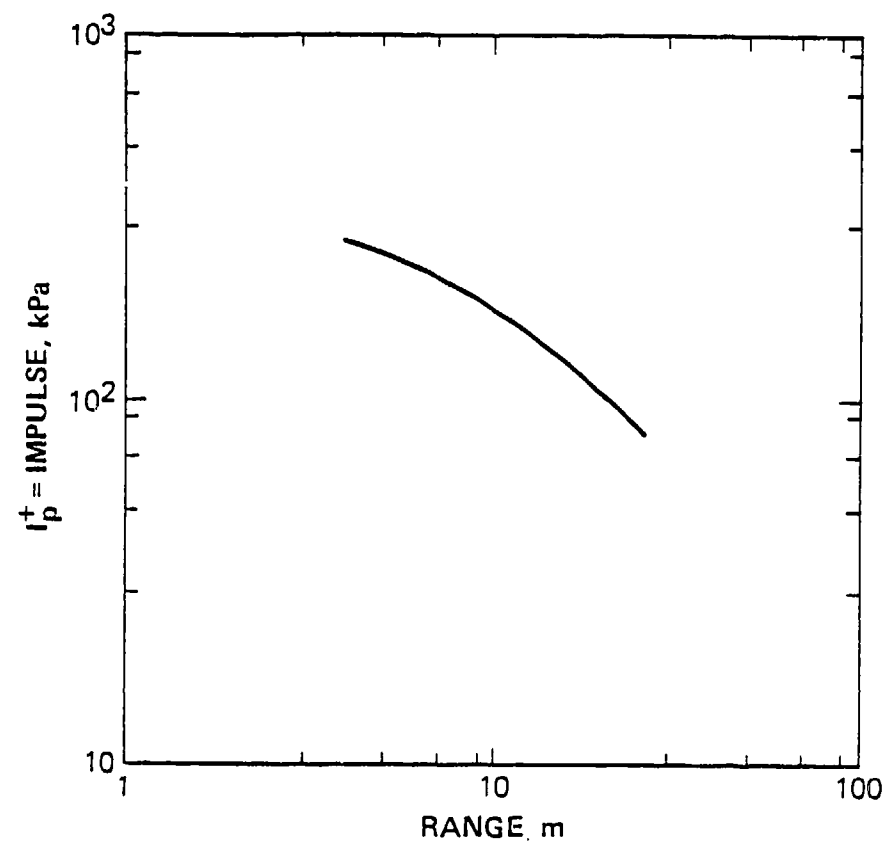


Figure 2-9 Airblast impulse versus range from a 1-kt nuclear surface burst.

TABLE 2-3

TABLE OF 1-kt NUCLEAR AIRBLAST CONDITIONS  
TO A RANGE OF 25 m

| Range (m) | TOA (ms) | P (GPa) | I (kPa-sec) |
|-----------|----------|---------|-------------|
| 4         | 0.003    | 9.354   | 274.7       |
| 4.6       | 0.007    | 6.187   | 265.4       |
| 5.0       | 0.012    | 4.834   | 257.3       |
| 6.0       | 0.028    | 2.819   | 236.6       |
| 7.0       | 0.047    | 1.787   | 219.2       |
| 8.0       | 0.069    | 1.204   | 204.9       |
| 9.0       | 0.094    | 0.850   | 192.4       |
| 10.0      | 0.123    | 0.622   | 181.1       |
| 11.0      | 0.157    | 0.469   | 170.8       |
| 12.0      | 0.196    | 0.363   | 161.3       |
| 13.0      | 0.241    | 0.286   | 152.4       |
| 14.0      | 0.294    | 0.230   | 142.7       |
| 15.0      | 0.353    | 0.188   | 136.4       |
| 16.0      | 0.421    | 0.155   | 129.2       |
| 17.0      | 0.498    | 0.129   | 122.5       |
| 18.0      | 0.584    | 0.109   | 116.4       |
| 19.0      | 0.678    | 0.093   | 110.7       |
| 20.0      | 0.783    | 0.080   | 105.5       |
| 25.0      | 1.452    | 0.041   | 84.8        |

Figure 2-10. For undiluted ANFO (94 percent ammonium nitrate, 6 percent fuel oil) the detonation velocity over the first meter is 3.8 m/ms, substantially slower than the nominal detonation velocity of 5.1 m/ms. From Chapman-Jouget theory,

$$P = \frac{\rho_o D^2}{\Gamma + 1}, \quad (2.5)$$

so for  $D = 3.8$  m/ms, the calculated peak pressure within one meter of the center of the detonation is 3.05 GPa, as opposed to the C-J pressure of 5.5 GPa. Equation 2.2 in Section 2.2.1 gave the peak pressure at the ground surface as a function of  $V/A$ .

In order to account for the non-ideal nature of the ANFO for thicknesses of less than one meter, these peak pressures were uniformly reduced by the ratio of the calculated peak pressure from Equation 2.5 to the C-J peak pressure, leading to a first-order corrected peak pressure,  $P'_c$ :

$$P'_c \text{ GPa} = \left( \frac{3.05}{5.5} \right) (0.75) \left( \frac{V}{A} \right)^{-0.69} = 0.416 \left( \frac{V}{A} \right)^{-0.69} \quad (2.6)$$

Setting  $P'_c$  equal to the Brode peak overpressure,  $P$ , for a 1 kt nuclear surface burst (Section 2.2.2) yields

$$V/A = 2.7 \times 10^{-5} R(m)^{4.32}. \quad (2.7)$$

The ratio of the standoff distance to the charge thickness is then determined.



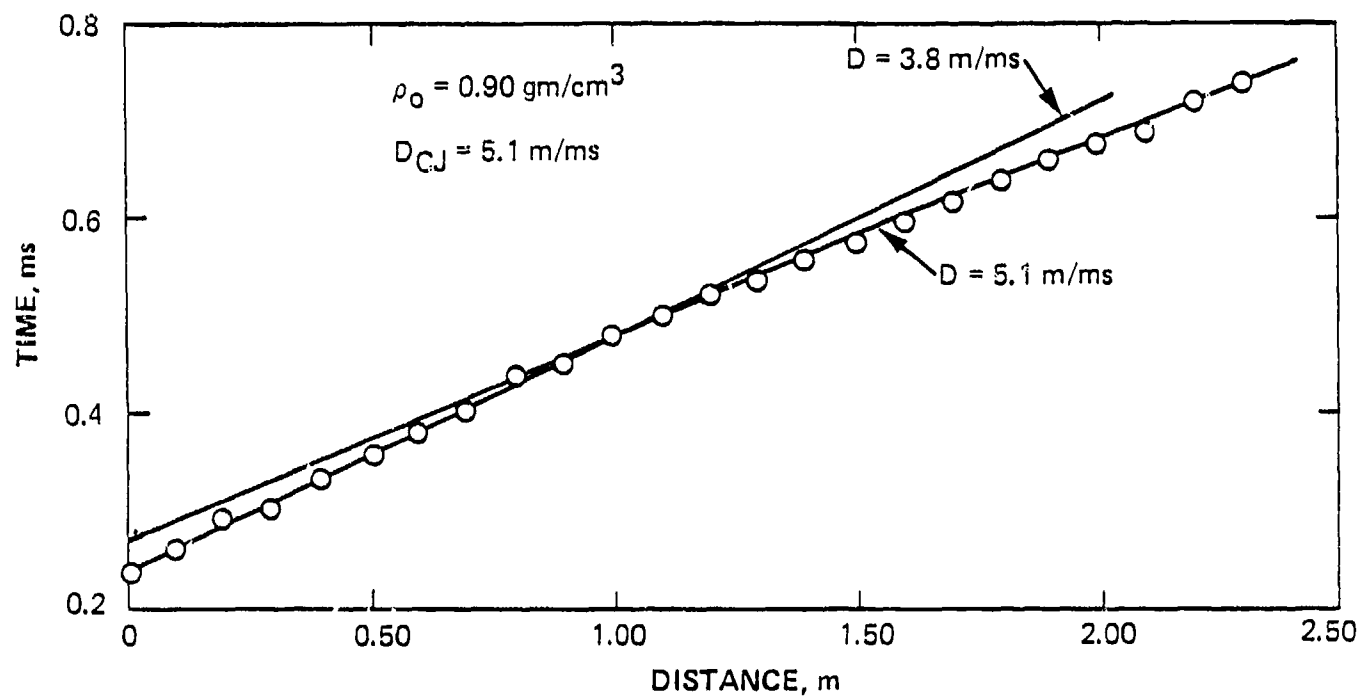


Figure 2-10 Detonation trajectory for undiluted 94/6 ANFO.

Equation 2.4 in Section 2.2.1 gave the total impulse derived from an ANFO sheet explosive of thickness  $A$ . When this impulse,  $I'$ , is set equal to the nuclear airblast impulse,  $I$ , the charge thickness,  $A$ , can be determined as a function of range. For this charge design the charge thickness,  $A$ , was determined by graphical means. Figure 2-11 shows the ANFO thickness as a function of range for this charge design.

Once the thickness of the charge is known as a function of range, the information can be combined with Equation 2.7 to give the standoff distance,  $V$ , as a function of range. This completes the charge design is shown in Figure 2-12.

Some comments regarding the merits of this design are in order. First, the peak airblast overpressures can be matched only at ranges greater than about 4.6 meters. At smaller ranges, the airblast impulse, which is the most important parameter, can be matched by simply increasing the thickness of the ANFO charge. However, in most applications the charge geometry at ranges of 4 to 5 meters will need to be integrated with the MINE THROW, or subsurface charge. Therefore, no effort was expended in examining the charge geometry for ranges of less than 4.6 meters.

Second, while the thickness of the charge decreases with increasing range, the standoff distance,  $V$ , for the charge increases with increasing range. At a range of 20 meters,  $V$  is about 0.86 meter. Carrying the charge out to a hypothetical range of 35 meters results in a standoff distance of about 10 meters. From a practical standpoint, a standoff distance of 1 to

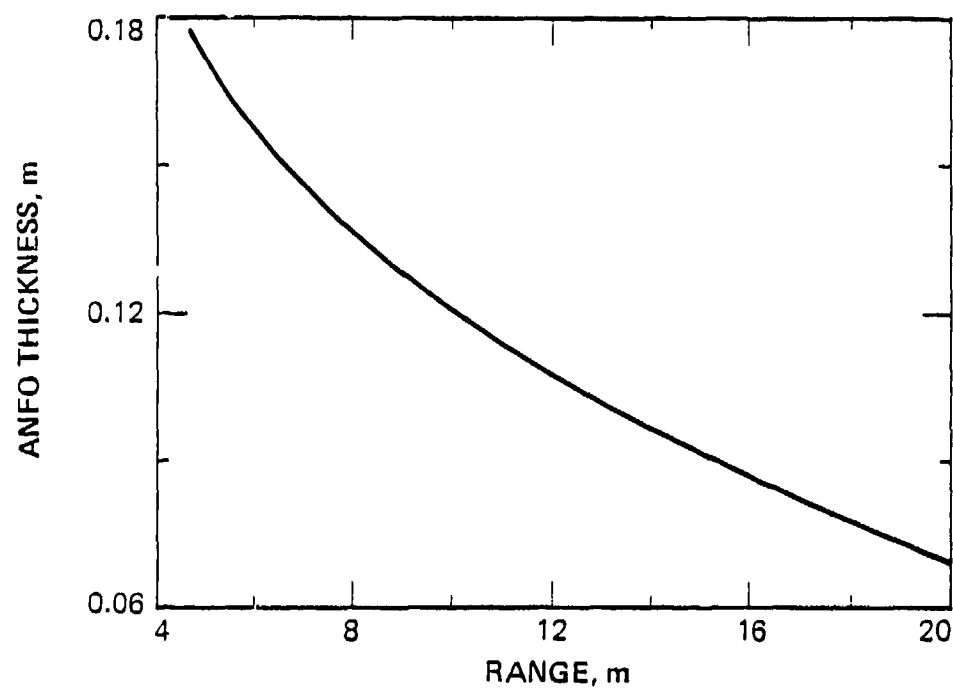


Figure 2-11 Explosive thickness versus range,  
Charge Design 1A.

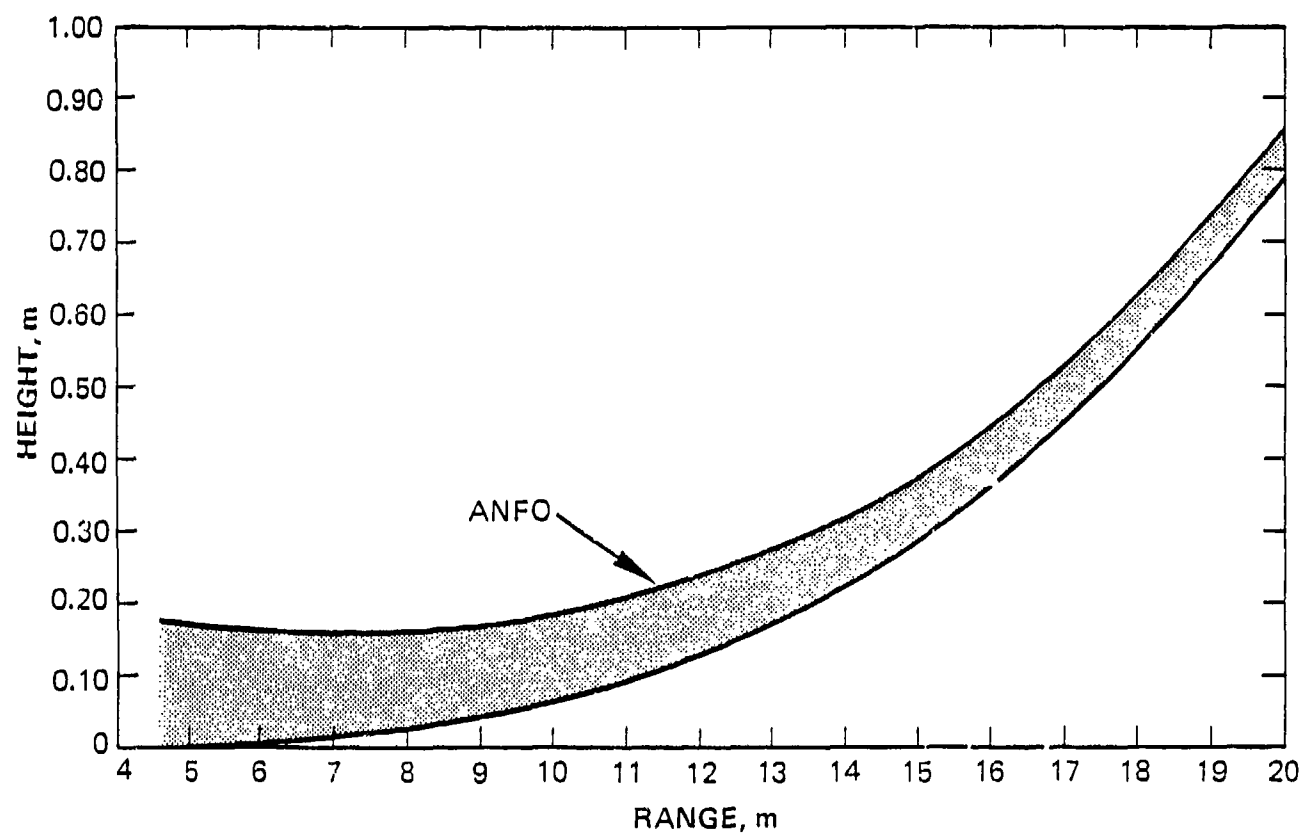


Figure 2-12 Standard source charge Design 1A (note expanded vertical scale).

2 meters was considered as a maximum, and thus the charge geometry was terminated at the 20 meter range.

Third, the charge thickness becomes quite small at large ranges. For example, at a range of 20 meters, A is 70 mm. As a result of the studies of the detonation characteristics of ANFO performed for the MINE THROW program (Reference 7), it was known that ANFO does not act in an ideal manner at those thicknesses. Even at a range of 4.6 meters, A is only 0.180 meter. Thus, over the entire range of the surface charge the ANFO thickness is in the range where the ANFO detonation characteristics are not presently well known and where the detonation may not be steady-state. This last point was to become the object of a substantial experimental effort later in the program.

Figure 2-13 shows how this charge design might be integrated with a hypothetical MINE THROW charge. Excluding this last charge, the integrated ANFO mass associated with this charge design was found to be 103.2 tons.

The detonation timing remains to be determined for Charge Design 1A. This was accomplished by graphically subtracting TOA from TOA', as discussed previously. A slight correction term due to the corrected ANFO detonation pressure was also applied. The resulting HE initiation time is given in Figure 2-14 as a function of range.

2.2.4 Detonator Spacing Calculations. The question of detonator spacing is an important one from technical as well as economic and fielding viewpoints. From the viewpoint of

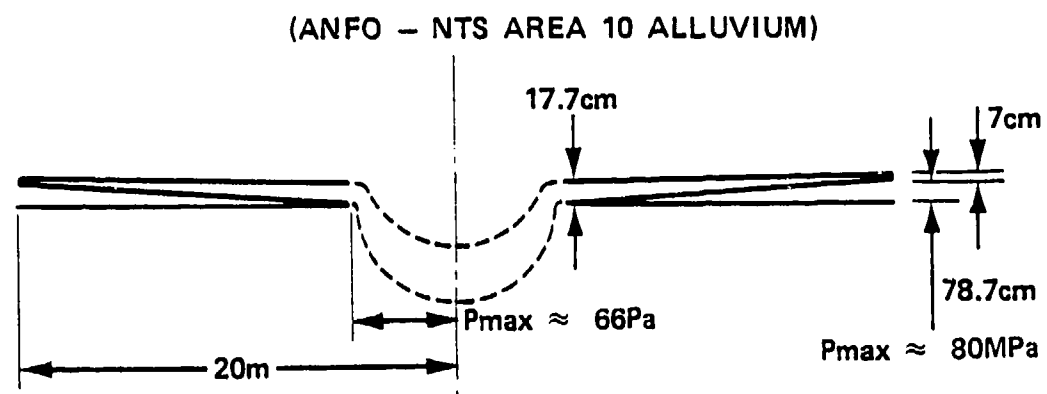


Figure 2-13 Charge Design 1A.

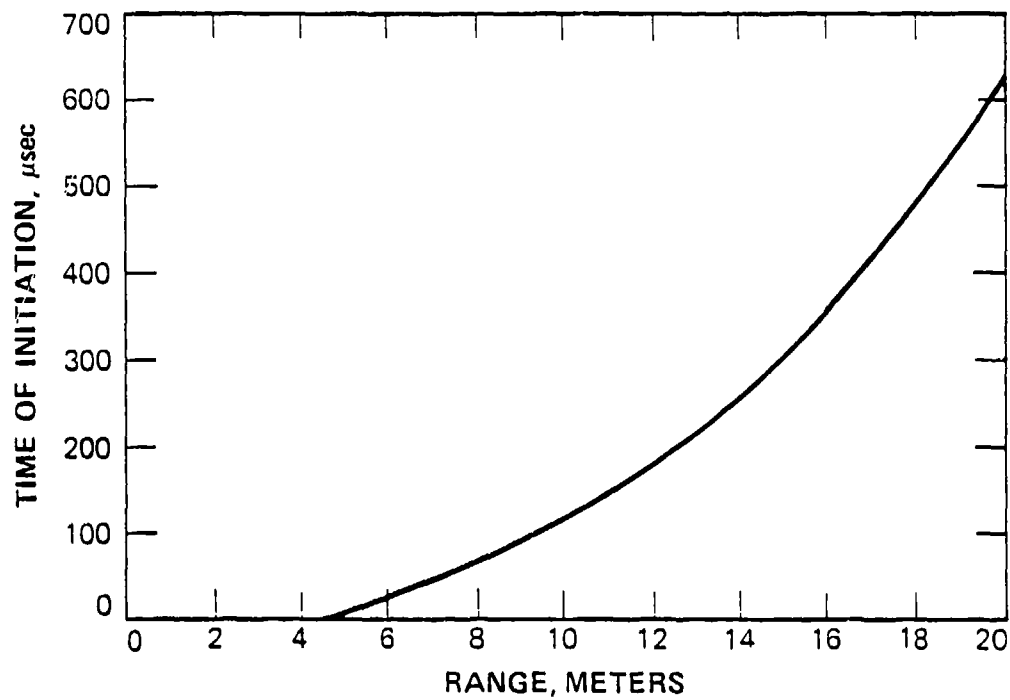


Figure 2-14 Initiation time versus range, Charge Design 1A.

economics and fielding, one wishes to use as few detonators as possible. On the other hand, if detonator spacing is too large, unacceptable perturbations in the airblast-induced ground motion will result because of multiple shock interactions. A matrix of two-dimensional calculations was performed to investigate the question of detonator spacing. This matrix included 9 two-dimensional calculations. The basic geometry for these calculations was an axis-symmetric ANFO disc overlying a void and infinitely thick disc of soil. In the calculations, the detonator spacing was chosen to be zero, (i.e., all surface zones detonated simultaneously) and specified multiples of the spacing  $A + V$ . Variation of peak pressure with range at the ground surface was examined, since peak pressure is a sensitive indicator of the perturbations resulting from finite detonator spacing. Table 2-4 summarizes the calculations performed. In these calculations, the ANFO was treated as a "non-ideal" explosive in a manner similar to that described in the previous section.



TABLE 2-4

SUMMARY OF TWO-DIMENSIONAL DETONATOR SPACING  
CALCULATIONS PERFORMED

| <u>Calculation</u> | <u>A (m)</u> | <u>V (m)</u> | <u>Detonator Spacing</u> |
|--------------------|--------------|--------------|--------------------------|
| 1                  | 0.1          | 0.0          | infinite                 |
| 2                  | 0.1          | 0.0          | 0.1 m = $(1[A+V])$       |
| 3                  | 0.1          | 0.0          | 0.2 m = $(2[A+V])$       |
| 4                  | 0.1          | 0.0          | 0.3 m = $(3[A+V])$       |
| 5                  | 0.1          | 0.1          | infinite                 |
| 6                  | 0.1          | 0.1          | 0.2 m = $(1[A+V])$       |
| 7                  | 0.1          | 0.1          | 0.4 m = $(2[A+V])$       |
| 8                  | 0.1          | 0.5          | 0.6 m = $(1[A+V])$       |
| 9                  | 0.1          | 0.5          | 1.2 m = $(2[A+V])$       |

The essential results of these calculations are shown in Figures 2-15 through 2-17. These plot the peak pressure or impulse at the ground surface as a function of range. Figure 2-15 shows that a detonator spacing of  $3(A+V)$  leads to significant pressure oscillations at the ground surface. Therefore, a detonator spacing this large was deemed unacceptable. Figure 2-16 shows results from calculations where the detonator spacing was  $1(A+V)$  and  $2(A+V)$ . The closer detonator spacing agrees very closely with the calculation using an infinite detonator spacing. The latter calculation leads to small but acceptable pressure oscillation at the ground surface. Thus, it was determined that a detonator spacing equal to  $2(A+V)$  would be an adequate for the STANDARD SOURCE charge design.

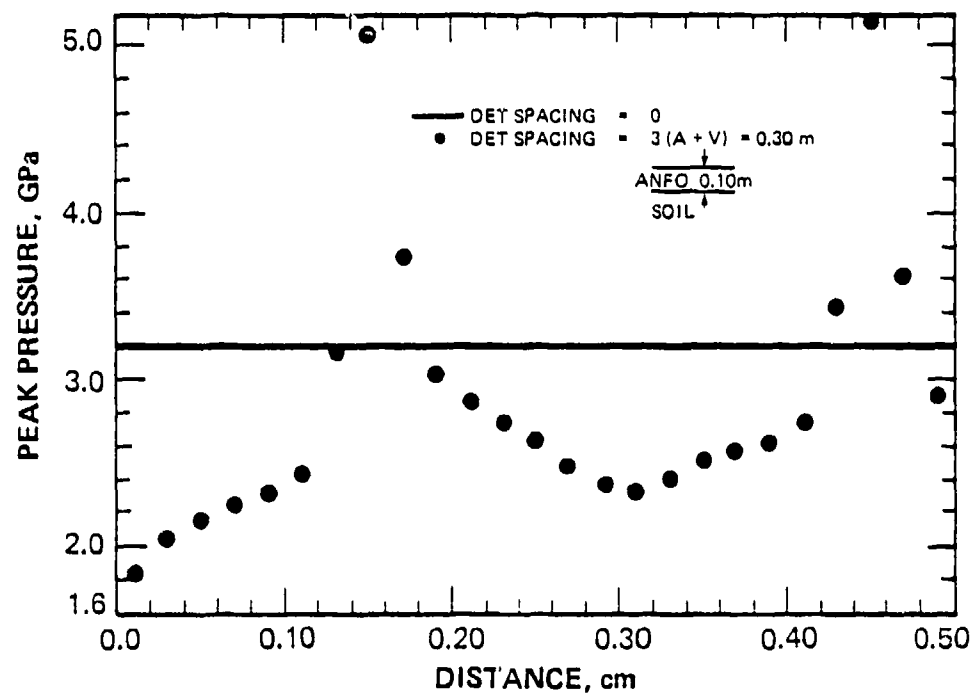


Figure 2-15 Calculations examining infinite and  $3(A+V)$  detonator spacing; peak pressure at ground surface versus range.

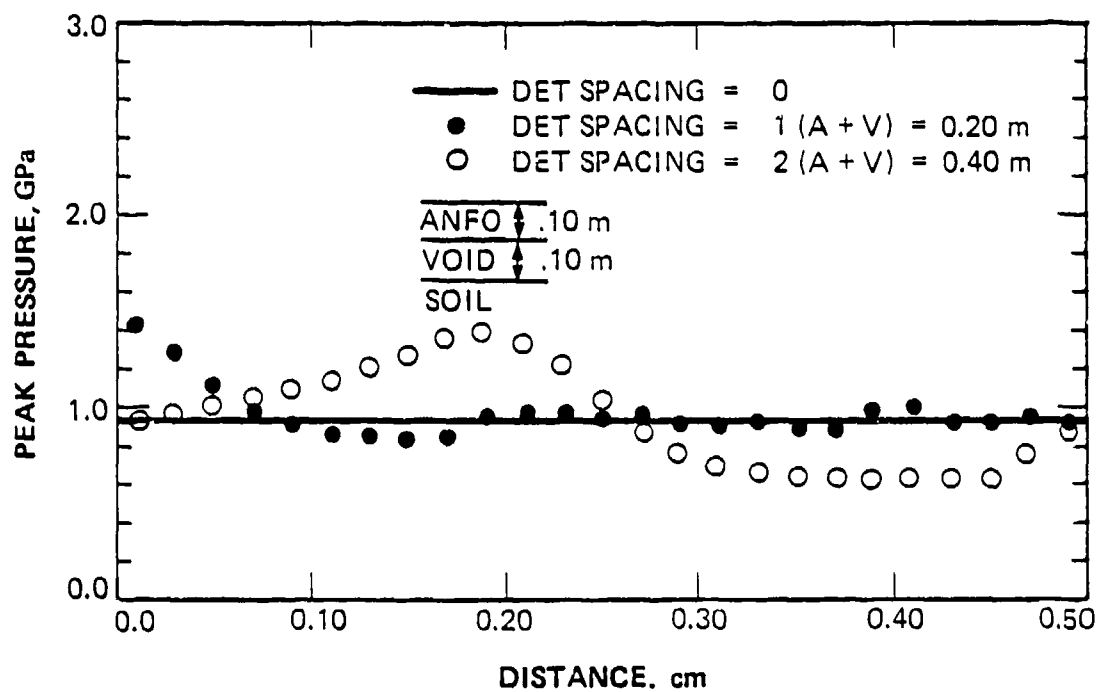


Figure 2-16 Calculations examining infinite, 1(A+V) and 2(A+V) detonator spacing; peak pressure at ground surface versus range.

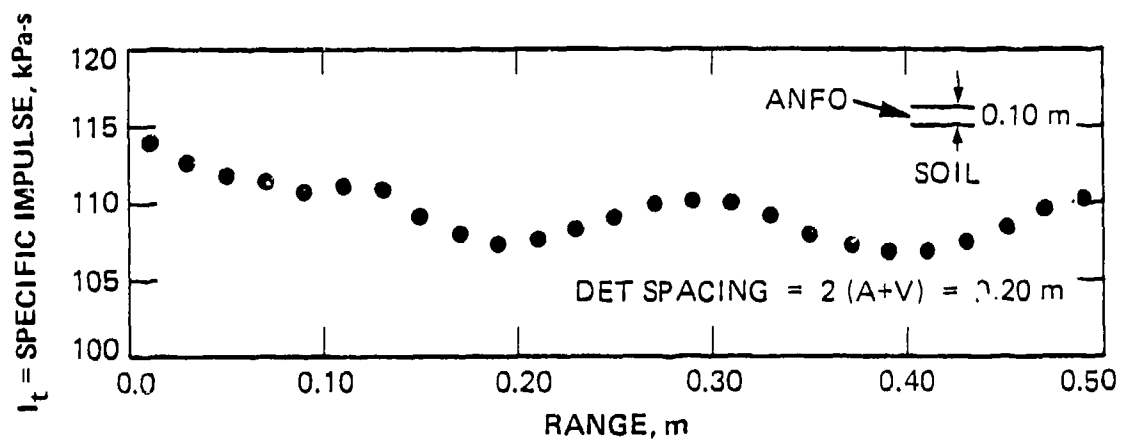


Figure 2-17 Effect of detonator spacing on impulse, spacing =  $2(A+V)$ , calculation No. 3.

It should be noted that the calculations performed would lead to larger than actual pressure oscillations. First, a void was used in the calculations rather than air. This greatly simplified the calculations and reduced their cost, but in reality the air between the charge and the ground surface will tend to diffuse perturbations and the shock wave resulting from finite detonator spacing. Further, the detonator spacing of the actual charge will be time phased to correctly simulate the air-blast TOA along the ground surface, as discussed in the previous section. Such time phasing of the detonation will also tend to smooth out perturbations resulting from finite detonator spacing.

For the chosen detonator spacing, Figure 2-17 shows the total impulse at the ground surface. The variations in total impulse are no larger than those observed in the peak pressure.

Using the candidate charge design, chosen detonator spacing and the initiation scheme for the charge, it was found that a total of 31 different detonator rings were required. The general concept is shown in Figure 2-18. At each of these detonation ranges (called detonation rings), high grade explosive boosters would be placed. The number of boosters per ring varied with range. Table 2-5 summarizes the proposed initiation scheme for Charge Design 1A. The total number of boosters required for this design, 4088, was found to be quite large. It was felt that a better initiation scheme should be worked out.

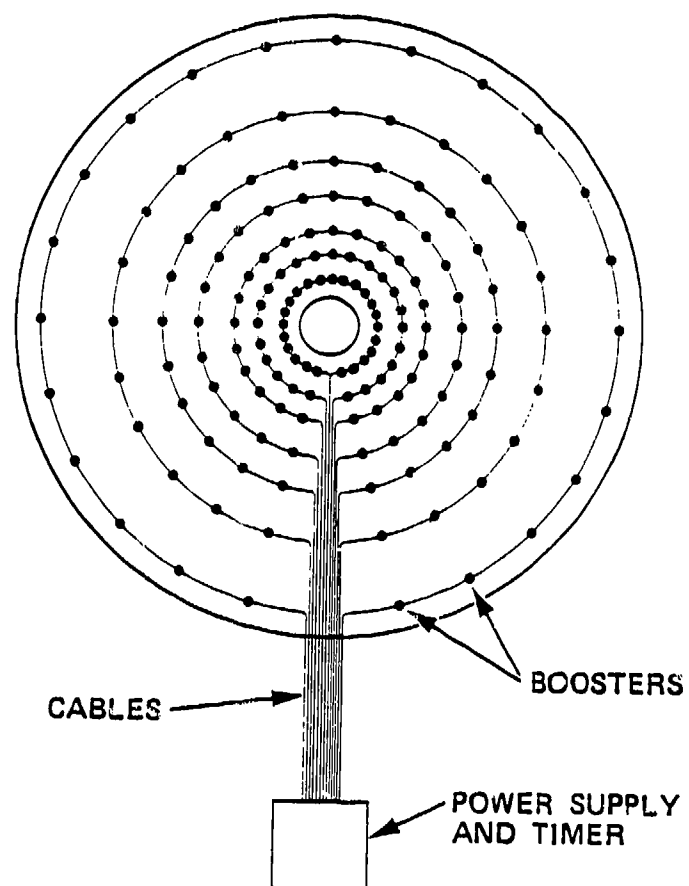


Figure 2-18 Concept of initiation geometry.

TABLE 2-5  
STANDARD SOURCE DETONATOR AND BOOSTER TIMING

| RADIUS-m | CIRCUMFERENCE<br>( $2\pi R$ )-m | $\lambda+V$ -m | DETONATOR SPACING,<br>$z2(A+V)$ -m | ~ NUMBER OF<br>DETONATIONS<br>PER RING<br>$2\pi R/2(A+V)$ | INITIATION<br>TIME<br>$\mu s$ | DISTANCE<br>BETWEEN<br>RINGS-ms | RING<br>NUMBER |
|----------|---------------------------------|----------------|------------------------------------|---|-------------------------------|---------------------------------|----------------|
| 4.6      | 28.9                            | 0.18           | 0.36                               | 80  | 0                             | 0                               | 1              |
| 5.0      | 31.4                            | 0.18           | 0.36                               | 87  | 4.8                           | 0.4                             | 2              |
| 5.36     | 33.7                            | 0.17           | 0.34                               | 99  | 10.0                          | 0.36                            | 3              |
| 5.70     | 35.8                            | 0.17           | 0.34                               | 105   | 20.0                          | 0.34                            | 4              |
| 6.04     | 38.0                            | 0.17           | 0.34                               | 112   | 23.6                          | 0.34                            | 5              |
| 6.39     | 40.1                            | 0.17           | 0.34                               | 118   | 29.0                          | 0.34                            | 6              |
| 6.72     | 42.2                            | 0.16           | 0.32                               | 132   | 36.0                          | 0.34                            | 7              |
| 7.04     | 44.2                            | 0.16           | 0.32                               | 138   | 44.3                          | 0.32                            | 8              |
| 7.36     | 46.2                            | 0.17           | 0.34                               | 136   | 51.0                          | 0.32                            | 9              |
| 7.70     | 48.4                            | 0.17           | 0.34                               | 142   | 59.0                          | 0.34                            | 10             |
| 8.04     | 50.5                            | 0.17           | 0.34                               | 149   | 66.9                          | 0.34                            | 11             |
| 8.38     | 52.7                            | 0.17           | 0.34                               | 155   | 74.0                          | 0.34                            | 12             |
| 8.72     | 54.8                            | 0.17           | 0.34                               | 161   | 82.0                          | 0.34                            | 13             |
| 9.06     | 56.9                            | 0.18           | 0.36                               | 158   | 89.8                          | 0.34                            | 14             |
| 9.42     | 59.2                            | 0.18           | 0.36                               | 164   | 100.0                         | 0.36                            | 15             |
| 9.78     | 61.4                            | 0.19           | 0.38                               | 162   | 109.0                         | 0.36                            | 16             |
| 10.16    | 63.8                            | 0.19           | 0.38                               | 168   | 119.0                         | 0.38                            | 17             |
| 10.54    | 66.2                            | 0.20           | 0.40                               | 166   | 130.0                         | 0.38                            | 18             |
| 10.94    | 68.7                            | 0.21           | 0.42                               | 164   | 142.0                         | 0.40                            | 19             |
| 11.36    | 71.4                            | 0.23           | 0.46                               | 155   | 155.0                         | 0.42                            | 20             |
| 11.82    | 74.3                            | 0.24           | 0.48                               | 155   | 170.0                         | 0.46                            | 21             |
| 12.30    | 77.3                            | 0.26           | 0.52                               | 149   | 186.0                         | 0.48                            | 22             |
| 12.82    | 80.6                            | 0.28           | 0.56                               | 144   | 207.0                         | 0.52                            | 23             |
| 13.38    | 84.1                            | 0.30           | 0.60                               | 140   | 228.0                         | 0.56                            | 24             |
| 13.98    | 87.8                            | 0.32           | 0.64                               | 137   | 257.8                         | 0.60                            | 25             |
| 14.62    | 91.9                            | 0.36           | 0.72                               | 128   | 287.0                         | 0.64                            | 26             |
| 15.34    | 96.4                            | 0.41           | 0.82                               | 118   | 324.0                         | 0.72                            | 27             |
| 16.16    | 101.5                           | 0.47           | 0.94                               | 108   | 370.0                         | 0.82                            | 28             |
| 17.1     | 107.4                           | 0.55           | 1.10                               | 98  | 425.0                         | 0.94                            | 29             |
| 18.2     | 114.4                           | 0.65           | 1.30                               | 88  | 495.0                         | 1.10                            | 30             |
| 19.5     | 122.5                           | 0.85           | 1.70                               | 72  | 590.0                         | 1.3                             | 31             |

#### 2.2.5 Two-Dimensional Charge Performance Calculation.

Using the preliminary charge dimensions and the detonator spacing previously discussed, a two-dimensional calculation was performed to directly compare the peak pressure, time of arrival, and total impulse delivered to the ground surface, with the desired nuclear environment. The equations-of-state for the ANFO and the soil were the same as discussed previously. However, because the calculation was performed primarily in Eulerian coordinates, it was possible to use a real air equation-of-state instead of the void approximations used in the one-dimensional calculations. The charge dimensions for this calculation are the same as presented in the Figure 2-12; the detonator spacing and timing is as presented in Table 2-5.

The calculation was performed to a total time of 1.76 ms. The essential results of the calculation are presented in Figures 2-19 through 2-21. Figure 2-19 shows the computed HE time of arrival, TOA', versus range at the ground surface, compared with the nuclear time of arrival. Over the region of the surface charge (4 to 20 meters) the agreement is very good. For ranges beyond the radial edge of the surface charge, the HE arrivals are late compared with the nuclear arrival time. Figure 2-20 is a plot of the computed peak airblast pressure versus range for the charge geometry compared to that for a Brode 1 kT surface burst. At ranges less than approximately 8 m, the computed pressures are slightly low; at greater ranges they are slightly above the Brode curve. Because of rather coarse zoning for ranges beyond 15 meters, the peak pressures from the calculation exhibit a somewhat erratic behavior. Overall, the agreement is considered very good for the first design attempt,



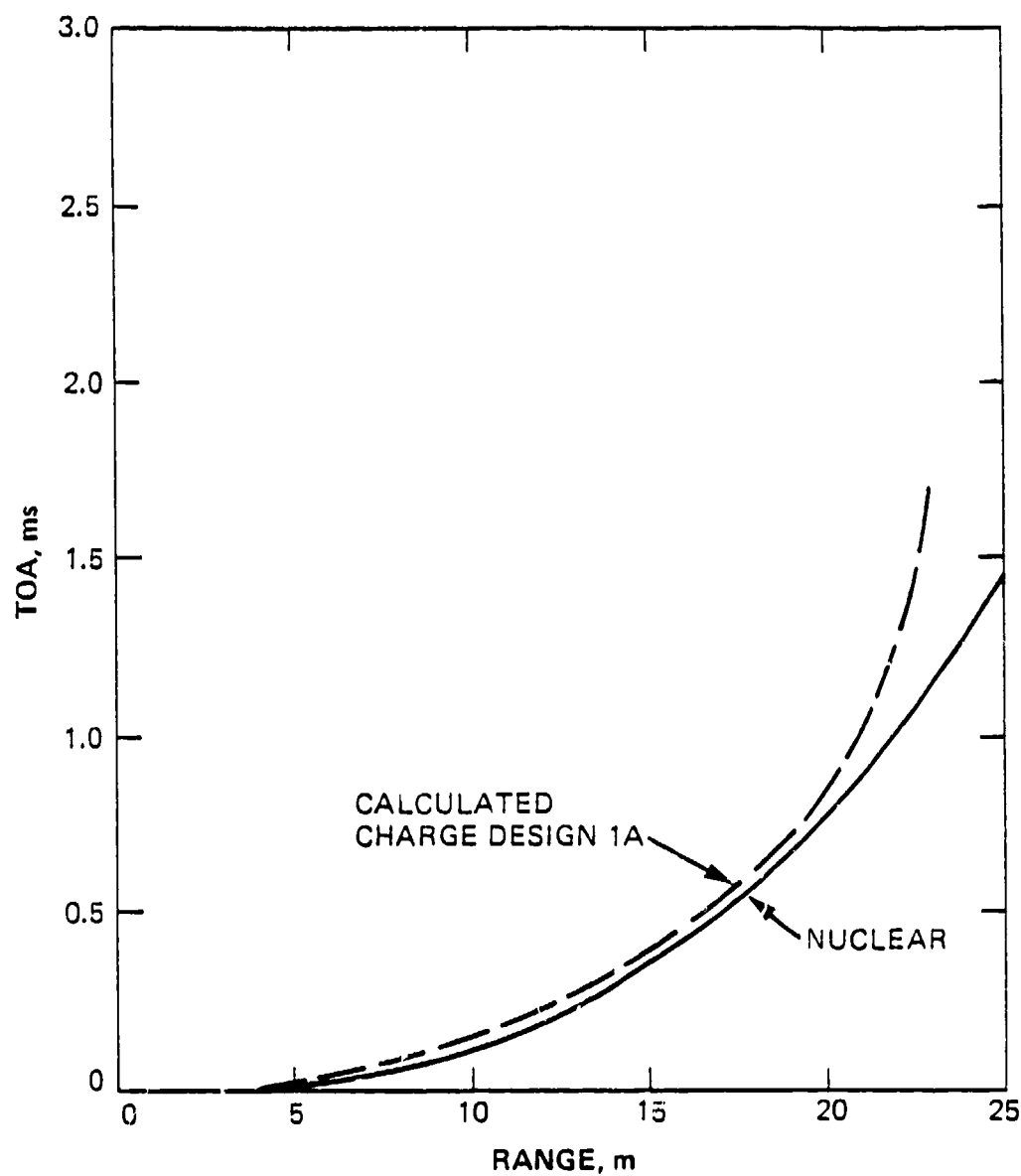


Figure 2-19 Two-dimensional charge performance calculation; computed time-of-arrival at the ground surface versus range compared with 1-kt nuclear time-of-arrival.

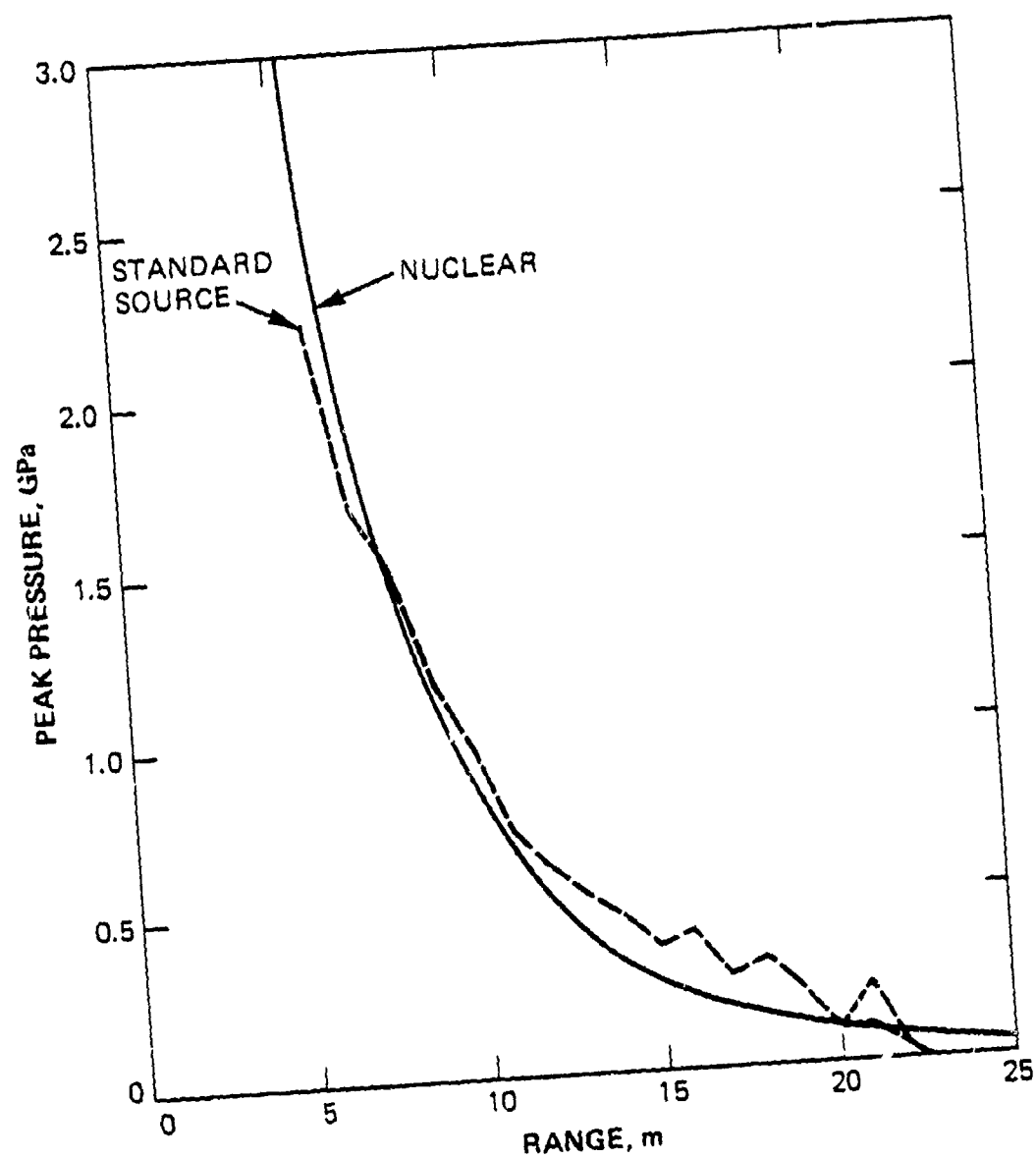


Figure 2-20 Two-dimensional charge performance calculation; computed overpressure versus range at the ground surface compared with 1-kt nuclear overpressures.

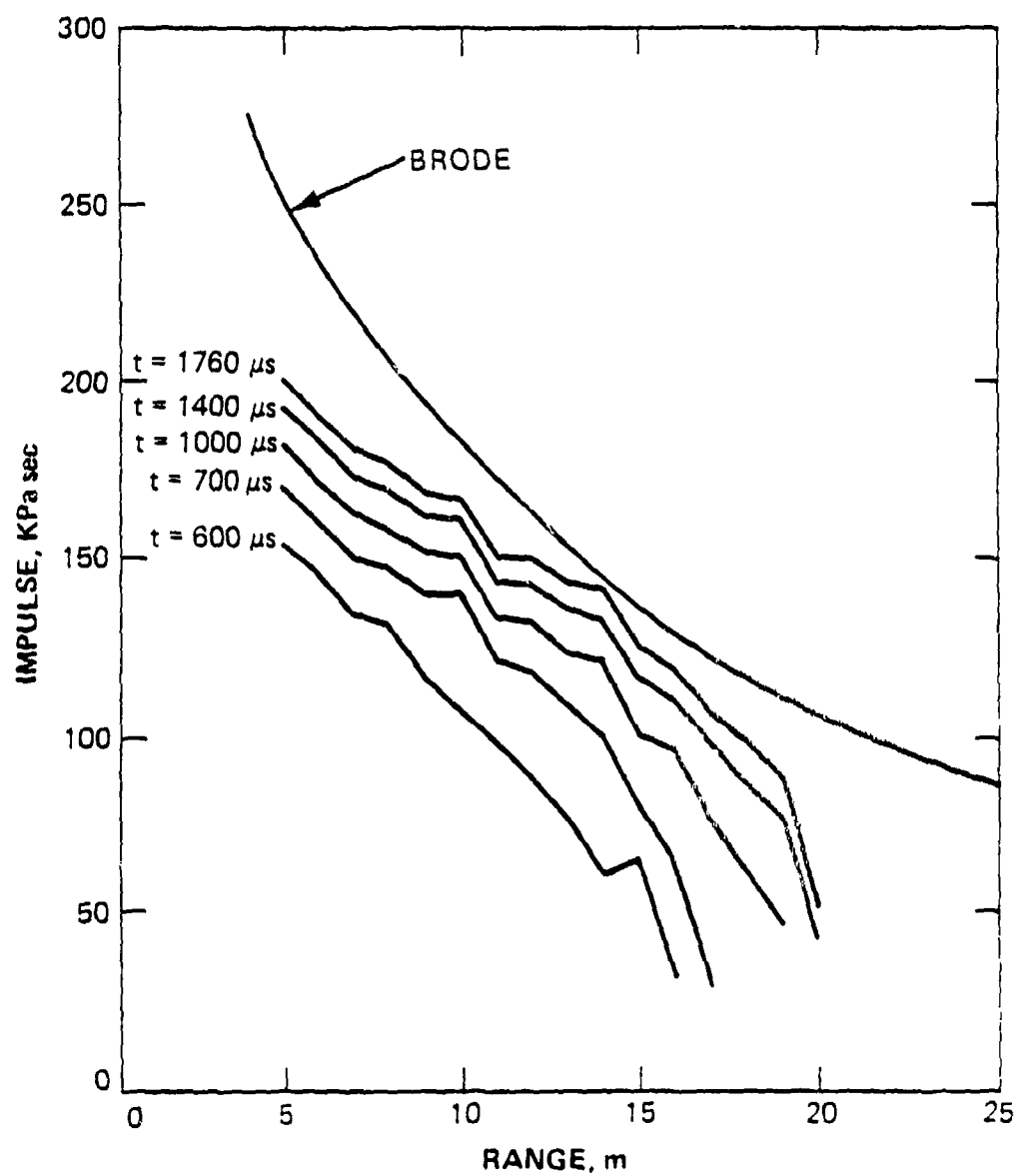


Figure 2-21 Two-dimensional charge performance calculation; computed total impulse versus range at the ground surface at five times, compared with total 1-kt nuclear impulse.

and the calculation provided important information on two-dimensional effects which would have to be taken into account to improve the overall charge design. Figure 2-21 plots the computed impulse,  $I'$ , versus range at 5 times during the calculation: 0.6, 0.7, 1.0, 1.4, and 1.76 ms. Impulse was still being delivered to the ground at the end of the calculation. Analysis of the results suggested that the computed impulse versus range would be somewhat less than the Brode nuclear curve due to the two-dimensional effects. To improve the agreement between the HE results and the desired nuclear impulse, one would increase the thickness of the charge in the ranges where the impulse was less than that desired. This increase would in turn increase the amount of ANFO required to perform the simulation, but not by a significant amount.

2.2.6 Preliminary STANDARD SOURCE Charge Design. The STANDARD SOURCE design is made up of two parts: a surface or airblast charge, and a subsurface or cratering charge. The work performed during this phase of the program concentrated on the design of the surface charge. It was seen that this charge could be constructed using the sheet of ANFO of varying thickness placed above the ground surface. The actual charge geometry was given in Figure 2-13. Construction of a charge of this size was a technical problem in itself. Some additional design work was performed to investigate the feasibility of performing a full-scale test.

First, the problem of charge support was considered. The design requires that a continuous ANFO sheet charge be placed above the ground surface at a standoff height which varies with

range. The simplest way to accomplish this was to use 1.2 x 2.4 meters x 8 foot cardboard trays as shown in Figure 2-22. These trays would be made of low mass honeycomb cardboard and supported by low mass styrofoam pillars. The depth of the trays would be adjusted for the correct depth of the explosive at the range (from ground zero) where that particular tray was to be emplaced. The styrofoam pillars would be cut to the proper height above the ground surface. Several hundred of these trays would be required to replace the entire charge. However, the weight of the charge would be distributed rather uniformly over the ground surface.

Figure 2-23 shows a schematic of the STANDARD SOURCE charge, composed of the array of ANFO trays making up the surface charge, and the ANFO subsurface charge. This is an artist's conception of how the below-ground charge is integrated with the above-ground airblast charge. A suitable protective housing must be provided for this entire arrangement, since it would be very susceptible to weather conditions, especially wind loadings, snow, and rain. Protective housings might include a snow fence with a tarpaulin acting as a wind shield, and a plastic covering over the charge to keep out moisture. Alternatively, a large building or tent could be constructed over the entire charge. A mobile catwalk could be constructed to bridge the charge to allow placement of detonators.

Serious consideration of the fielding aspects of a STANDARD SOURCE charge led to a realization that more experimental tests and design work would be required prior to such a test. The main items of concern, or "key unknowns," are discussed in Section 2.3.

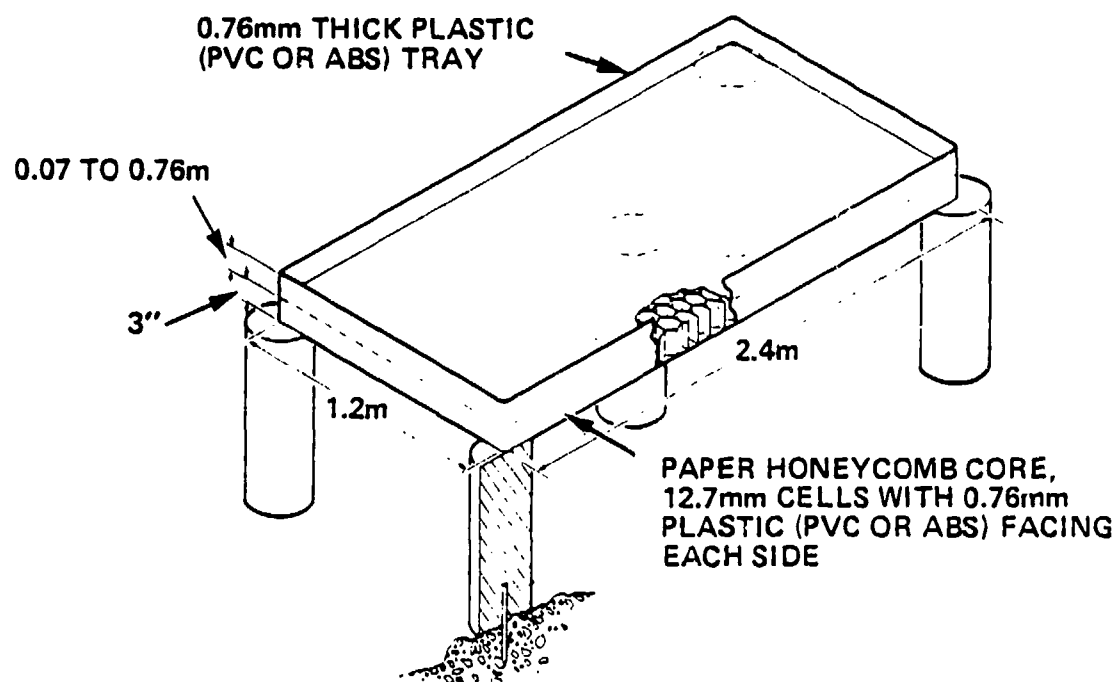


Figure 2-22 Typical panel for supporting ANFO.

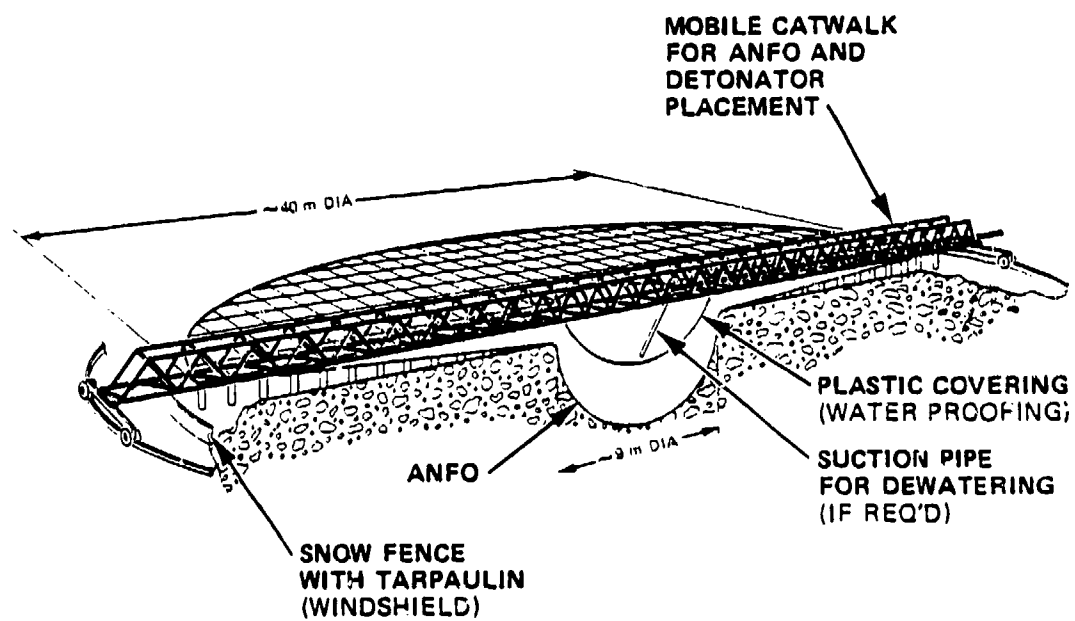


Figure 2-23 Conceptual layout of standard source charge.

### 2.3 SUMMARY OF KEY UNKNOWNNS

Several key unknowns affecting the feasibility of performing a STANDARD SOURCE type experiment arose from this preliminary investigation. These are discussed briefly in this section.

First, the primary concern was that the charge design was based solely on calculations which assumed ideal or "near ideal" behavior of ANFO in thin sheets. Very little experimental data existed which would confirm or deny the existence of a low order ANFO detonation in thin sheets, but it was strongly felt that before constructing such a large field test the properties of the explosive should be well known. It was desired to continue with ANFO as the primary explosive for consideration because of its comparatively low cost. To address this point, a small scale experimental program was recommended. Also, the detonator spacing was chosen based on similar types of calculations. Similar verification of the adequacy or inadequacy of this spacing would be needed before field construction began.

Second, an initiation system would have to be designed and tested. The STANDARD SOURCE charge design involves a considerable number of detonation points, all of which must be carefully timed in order to simulate the arrival of the nuclear airblast.

Third, a subsurface or MINE THROW charge would need to be designed and tested. It was concluded that this charge should simulate the direct-induced cratering and ground motion for a specific nuclear event.



Fourth, the low overpressure airblast characteristic of the STANDARD SOURCE charge needed to be investigated. The primary overpressure region of interest was that for pressures of less than 100 psi. Both calculational and experimental efforts were considered in order to answer this question.

Finally, a subscale field test of the full simulation concept was considered. This test, although not simulating any specific nuclear effects, would verify all of the techniques involved in this new technology.

With these efforts outlined, the program proceeded to more serious feasibility studies. Section 3 of this report discusses the work performed in order to address these key uncertainties.

## SECTION 3

### FURTHER INVESTIGATION OF TECHNICAL FEASIBILITY

#### 3.1 EARLY THIN ANFO INVESTIGATION

The purpose of this series was to investigate the detonation and initiation properties of thin, plane, unconfined layers of ANFO. This series of tests was delayed by a prolonged period of rainy weather. Testing finally began in mid-March of 1978 and was concluded in mid-August of 1978. There were interruptions throughout this period to accommodate other tests and to evaluate results.

3.1.1 Experimental Geometry and Instrumentation. The charge containers for all of the early experiments consisted of trays made of double strength cardboard with dimensions of 60 cm wide, 90 cm long, and 18 cm deep. The tray was supported by four wooden legs (one at each corner), elevating the bottom of the tray 50 cm above and parallel to the ground surface.

Detonation of these charges was initiated from the center of one end of the tray.

The first experiments were concerned with selecting the proper initiator that would reliably cause detonation of the ANFO with a minimum of overdrive from the booster.

All experiments except the first three have diagnostic ionization pin gages to measure the detonation velocity. The pin geometry was the same for all shots except the final experiment, shot No. 26. A diagram of the ionization pin locations and the booster is shown in Figure 3-1. The pins have a 7.5 cm spacing and are on two diagonal lines with overlap for redundancy. The booster consists of a 15 cm length of 400 grain primacord with four 5 cm lengths tied in parallel at the end for boost. The charge was always initiated at the mid-depth of the ANFO.

Shots 4 through 7 were detonated 50 cm above a 2-inch-thick steel plate that rested on a 45 cm thick concrete foundation. The steel plate had ports for four pressure transducers. These are also shown in Figure 3-1 as P1, P2, P3, and P4. They are in line with TOA Pin No. 13 and are 15 cm on centers.

The pressure gages used on shots Nos. 4, 5, and 6 were PCB101A03\* rated at  $1.38 \times 10^5$  kPa (20,000 psi). The gages all failed at shock arrival and only provided arrival time on the plate, indicating pressures were much higher than predicted. On shot 7 ballistic dynamic pressure transducers were used on the plate. These were model PCB108A rated at  $5.5 \times 10^5$  kPa (80,000 psi). These gages provided peak pressure data but failed because of the extremely high accelerations. (The connector assembly on the gage flew apart).

---

\*Manufactured by PCB Piezotronics, Inc., Buffalo, New York.

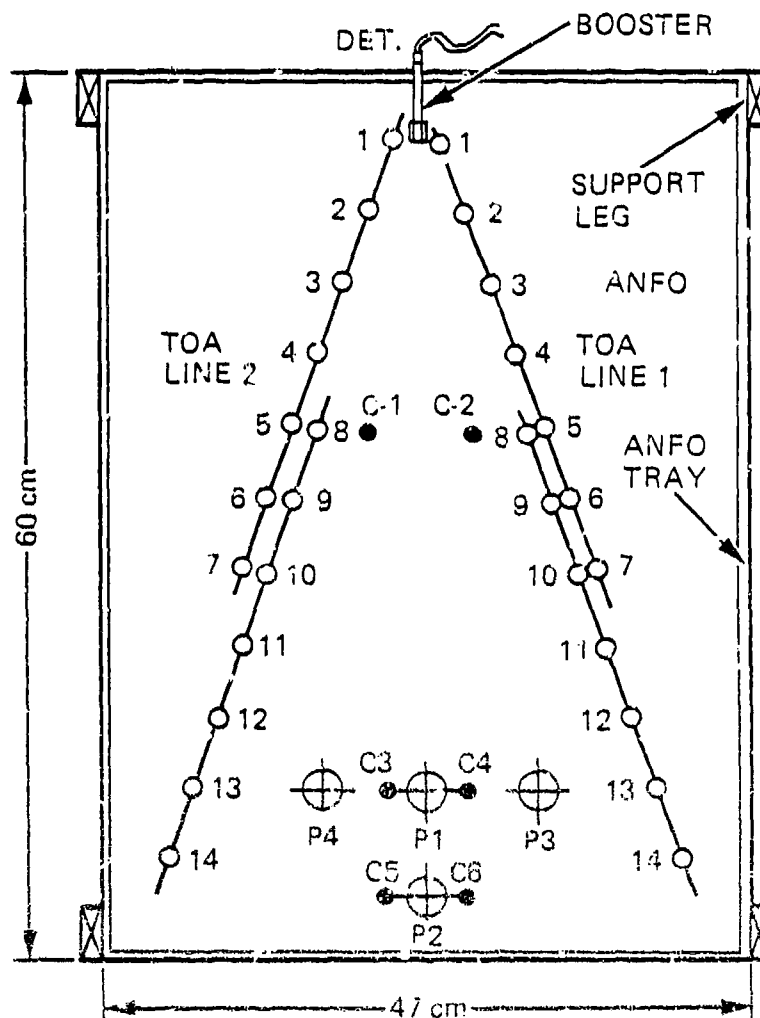


Figure 3-1 Thin film ANFO with TOA Pins and booster.

locations are shown in Figure 3-1 as C1 through C6. The gages are 4 cm long by 2 cm in diameter and were inserted in drill holes in the plate with the upper face flush with the surface of the plate. Shot 23 used the same type ANFO tray as previous shots. The ground surface under the charge had a 2.5-cm-thick aluminum witness plate on a 15-cm-thick bed of sand. The aluminum plate had eleven piezoelectric time-of-arrival pins (Model CA-1135) and two carbon pressure gages (Model C300-50-EK\*).

The gage layout for shot 23 is shown in Figure 3-2. Time-of-arrival piezoelectric pins are labeled T-1 through T-11. Pins T-4, T-5, T-6, T-7 and T-11 are flush with the upper surface of the plate. Carbon pressure gages are labeled C1 and C2.

Instrumentation on these shots consisted of shorting pins in the ANFO for detonation velocity measurements, PZ (piezoelectric) pins for measuring shock propagation velocity across the witness plate, and diaphragm pressure, carbon pressure and passive crush gages.

The ANFO shorting pins were operated in groups of seven in a serial string. Small capacitors were alternately charged positively and negatively at 300 volts d.c. As the pins were shorted by the ionization front, they discharged their respective capacitors across a common load resistor to produce a train of

---

\*Manufactured by Dynasen, Inc., Goleta, California.

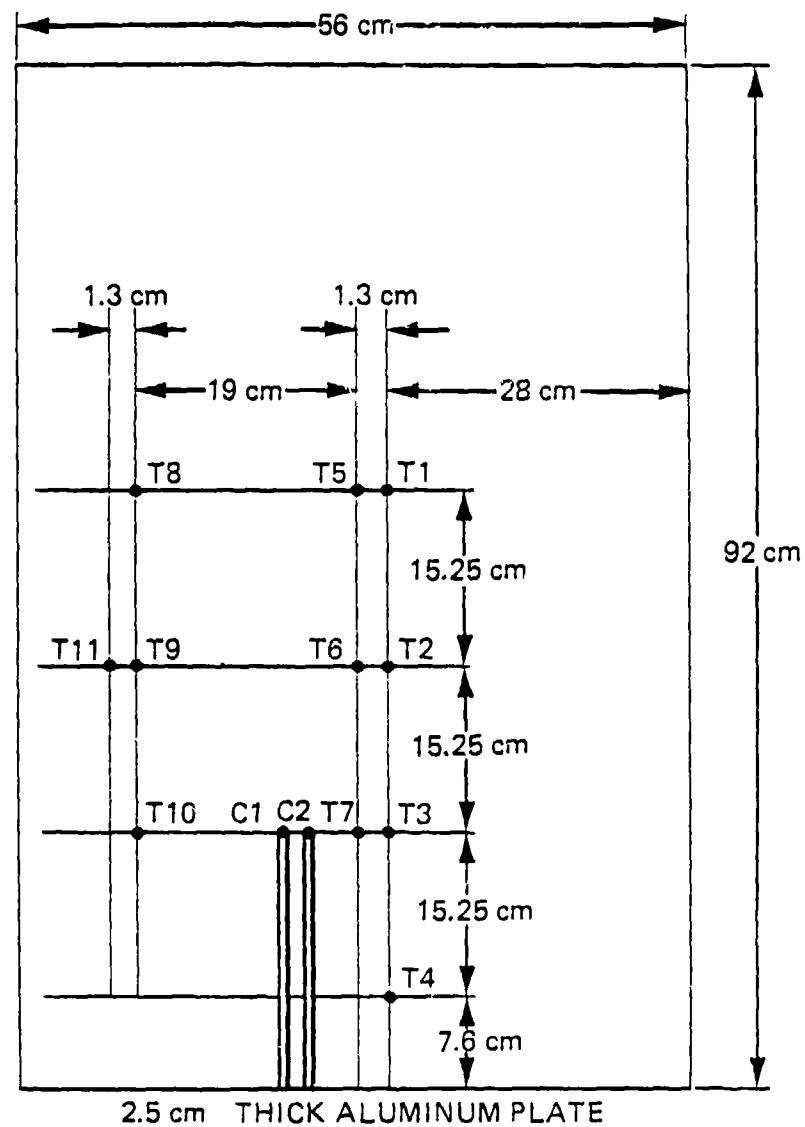


Figure 3-2 Instrumented witness plate, Shot 23.

bipolar pulses. The pulse train was displayed and photographed on a raster type oscilloscope. A sketch of this system is shown in Figure 3-3.

The piezoelectric pin gages generated a voltage when subjected to a mechanical disturbance: force, stress, pressure or acceleration. The output was coincident in time with the occurrence. The voltage output was unipolar and was transferred via coaxial cable to an amplifier and recorded on a wide-band II FM track of a magnetic tape recorder. The system had a risetime capability of 1  $\mu$ s. A sketch of this system is shown in Figure 3-4.

The PCB quartz diaphragm gages, purchased with built-in source followers, were operated in the voltage mode. Power was supplied by PCB signal conditioners that furnished constant current to the gage electronics and decoupled the signal for recording on oscilloscopes equipped with cameras. The transfer cable from the signal conditioner to the gage was RG58/cu. A sketch of this system can be seen in Figure 3-5.

Dynasen's carbon shock pressure gage consists of a thin carbon piezo-resistive element that is connected to two electrical leads and encapsulated between two layers of insulator using epoxy resin as filler and binder. The useable range of application is 0 to  $5 \times 10^6$  kPa (0 to 50 kbar). The gage has a negative coefficient of resistance with increasing pressure. The circuit diagram is shown in Figure 3-6.

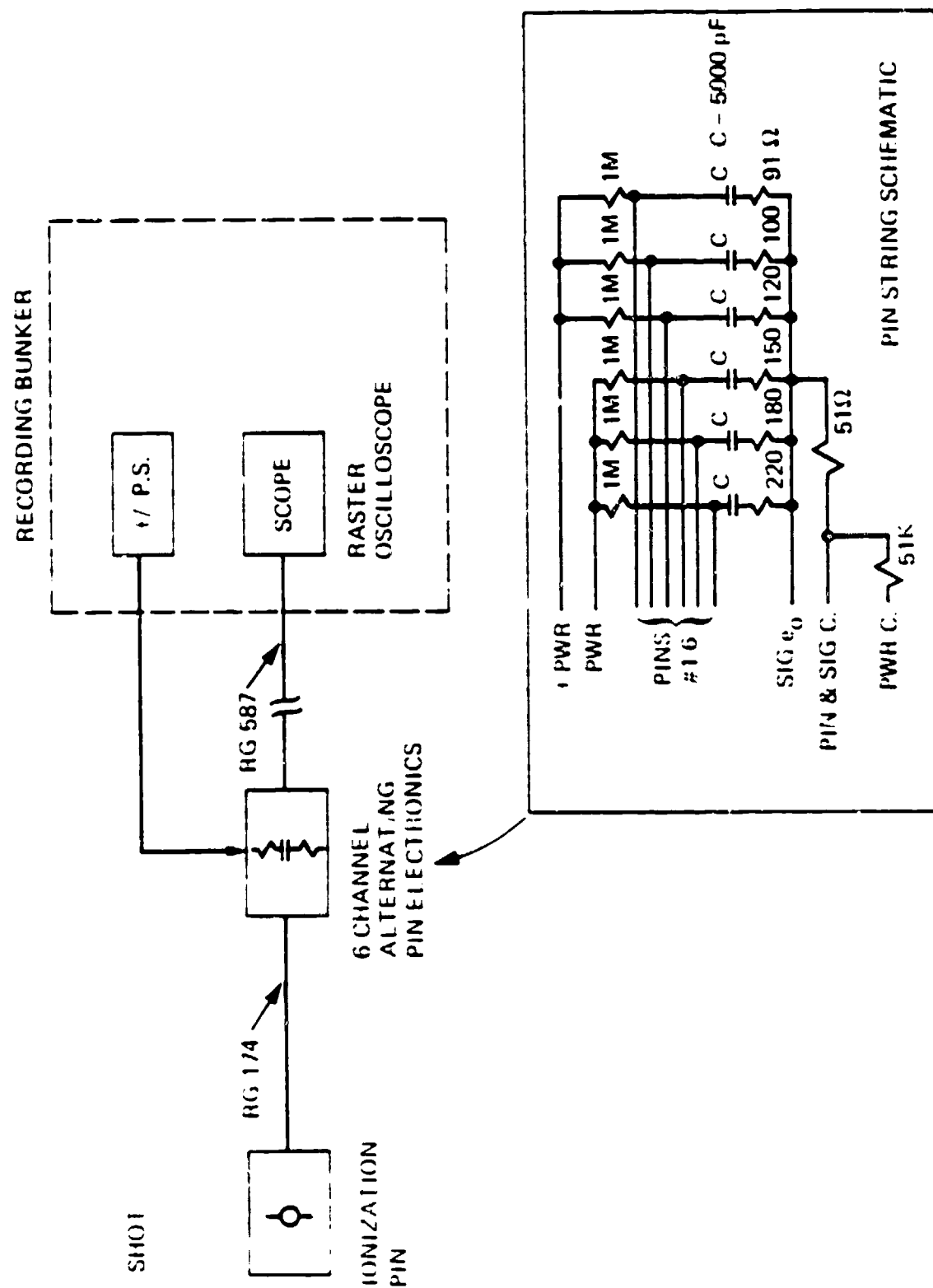


FIGURE 1-3 Ionization Pin system.



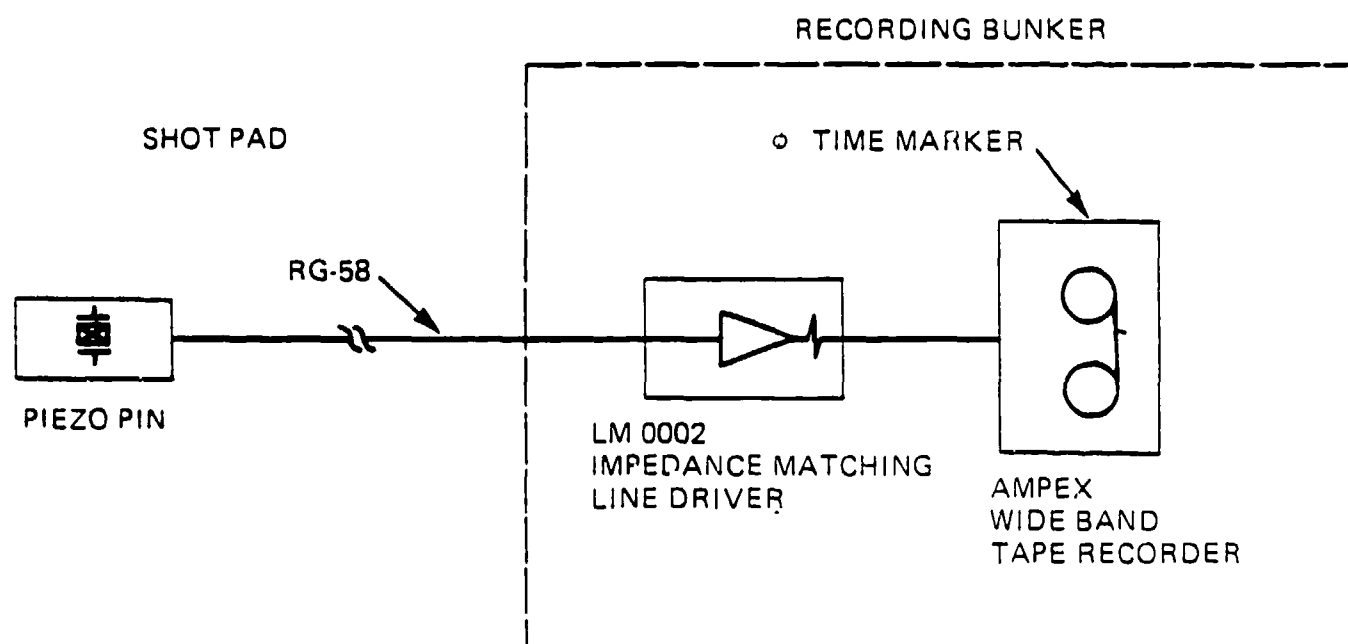


Figure 3-4 Time-of-arrival Pin system.

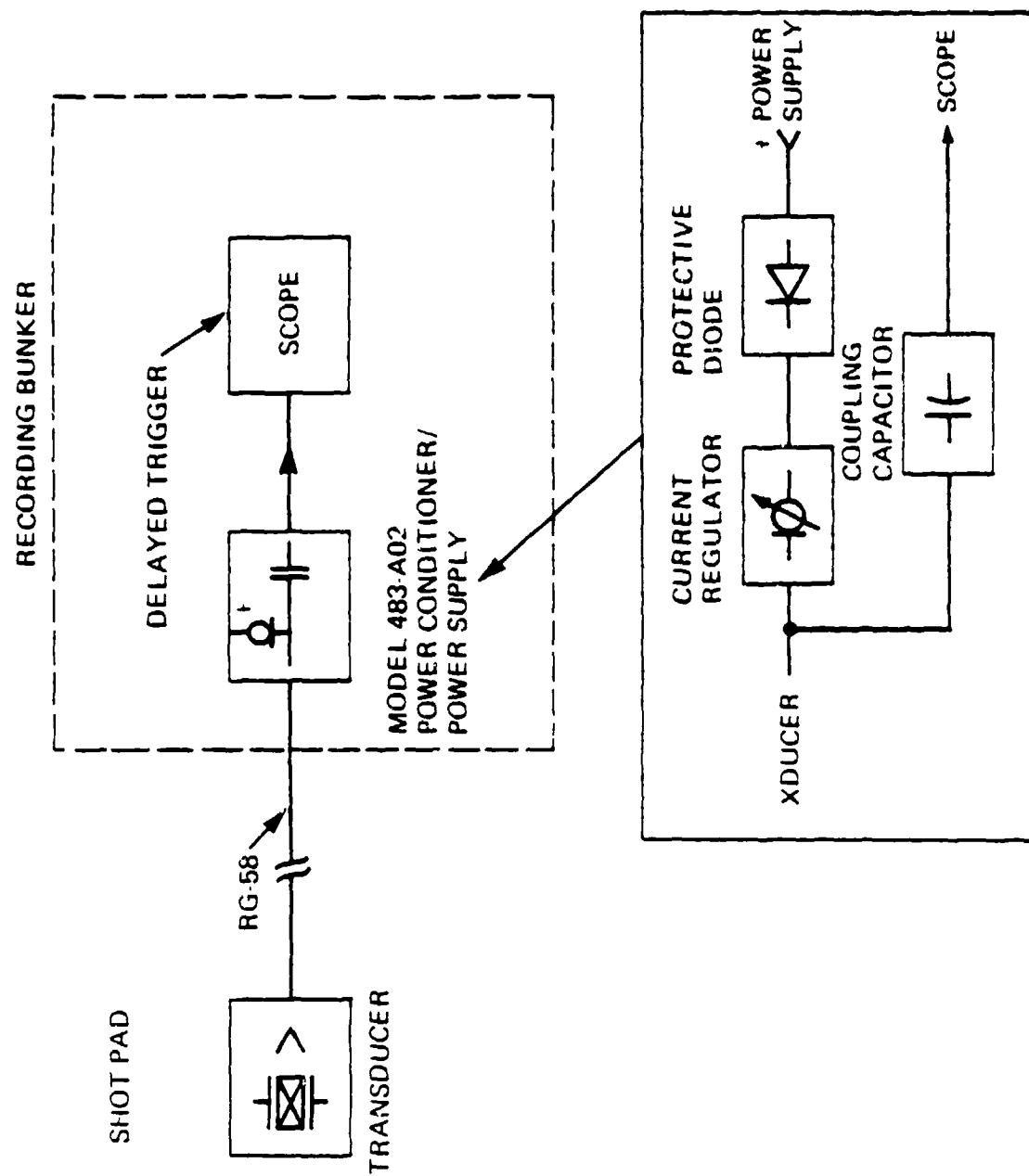


Figure 3-5 P.C.B. pressure recording system.

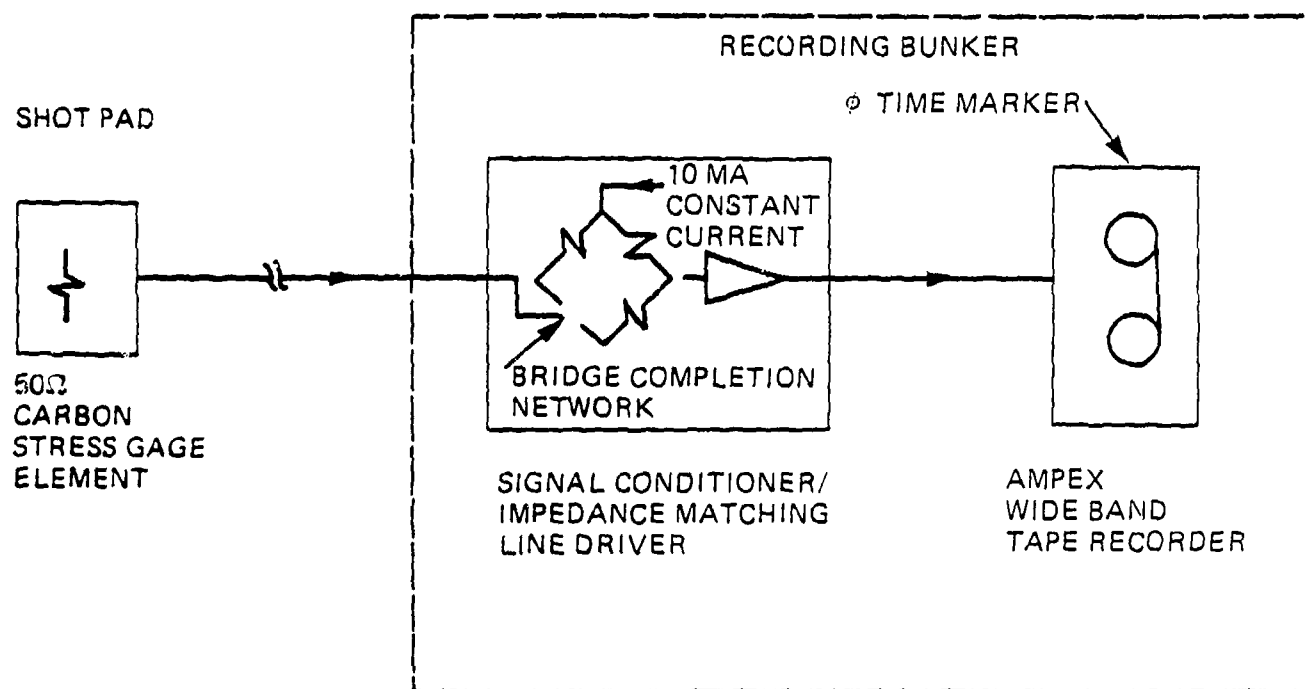


Figure 3-6 Carbon stress gage recording system.

The passive crush gages consist of a 0.476 cm diameter copper ball resting between a hardened steel piston and anvil. Pressure drives the piston against the copper ball causing the ball to deform. Deformation is proportional to pressure. Figure 3-7 shows a calibration curve where the 1/e decay time of the pressure is predicted at 100  $\mu$ s. The curve was calculated by determining the first positive maximum of  $S(t)$ ,  $S(T)$  being the solution of  $ms + K(s)$ .  $S(t) = AP_m \exp (-t/t_0)$  for  $S(0) = S(0) = 0$  where

$S$  = piston displacement  
 $m$  = mass of piston + 1/3 mass of ball  
 $A$  = piston area  
 $P_m$  = peak pressure  
 $t_0$  = 1/e decay time of pressure

This method follows essentially the format suggested in (8), except the reference assumes a constant  $K$  which yields a closed form expression for  $S$ , but is not realistic.  $K$  therefore was evaluated as a function of  $S$ , by selecting 10 equidistant pairs  $(S, K)$  from the static calibration table and determining the LSF (least squares fit) to a parabola. Figure 3-8 shows a typical experimental setup for one of the early thin ANFO experiments, shot 13.

3.1.2 Results Summary. In all, 23 thin ANFO experiments were performed during this test series. Table 3-1 summarizes these experiments and some of the other tests performed during the program. This section summarizes 22 of the thin ANFO experiments. Test 26, the final thin ANFO experiment, will be

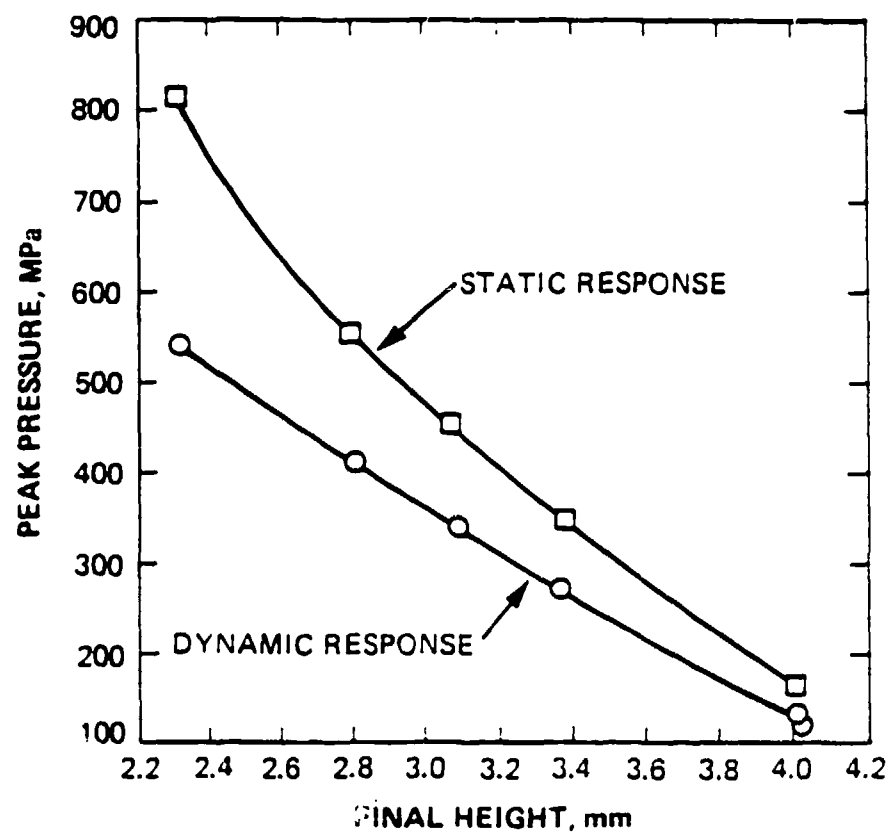


Figure 1-7 Calibration curves for copper crush balls.



Figure 3-8 Experimental setup, Shot 13.

TABLE 3-1

| THIN ANFO EXPERIMENTS - SUMMARY TABLE |        |       |       |        |      |           |           |              |            |
|---------------------------------------|--------|-------|-------|--------|------|-----------|-----------|--------------|------------|
| ANFO EXPERIMENT                       |        |       |       |        |      |           | DATA      |              |            |
| Test                                  | A (cm) | L (m) | W (m) | V (cm) | V/A  | DET       | D in ANFO | TOA on Plate | P on Plate |
| 1                                     | 5      | 0.6   | 0.6   | 50     | 10.0 | PC        |           |              |            |
| 2                                     | 5      | 0.6   | 0.6   | 50     | 10.0 | PC        |           |              |            |
| 3                                     | 5      | 0.6   | 0.6   | 50     | 10.0 | PC        |           |              |            |
| 4                                     | 7.5    | 0.6   | 0.6   | 50     | 6.7  | PC        | X         | X            |            |
| 5                                     | 7.5    | 0.6   | 0.6   | 50     | 6.7  | PC        | X         | X            |            |
| 6                                     | 7.5    | 0.6   | 0.6   | 50     | 6.7  | PC        | X         | X            |            |
| 7                                     | 7.5    | 0.6   | 0.9   | 50     | 6.7  | PC        | X         | X            | X          |
| 8                                     | 7.5    | 0.6   | 0.9   | 50     | 6.7  | PC        | X         | X            |            |
| 9                                     | 7.5    | 0.6   | 0.9   | 50     | 6.7  | PC        | X         | X            |            |
| 10                                    | 12.5   | 0.6   | 0.9   | 83.3   | 6.7  | PC        | X         |              |            |
| 11                                    | 12.5   | 0.6   | 0.9   | 83.3   | 6.7  | PC        | X         |              |            |
| 12                                    | 12.5   | 0.6   | 0.9   | 83.3   | 6.7  | C4        | X         |              |            |
| 13                                    | 7.5    | 0.6   | 0.9   | 50     | 6.7  | PC        | X         |              | X (static) |
| 14                                    |        |       |       |        |      |           |           |              |            |
| 15                                    | 7.5    | 0.6   | 0.9   | 50     | 6.7  | PC        | X         |              | X (static) |
| 16                                    | 7.5    | 0.6   | 0.9   | 50     | 6.7  | PC        |           |              |            |
| 17                                    |        |       |       |        |      |           |           |              |            |
| 18                                    |        |       |       |        |      |           |           |              |            |
| 19                                    |        |       |       |        |      |           |           |              |            |
| 20                                    |        |       |       |        |      |           |           |              |            |
| 21                                    | 17.5   | 0.6   | 0.9   | 50     | 2.9  | PC        | X         |              |            |
| 22                                    | 17.5   | 0.6   | 0.9   | 50     | 2.9  | PC        | X         |              |            |
| 23                                    | 7.5    | 0.6   | 0.9   | 50     | 6.7  | PC        | X         |              |            |
| 24                                    | 17.5   | 0.6   | 0.9   | 50     | 2.9  | PC        | X         |              |            |
| 25                                    | 7.5    | 0.6   | 0.9   | 50     | 6.7  | PC        |           | X            |            |
| 26                                    | 7.5    | 1.2   | 1.9   | 30     | 4.0  | PC (line) | X         | X            | X          |

A: ANFO Thickness

DET: How ANFO Detonated

V: Standoff Distance

PC : Primacord

COMMENTS

disarmed  
no detonation  
partial detonation{ D "valley" in  
ANFO near  
booster{ D<sub>max</sub> = 0.28 cm/μs{ D<sub>max</sub> = 0.36 cm/μsnot performed  
diluted NM  
3 tests, Al/ANFOAirblast experiment  
"  
"{ D<sub>max</sub> > 0.37 cm/μs  
Al/ANFOANFO pins, P  
measurements lostD<sub>max</sub> = 0.325 cm/μs

discussed separately. Tests 14 and 17 were not performed, and tests 18, 19 and 20 were airblast experiments and will be discussed separately in Section 3.4. As a note of clarification, Test 16 in Table 3-1 was actually composed of three experiments, 16a, 16b, and 16c. All were tests of the detonation properties of thin sheets of aluminized ANFO.

Tests 1, 2, and 3 were performed with an ANFO thickness of 5 cm, and with a primacord booster. It was found in these initial 3 tests that it was not possible to obtain full detonation of the ANFO sheets this thin. Therefore, all remaining tests were performed with ANFO thicknesses (A) of greater than or equal to 7.5 cm.

Tests 4, 5, and 6 had an ANFO thin sheet thickness of 7.5 cm, with the sheet located 50 cm above the surface. Figure 3-9 shows the detonation velocity versus range in the thin ANFO for these three experiments as determined from the time of arrival pin data within the ANFO charge itself. It was in these three experiments that the presence of a "valley" in the detonation velocity near the primacord booster was first noticed. It seemed that the ANFO was being overdriven, causing the detonation velocity to drop to below 1 mm/ $\mu$ s near the booster before it began to rise. In Figure 3-9 the detonation velocity continues to rise along the entire length of the tray, reaching a velocity at the end of the tray of around 2 mm/ $\mu$ s. It was felt that the length of the tray was too short to obtain the maximum detonation velocity for this thickness. Thus, in all following experiments, the tray length was increased from 0.6 to 0.9 meters.



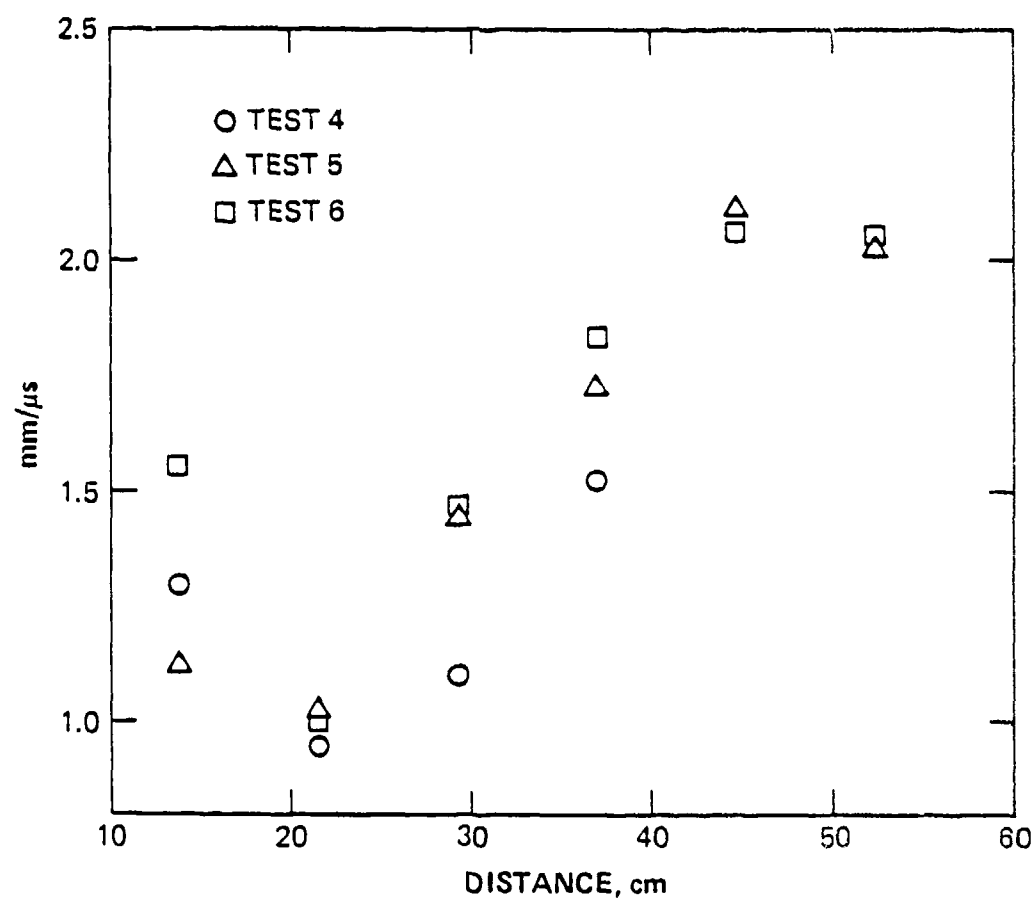


Figure 3-9 Propagation velocity in ANFC versus distance from booster, Tests 4, 5, and 6.

Figure 3-10 shows the detonation velocity,  $D$ , versus distance from the booster as derived from TOA data on Tests 7, 8, and 9. These experiments had an ANFO thickness of 7.5 cm and the tray was located 50 cm from the ground surface. Figure 3-10 shows that the detonation velocity becomes constant at about 0.27 cm/ $\mu$ s towards the end of the sheet. Thus, the length of the tray was considered to be long enough. The measured detonation velocity, however, was still only 50 percent of the C-J detonation velocity in bulk ANFO, (about 0.51 cm/ $\mu$ s). The thickness of the ANFO was then changed to 12.5 cm, and Tests 10 and 11 were performed. The results of these experiments (also shown in Figure 3-10) show that the maximum value of  $D$  rises to about 0.36 cm/ $\mu$ s. This figure was substantially higher than  $D$  for the previous ANFO experiments, but still did not approach the ideal C-J detonation velocity. An additional test within an ANFO thickness of 12.5 cm, labeled Test 12, was fired using a C4 booster instead of primacord. The results obtained concerning the detonation velocity in the ANFO were no different on this test than those reported for Tests 10 and 11.

In the preliminary charge design for the STANDARD SOURCE experiment, a "first order" correction to the ANFO detonation velocity was made, based on data from a previous program. This correction involved using a constant detonation velocity for thin sheets of ANFO which was lower than the nominal C-J detonation velocity. The early thin ANFO experiments discussed above showed that, close to the booster, the detonation velocity was certainly not a constant, its value dependent upon the absolute thickness of the ANFO sheet. Taken by itself, this is a minor problem. However, it is also necessary to obtain the peak pressure and the

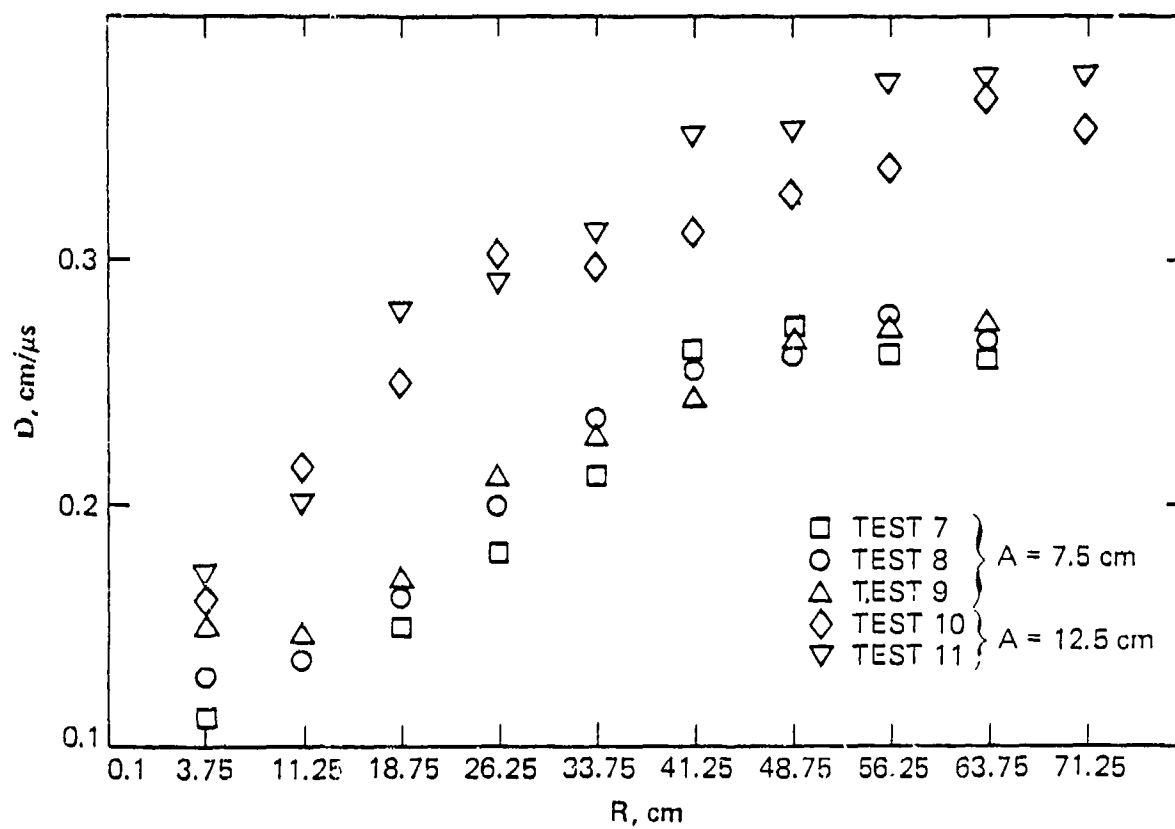


Figure 1-1 Retention velocity in WFF versus distance for 7.5 cm test, Tests 7-11.

total impulse on the surface for a given charge thickness to design the STANDARD SOURCE charge.

Attempts to measure pressure on the plate in the above experiments were not very successful. Many gages were destroyed in the process. Only on test Test 7 was a peak pressure measured: Gage 1 recorded a peak pressure of 483 MPa, and Gage 2 recorded a peak pressure of 262 MPa. There is a large spread between these two measurements which were made at essentially the same range, and both gages were subjected to higher than expected pressures. This effect can be seen by using Equation 2.6 with  $V/A = 6.7$ , yielding a calculated peak pressure of 113 MPa. One-dimensional calculations could not explain these high measured pressures.

In a further attempt to measure pressure on the plate, another experiment, Test 13, was performed. This experiment contained the TOA pins in the ANFO charge and also 6 copper crush gages mounted in the plate at various ranges. The TOA data in the ANFO agreed well with that from the earlier experiments with 7.5 cm thickness ANFO. The Test 13 copper crush gage results are shown in Table 3-2. The pressures derived from Gages 5 and 6, located near the pressure gages in the previous tests, also indicated high peak pressure. However, the gages at the ranges closer to the booster showed lower pressures. Some evidence of a pressure gradient, with range, is also seen in this data.

At this point in the program it was decided to try a different type of explosive. Dr. M. Finger, a consultant from the Lawrence Livermore Laboratory, recommended the use of

TABLE 3-2

## COPPER CRUSH GAGE RESULTS: TEST 13

| GAGE NUMBER | SERIAL NUMBER | RANGE FROM<br>BOOSTER | PEAK PRESSURE FROM<br>STATIC CRUSH CURVE |
|-------------|---------------|-----------------------|--|
| 1           | 38051         | 47 cm                 | 80 MPa                                   |
| 2           | 39557         | 47 cm                 | 90 MPa                                   |
| 3           | 38579         | 80 cm                 | 98 MPa                                   |
| 4           | 34447         | 80 cm                 | 107 MPa                                  |
| 5           | 38064         | 94 cm                 | 160 MPa                                  |
| 6           | 38661         | 94 cm                 | 305 MPa*                                 |

\*Damage to gage indicated severe impact with ground or plate (rebound)

TABLE 3-3

COPPER CRUSH GAGE RESULTS: TEST 15  
(DILUTED NITROMETHANE)

| GAGE NUMBER | SERIAL NUMBER | RANGE FROM<br>BOOSTER | PEAK PRESSURE FROM<br>STATIC CRUSH CURVE |
|-------------|---------------|-----------------------|--|
| 1           | 39557         | 47 cm                 | *  |
| 2           | 38051         | 47 cm                 | 405 MPa                                  |
| 3           | 34447         | 80 cm                 | 260 MPa                                  |
| 4           | 38064         | 80 cm                 | 485 MPa                                  |
| 5           | 38661         | 94 cm                 | 350 MPa                                  |
| 6           | 38579         | 94 cm                 | 335 MPa                                  |

\*Gage wedged in plate, data lost.

diluted, sensitized nitromethane. The mixture used is as follows:

|                       | <u>Percent</u> |
|-----------------------|----------------|
| Nitromethane          | 65             |
| Alcohol               | 30             |
| Ethylenediamene (EDA) | 5              |

This test was designated Test 15. The explosive thickness was 7.5 cm, and the test geometry was the same as had been used in the previous ANFO experiments. The TOA pin data in the explosive indicated an average detonation velocity of 0.55 cm/ $\mu$ s; this average is consistent with the C-J detonation velocity in diluted nitromethane. Also, copper crush gages were placed in the steel plate beneath the explosive. The results of these measurements are given in Table 3-3. The peak measured pressures are higher than those recorded for ANFO using the copper crush gages, and the data seem to be more consistent than the ANFO results.

Four experiments were then performed to see if the addition of aluminum chips or aluminum powder to ANFO would increase the detonation velocity. These were Tests 16a, 16b, 16c, and 23. All tests were performed for an ANFO thickness for a 7.5 cm with the test bed dimensions (62 x 94 cm) being the same as in the previous ANFO experiments. Primacord boosters were used. Test 16a was an aluminized ANFO mixture of 3 percent aluminum chips, 97 percent ANFO which was commercially available from Gulf Oil Company, Flagstaff, Arizona. Time-of-arrival results from pin data within the ANFO charge indicated a very erratic detonation velocity. Therefore, the next three experiments

(Tests 16b, 16c, and 23) used ANFO which was mixed with purified aluminum powder at the Tracy Test Site. Test 16b consisted of 97 percent ANFO and 3 percent aluminum powder; Test 16c and 23 consisted of 94 percent ANFO and 6 percent aluminum powder. The powder was mixed by sprinkling the calculated amount of ANFO over the charge and then mixed by rolling the entire charge inside of the paper barrel to gain uniform consistency. Figure 3-11 shows the detonation velocity in the ANFO charge from Test 16b and 16c as calculated from the pin TOA data within the charge. The data from Test 23 agreed well with that obtained on Test 16c. These data indicated that the detonation velocity in the ANFO was enhanced to some degree by the addition of the aluminum powder. The average detonation velocity at the end of the ANFO sheet was approximately 0.30 cm/ $\mu$ s, as compared to a detonation velocity of about 0.27 cm/ $\mu$ s as measured in the previous tests using an ANFO charge thickness of 7.5 cm.

Three tests (Tests 21, 22, and 23) were then performed with an ANFO thickness of 17.3 cm. TOA data in the ANFO charge were recorded for all three experiments and no attempt was made to measure pressure or time-of-arrival on the plate. Figure 3-12 shows the detonation velocity in the ANFO charge versus distance from the booster for these three experiments. The detonation velocity levels off at the end of the charge at about 0.36 to 0.38 cm/ $\mu$ s. Thus, as expected, the detonation velocity in the steady state continues to increase as the charge thickness is increased.

A final experiment (Test 25) was performed to attempt again to obtain pressure measurements on the plate. This shot had an

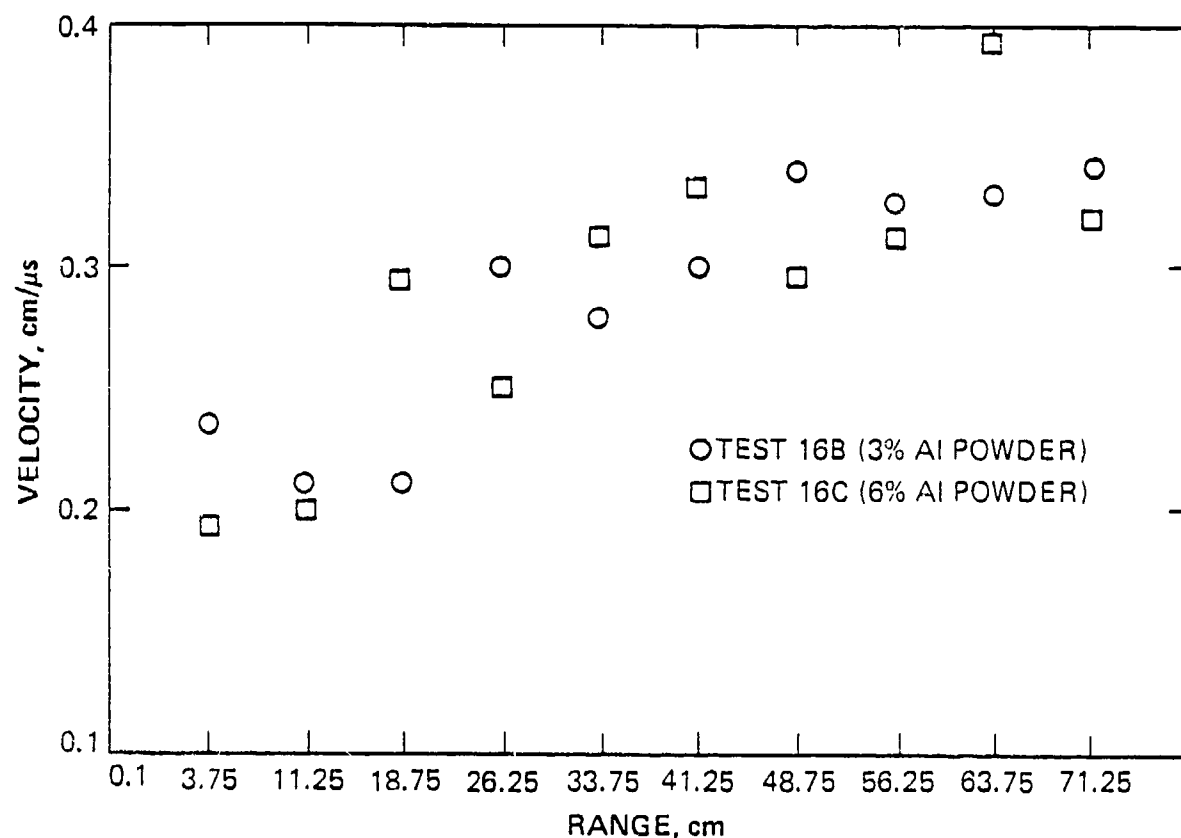


Figure 3-11 Detonation velocity in ANFO charge, Tests 16B and 16C (aluminized ANFO).



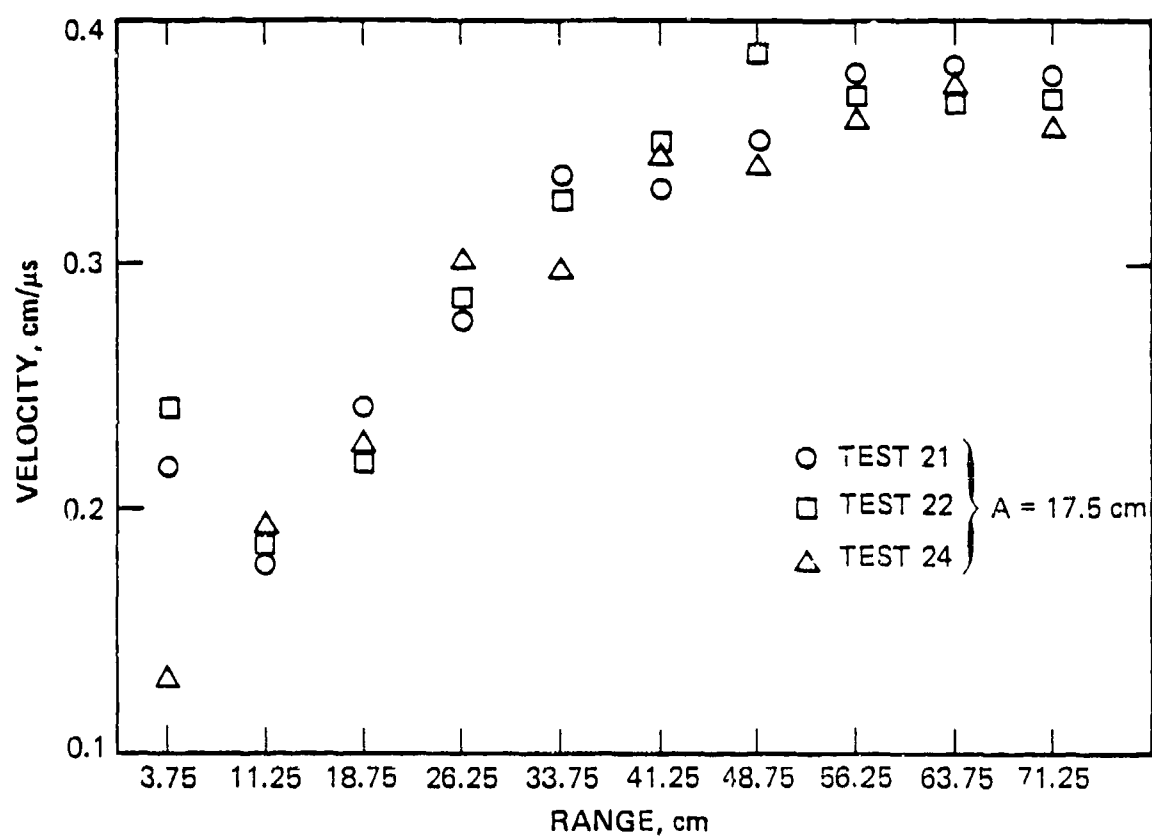


Figure 3-12 Detonation velocity in ANFO versus distance from booster, Tests 21, 22, and 24.

ANFO thickness of 7.5 cm located 50 cm about the plate. The plate was made of aluminum and was segmented to decrease chance of spurious signals reaching the pressure gages. Data on the detonation velocity in the ANFO were not obtained on this experiment and the pressure gages all failed before the peak pressure was reached. However, some TOA data on the plate were obtained from the pressure gages. These data are shown in Figure 3-13. The data from the pins which were located 7.6 cm above the plate indicated an average velocity of 0.33 cm/ $\mu$ s. The data from the pins which were flush with the plate indicated a time-of-arrival consistent with the velocity of 0.33 cm/ $\mu$ s only to a position about halfway down the charge. After that point, the slope of the TOA curve becomes 0.66 cm/ $\mu$ s, or exactly double the previous value. Very little analysis of these data was performed because of the loss of TOA data within the ANFO charge itself.

3.1.3 Computations and Modeling in One and Two Dimensions. Computer calculations were performed during this phase of the program. The purpose of these calculations was to model the results of the early thin ANFO experiment. As has been seen in the previous section, the majority of the data consisted of TOA data and the derived detonation velocity,  $D$ , in the ANFO charge itself. To perform the STANDARD SOURCE design, it was necessary to obtain the peak pressure and the total impulse at the ground surface. The early thin ANFO experiments obtained very few of these data. It was felt that if calculations could model the detonation velocity in the ANFO properly for each of the thicknesses for which experimental data existed, the peak pressures and total impulses on the ground surface could then be calculated.

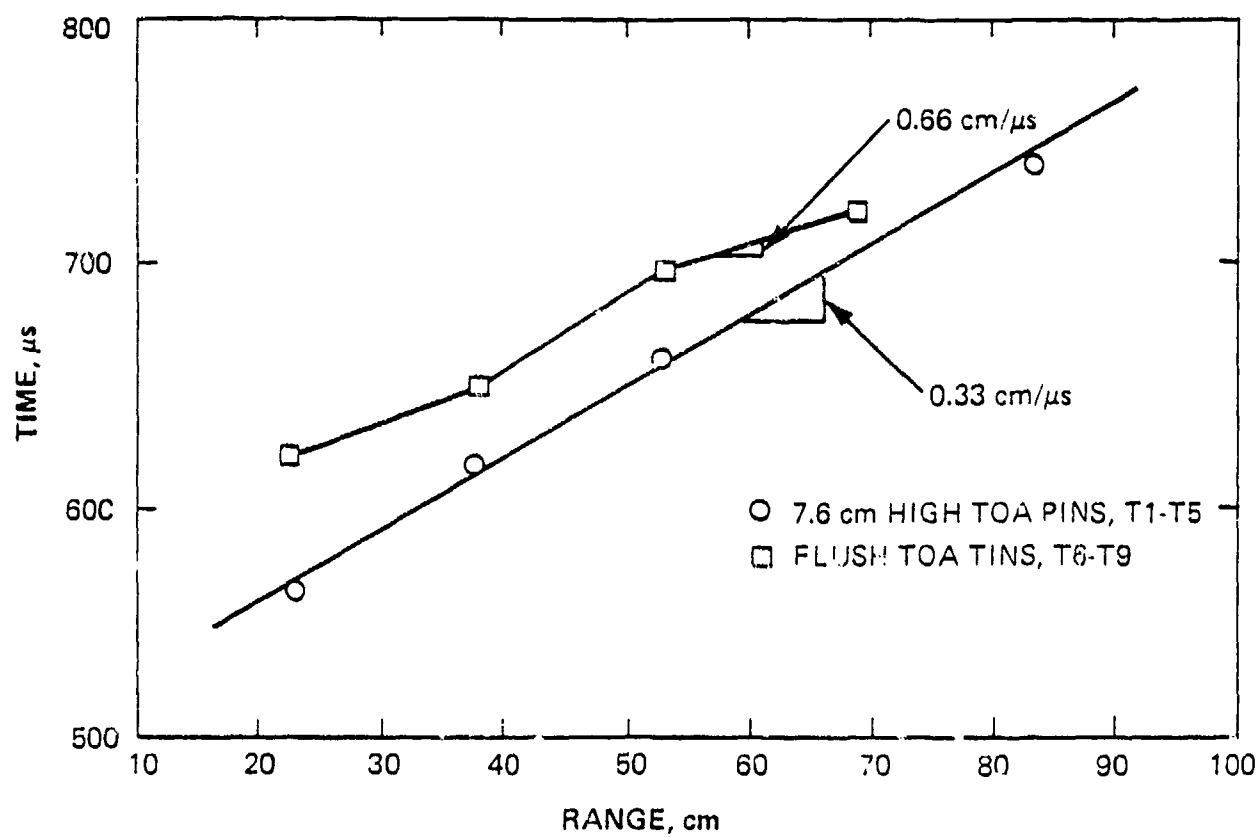


Figure 3-13 TOA data from pins on and above the segmented aluminum plate, Test 25.

Several different computational approaches were tried. The most successful of these approaches employed a model for the burn of the ANFO which assumed that the energy was not all released at the shock front [as assumed by the JWL detonation model (Reference 6)], but that after initiation of the burn of the ANFO, some length of time was necessary to complete the detonation. The computational approach was essentially to model the "non-ideal" nature of the ANFO explosive, as was being observed in these early experiments.

To model the ANFO behavior, a "grain burn" model was implemented in the one- and two-dimensional computer codes. This model was developed previously for DNA on another program (Reference 9), and is briefly summarized below. The model assumed that the chemical energy of the explosive is released over a finite period of time after the arrival of the detonation wave. It also assumed that an activation energy is required to initiate a release of energy from the ANFO grain. Thus, the grain burn model assumed:

$$\frac{dF}{dt} = G(E_a, \tau), \text{ where} \quad (3.1)$$

F is the fraction of ANFO consumed at time, t,  $E_a$  is the activation energy, and  $\tau$  is the time over which the total energy of the ANFO grain is completely released. The model further assumed that:

$$E_a = \alpha E_0. \quad (3.2)$$

Thus, the activation energy is a simple function of the total energy release,  $E_0$ .

The calculational geometries are shown schematically in Figure 3-14. The 1-D calculation assumed planar symmetry. The charge was detonated at the left and detonation proceeded to the right. To match the data for the 7.5-cm ANFO experiment, it was found that a larger value of  $\tau$  (225  $\mu$ s) was required than that for the 12.5 cm experimental results (100  $\mu$ s). The value of  $\alpha$  required was the same for both thicknesses (0.05). This indicated that surface rarefactions in the experiment were controlling the time over which the ANFO was burned, and the results seemed reasonable. It should be pointed out, however, that in the thin ANFO experiments the detonation was initiated at a single point and not along a line. Therefore, the one-dimensional calculations were only an approximation of the experimental data.

The two-dimensional calculations also assumed planar symmetry, and the charge was detonated at the left and detonation proceeded to the right. Six computational zones were contained within the ANFO charge, and void regions were placed on both sides of the charge so that rarefactions could be modeled. No attempt was made to put a ground surface (or reflecting boundary) in the calculation.

To match the data from the early thin ANFO experiments, a higher value of  $\alpha$  (0.15) and lower values of  $\tau$  ( $\sim$  50  $\mu$ s) were required. It should be pointed out that the two-dimensional calculations also assumed a line detonation instead of a single point detonation as used in the experiments.

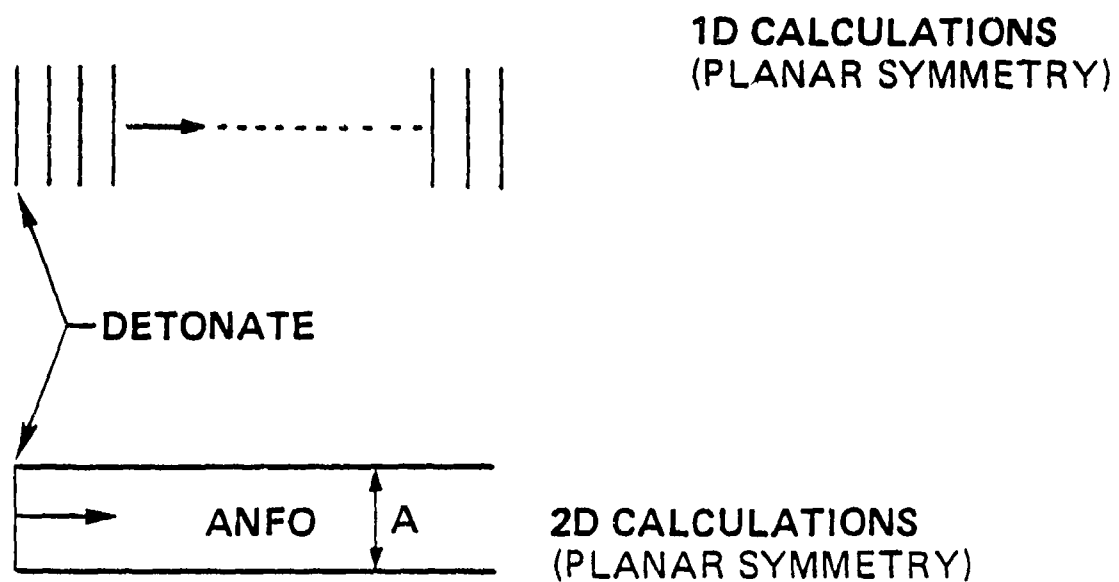


Figure 3-14 Geometries for thin ANFO calculations.

These computational efforts indicated that the ANFO was not behaving as an ideal explosive in thin sheets and that further experimental and calculational work would be required to understand the ANFO detonation processes.

### 3.2 FINAL THIN ANFO EXPERIMENT

The final thin ANFO experiment (Test 26) was drastically redesigned to incorporate the following features:

- The lateral dimensions of the charge container were increased to eliminate edge effects.
- The charge height above the plate was reduced from 50 to 20 cm for the same reason.
- The charge was ignited with multiple detonators across the center line to provide a line ignition.
- The line charge was placed 33 cm from the left hand boundary to provide relief from rarefactions from that boundary.
- High speed framing camera coverage was incorporated as a diagnostic tool.

3.2.1 Geometry and Instrumentation. Figure 3-15 is a photograph of the test bed. The ANFO tray was 7.5 cm thick and was suspended 20 cm above the test bed. A segmented instrumented aluminum plate was placed below the ANFO tray on a bed of sand. The overhead canopy had wires strung to the ANFO tray to prevent the cardboard bottom from sagging.

Figure 3-16 is a sketch of the segmented aluminum plate. P1, P2, P3, and P4 are carbon pressure gages. T1, T2, T3, T4,



Figure 3-15 Side-on photograph of the setup of the final thin ANFC experiment.



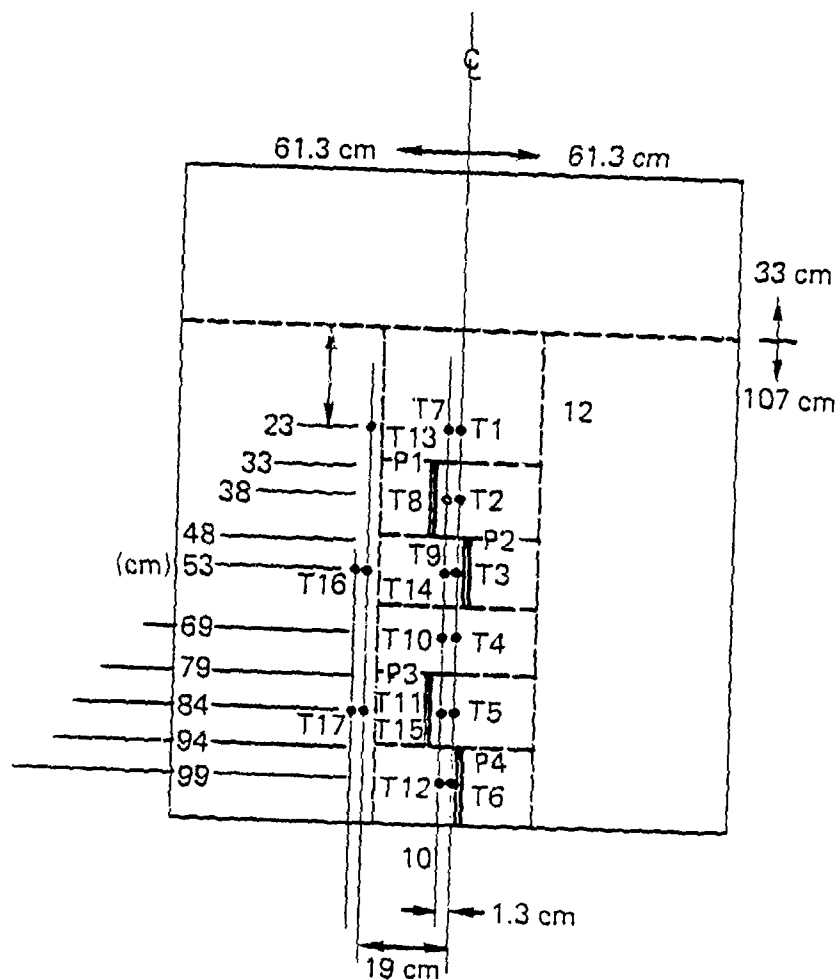


Figure 3-16 Final thin ANFO segmented aluminum plate.

T5, T6, T16, and T17 are piezoelectric TOA gages elevated 7.5 cm above the plate. T7, T8, T9, T10, T11, T12, T13, T14, and T15 are the same type of sensor mounted flush with the plate's surface. The dotted line extending horizontally across the plate was directly beneath the initiation line of the ANFO tray. The vertical center line of the plate was aligned with the vertical center line of the explosive tray.

Line initiation was achieved by stretching a length of 400 grain primacord across the explosive tray at mid-depth (3.75 cm). The primacord was fired by 17 detonators equally spaced along the length of cord. This placed the detonators at 10 cm intervals.

A Scotchlite backdrop was installed to enhance the photography. Figure 3-17 is a background diagram of the backdrop; BW1, BW2, and BW3 are high voltage spark gaps and are used for timing. The mirror was suspended over the ANFO tray at a 45 degree angle to photographically observe edge effects near the end of the tray.

The instrumentation gages, amplifiers, and recording techniques were the same as those described for the earlier ANFO experiments.

3.2.2 Results Summary. The last Standard Source thin ANFO experiment recovered data as follows:

1. TOA (pin) data in the ANFO charge along three lines,

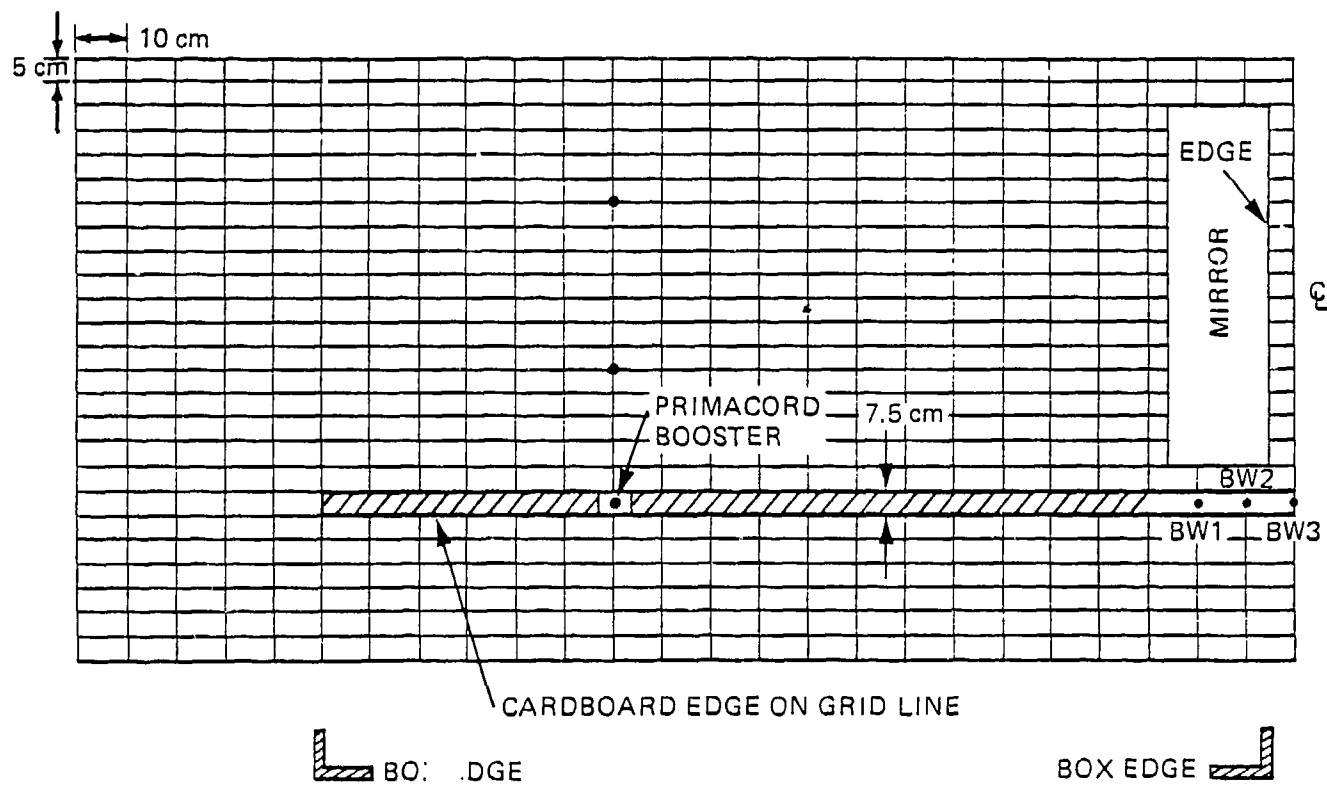


Figure 3-17 Standard source background grid.

2. TOA (pin) data at a height of 76.2 mm (3 inch) above the aluminum plate along two lines,
3. TOA (pin) data flush with the plate along two lines,
4. Pressure data from four pressure gages located on the aluminum plate, and
5. Eighteen frames from the framing camera at 25 micro-second intervals.

It is helpful to begin by looking at the phenomenology as seen from selected frames from the framing camera. Figure 3-18 shows the first frame at time  $T=0$  (the detonation time of the primacord booster). This initial side-on view of the ANFO tray fast frame photograph is included for reference. The vertical lines marked with the two X's indicate the location of the primacord booster. The detonation of the ANFO sheet will proceed from this point to the right and the left, but instrumentation is located only to the right side. The bright spot located to the far right, close to the ANFO sheet, is a bridge wire which was detonated concurrently with the booster detonators. At the bottom of the pictures TOA pins are clearly seen positioned directly above the aluminum plate.

As the detonation proceeds, the ANFO detonation products initially expand more or less spherically. This is shown in Figure 3-19, a photograph of frame six at a time of 150  $\mu$ s. When the detonation products reach the aluminum plate below the charge the expansion is no longer spherical and the products become confined and begin to travel faster in the confined region. This is shown in Figure 3-20, which is frame eight at a time of 200  $\mu$ s. Concurrently, the light intensity of the ANFO detonation products dramatically increases very close to the front of the

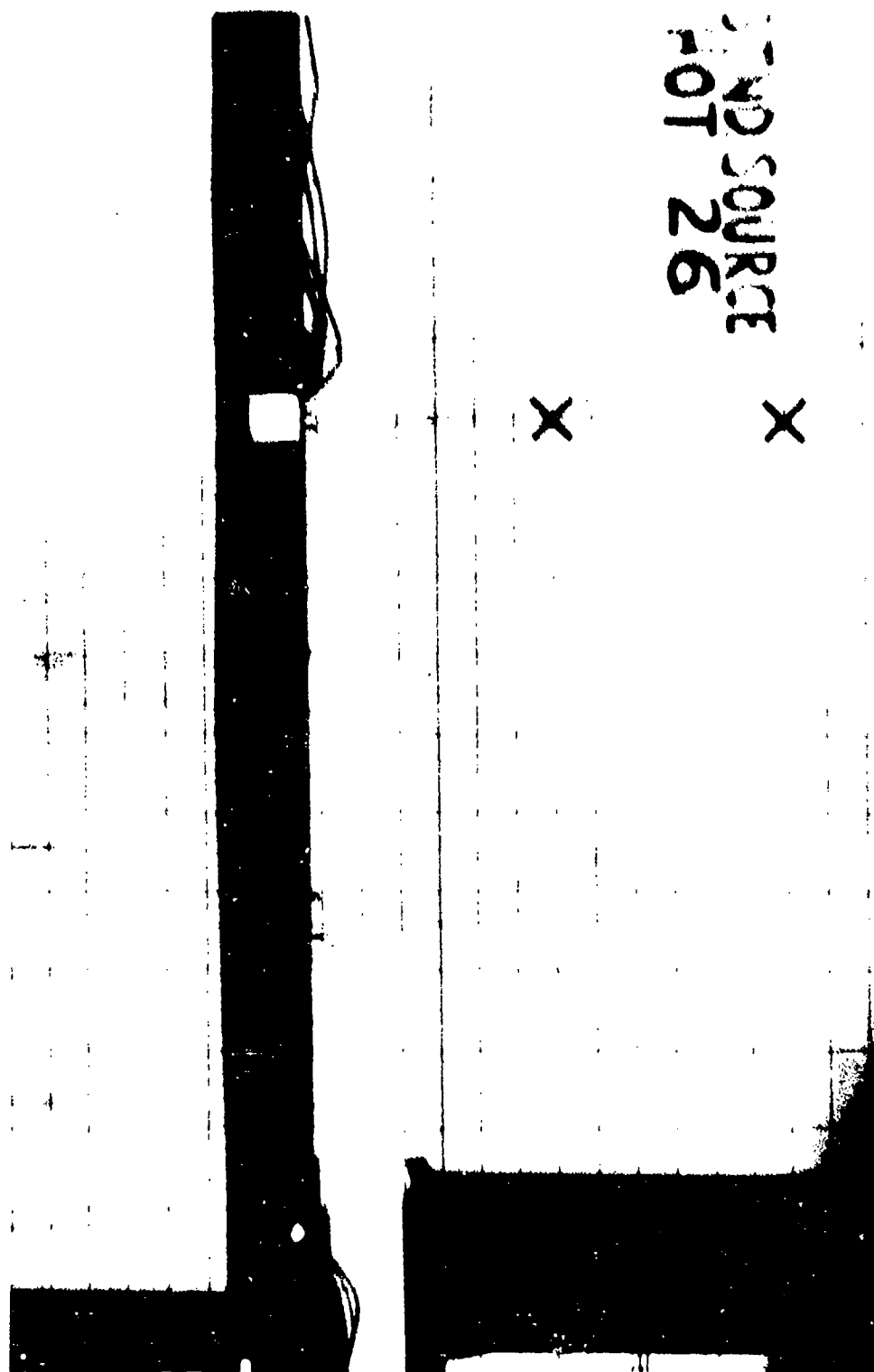


Figure 3-18 Fast camera Frame 1 ( $t = 0 \mu s$ ) side-on setup view of thin ANFO, Test 26.

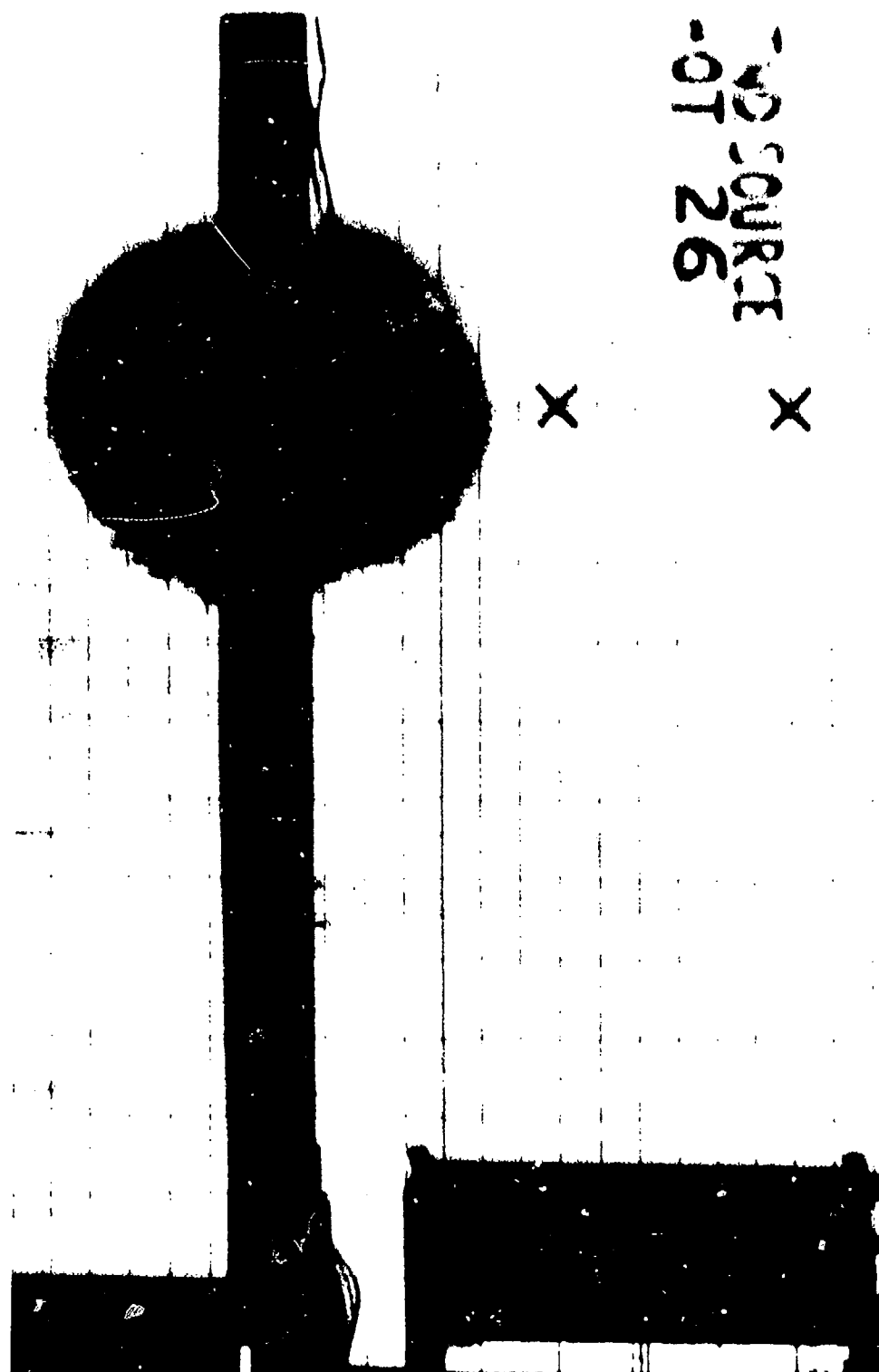


Figure 3-19 Fast camera, Frame 6 ( $t = 150 \mu s$ ) showing early spherical expansion of ANFO detonation products.

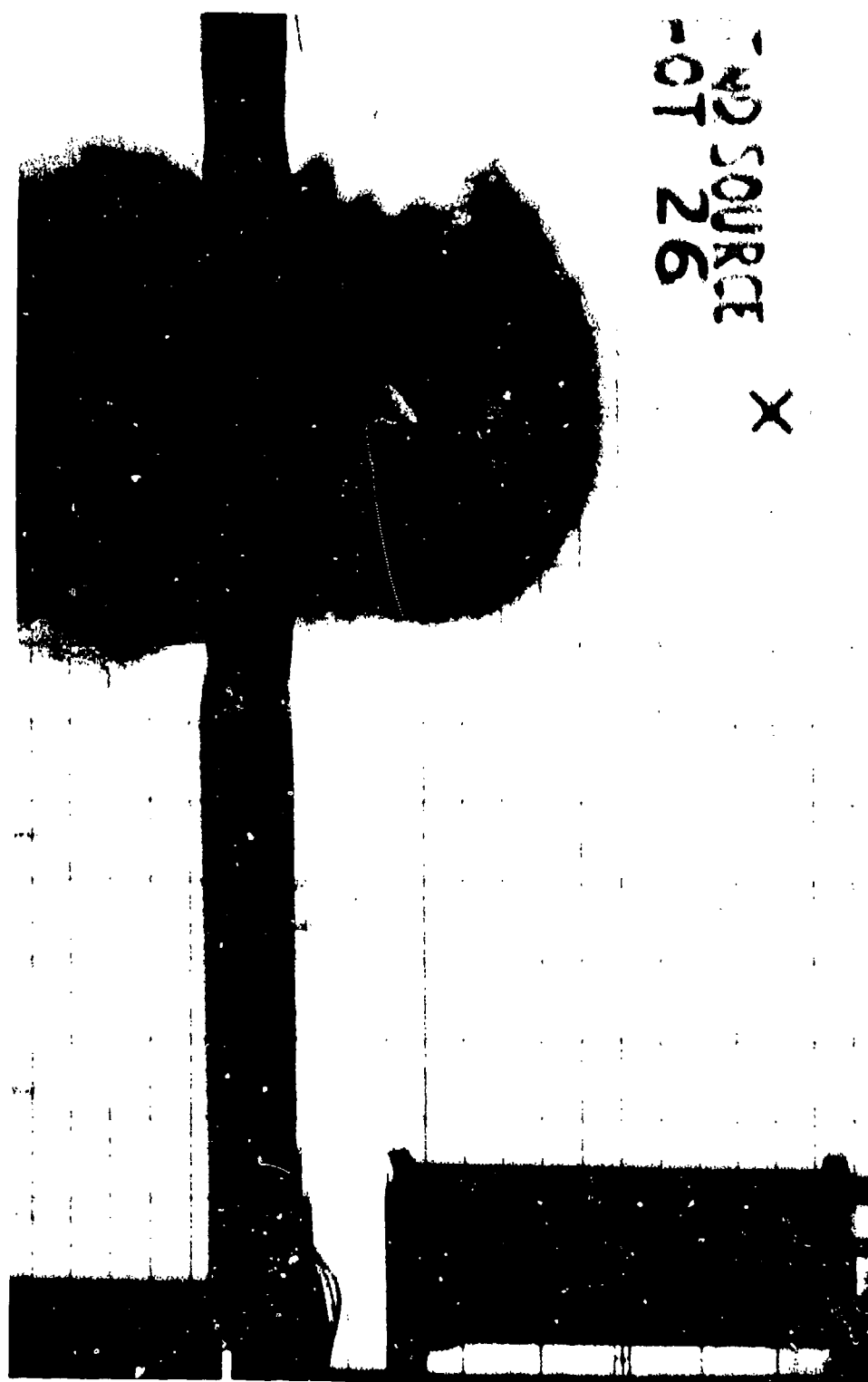


Figure 3-20 Fast camera Frame 8 ( $t = 200 \mu s$ ).

detonation. This is seen clearly in this figure. As the detonation proceeds, this region of greater light intensity expands considerably, and also interacts with the aluminum plate below the charge. As the shock strikes the plate at greater than the critical angle, this interaction creates a Mach shock. This is shown clearly in Figure 3-21, at a time of 275  $\mu$ s. The Mach stem continues to grow in the region between the plate and the charge until the detonation front in that region is almost vertical. This is shown in Figure 3-22, Frame 14 at a time of 350  $\mu$ s. Figure 3-23, frame 16 at a time of 400  $\mu$ s, shows that this Mach stem is actually out ahead of the shock front in the ANFO charge itself towards the end of the experiment.

Data was digitized along four lines from the fast camera photographs. All four lines started at the center of the detonation and proceeded to the right, following the detonation process along the ANFO sheet and in the region between the sheet and the aluminum plate. Lines 1 and 2 were directly above and below the ANFO charge, respectively. Lines 3 and 4 were near the aluminum plate, with line 3 about 0.05 meter above the plate and line 4 flush with it. The digitized data from these four lines are given in Table 3-4 and they will be compared with other TOA data in this section.

The data from the TOA pins within the ANFO charge are given in Table 3-5. Figure 3-24 plots these data for all three sets of pins: rear, center, and front. There is a spread of 20 to 40  $\mu$ s in the timing between the 3 sets of pins at each range. The data at each range were then averaged and the average value plotted in Figure 3-25. For the first 200  $\mu$ s, it is seen that the slope is



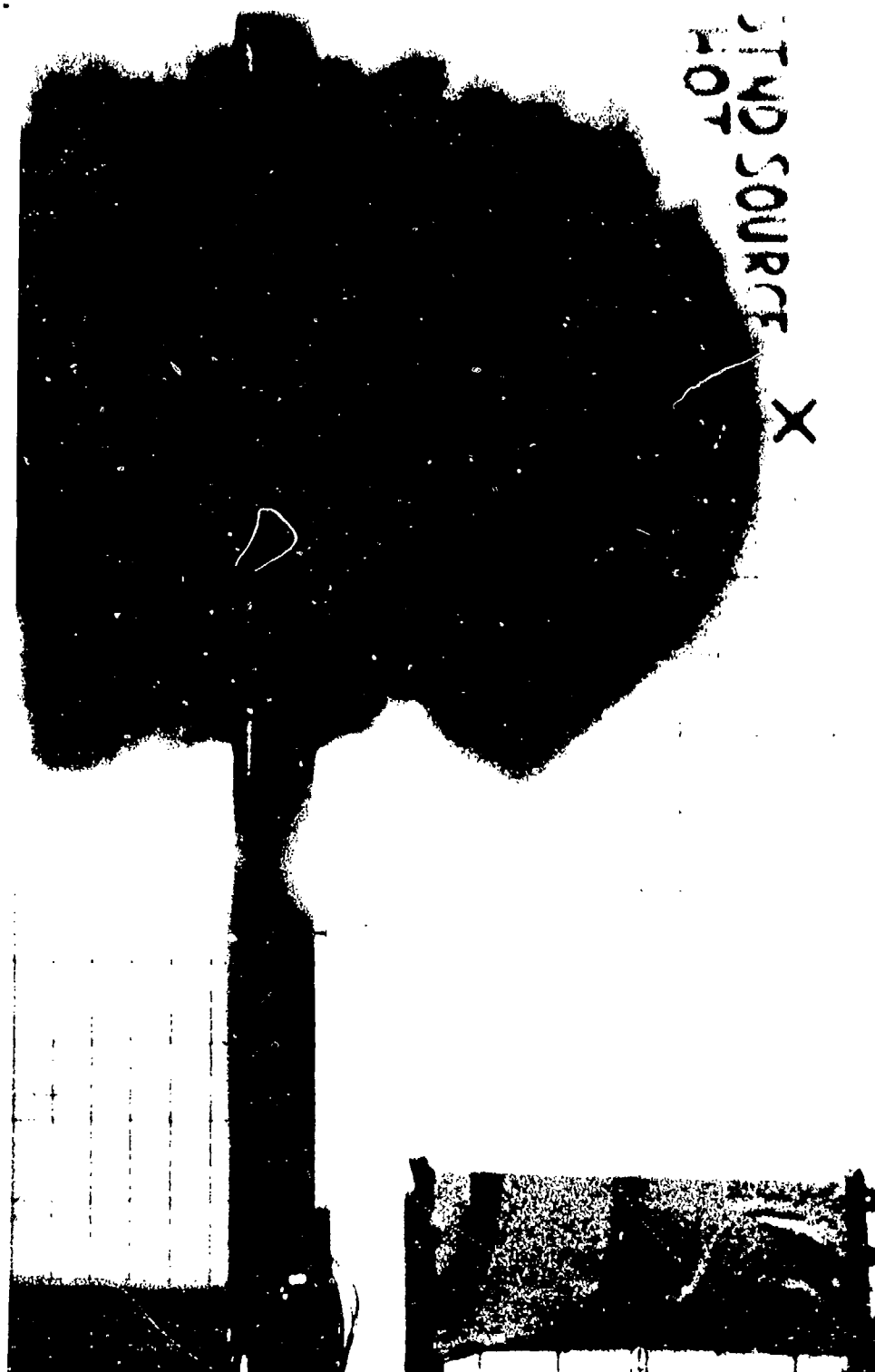


Figure 3-21 Fast camera Frame 11 ( $t = 275 \mu s$ ) showing initial formation of mach stem along aluminum plate.



Figure 3-22 Fast camera Frame 14 ( $t = 350 \mu s$ ), showing further mach stem development beneath the ANFO charge.



Figure 3-23 Fast camera Frame 16 ( $t = 400 \mu s$ ).

TABLE 3-4

TIME-OF-ARRIVAL IN TEST 26, DATA FROM FAST CAMERA PHOTOGRAPHS

| Frame | time (μs) | Line 1 | Line 2 | Line 3 | Line 4 |
|-------|-----------|--------|--------|--------|--------|
| 1     | 25        | .00    | .00    | .00    | .00    |
| 2     | 50        | .06    | .01    | .00    | .00    |
| 3     | 75        | .10    | .10    | .00    | .00    |
| 4     | 100       | .15    | .15    | .00    | .00    |
| 5     | 125       | .20    | .22    | .00    | .00    |
| 6     | 150       | .24    | .26    | (TOA)  | .00    |
| 7     | 175       | .27    | .29    | .18    | (TOA)  |
| 8     | 200       | .33ℓ   | .31    | .26    | .23    |
| 9     | 225       | .40ℓ   | .40ℓ   | .33    | .30    |
| 10    | 250       | .49ℓ   | .47ℓ   | .40    | .33    |
| 11    | 275       | .56ℓ   | .54ℓ   | .43    | .42    |
| 12    | 300       | .64ℓ   | .62ℓ   | .55    | .54    |
| 13    | 325       | .73ℓ   | .70ℓ   | .65    | .64    |
| 14    | 350       | .80ℓ   | .78ℓ   | .73    | .74    |
| 15    | 375       | .88ℓ   | .85ℓ   | .83ℓ   | .85ℓ   |
| 16    | 400       | .96ℓ   | .93ℓ   | .95ℓ   | .96ℓ   |
| 17    | 425       | 1.03ℓ  | 1.00ℓ  | 1.06ℓ  | 1.08ℓ  |
| 18    | 450       | 1.10ℓ  | 1.08ℓ  | --     | --     |

Line 1 - 0.05 m above ANFO charge

Line 2 - 0.05 m below ANFO charge

Line 3 - 0.05 m above aluminum plate

Line 4 - Flush with aluminum plate

ℓ: ANFO gasses clearly become luminescent in photographs.

TABLE 3-5

TOA PIN DATA IN THIN ANFO, TEST 26

| <u>Range (m)</u> | <u>TOA, Set 1<br/>(front) (<math>\mu</math>s)</u> | <u>TOA, Set 2<br/>(center) (<math>\mu</math>s)</u> | <u>TOA, Set 3<br/>(rear) (<math>\mu</math>s)</u> |
|------------------|---|--|--|
| 0.000            | 0   | 0  | 0  |
| 0.075            | 45  | 45   | 53   |
| 0.150            | 67  | 73   | 80   |
| 0.225            | 111   | 118  | 124  |
| 0.300            | 149   | 166  | 165  |
| 0.375            | 175   | 192  | 194  |
| 0.450            | 202   | 222  | 223  |

|       | <u>TOA, Set 4<br/>(front) (<math>\mu</math>s)</u> | <u>TOA, Set 5<br/>(center) (<math>\mu</math>s)</u> | <u>TOA, Set 6<br/>(rear) (<math>\mu</math>s)</u> |
|-------|---|--|--|
| 0.525 | 227   | 239  | 254  |
| 0.600 | 249   | 262  | 277  |
| 0.675 | 269   | 285  | 301  |
| 0.750 | 294   | 310  | 322  |
| 0.850 | 322   | 340  | 355  |
| 0.950 | 354   | 376  | 382  |
| 1.050 | 388   | 407  | 417  |

79.4.131

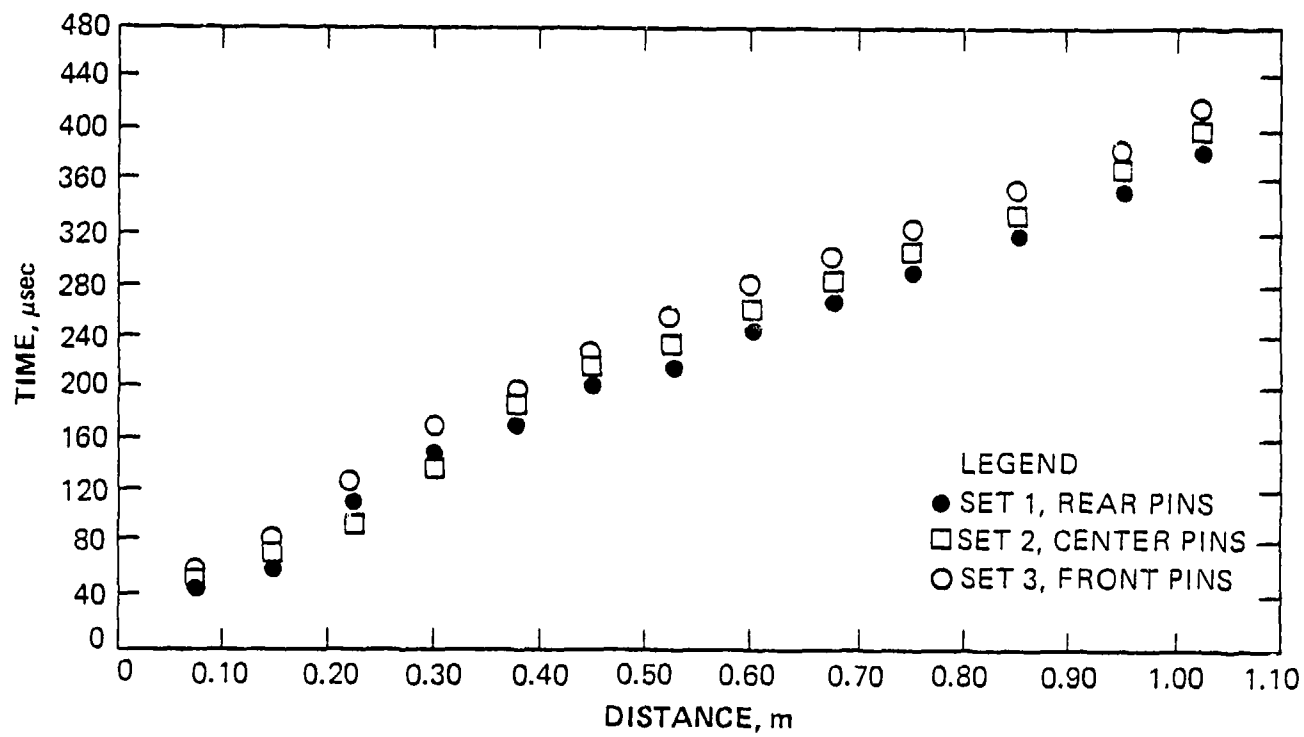


Figure 3-24 TOA versus range in thin ANFO Test 26.

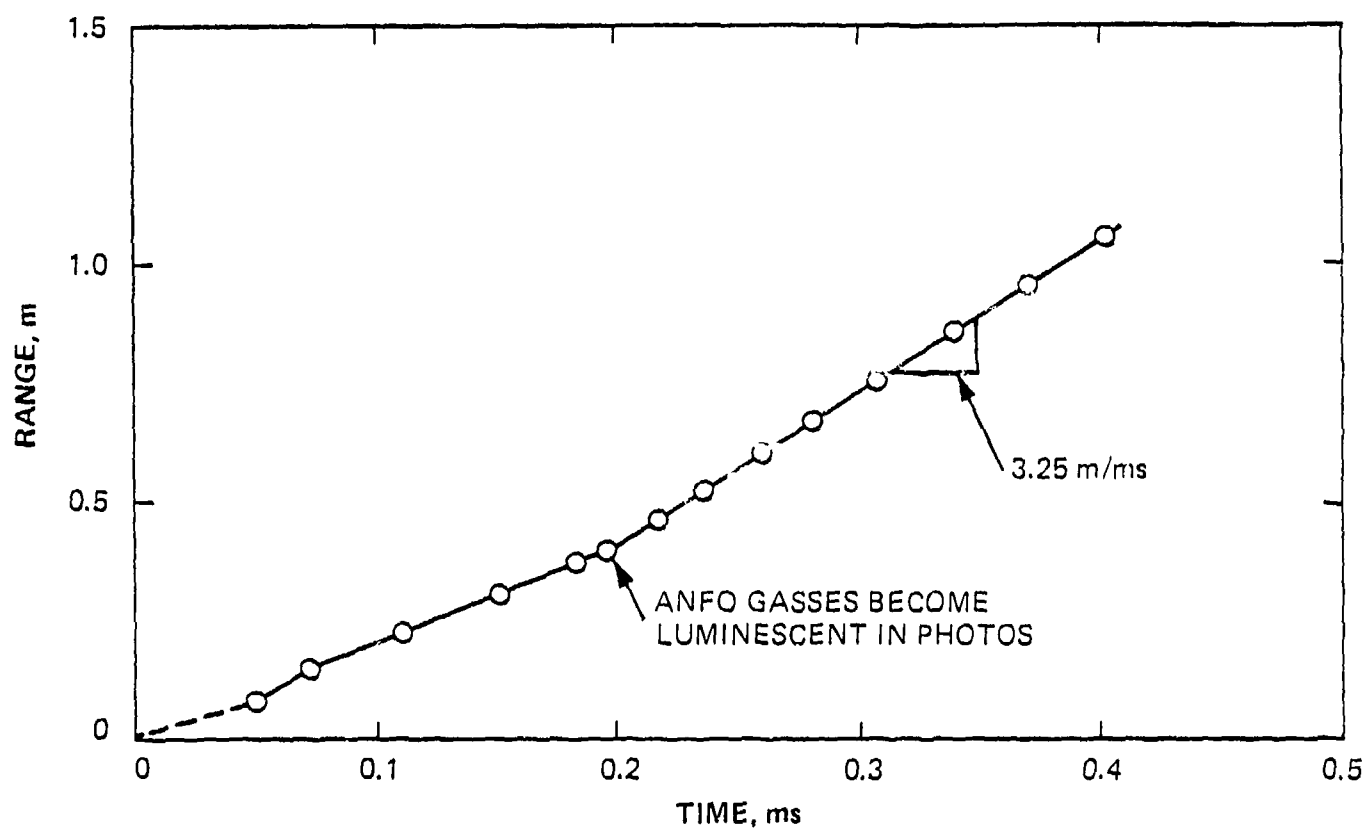


Figure 3-25 TOA in ANFO test 26 (average of three pin lines).

variable. After that time, the slope becomes remarkably regular, indicating a detonation velocity within the ANFO of about 3.25 m/ms (0.325 cm/ $\mu$ s). The point at which the change in slope occurs corresponds to the time when the ANFO gases become luminescent in the framing camera photographs. Figure 3-26 compares the averaged ANFO pin data with the data obtained from the photographs above and below the ANFO charge (lines 1 and 2). It is seen that the velocity data obtained from the photographs agree very well with the detonation velocity within the ANFO when account is taken of the time delay required for the ANFO detonation products to expand.

Figure 3-27 shows the data digitized from the framing camera along lines in 3 and 4, near and flush with the segmented aluminum plate, respectively. The two lines give data which are in good agreement, and from a range of 30 to approximately 80 cm the slope of the curve is constant, indicating a velocity of 0.375 cm/ $\mu$ s. Beyond the range of 80 cm, the velocity of the shock near the plate increases due to the formation of the Mach stem.

The above data agree well with the time-of-arrival data obtained from the TOA pins on and near the aluminum plate and from the pressure gages. These data are shown in Figure 3-28, and are summarized in tabular form in Table 3-6. Figure 3-28 compares these data with the digitized data from the camera time-of-arrival presented in Figure 3-27. Because of the positioning of the pressure gages, and the formation of the Mach stems, those gages experienced much higher pressures than expected. Therefore, no data concerning the peak pressure on the plate were obtained from Test 26.



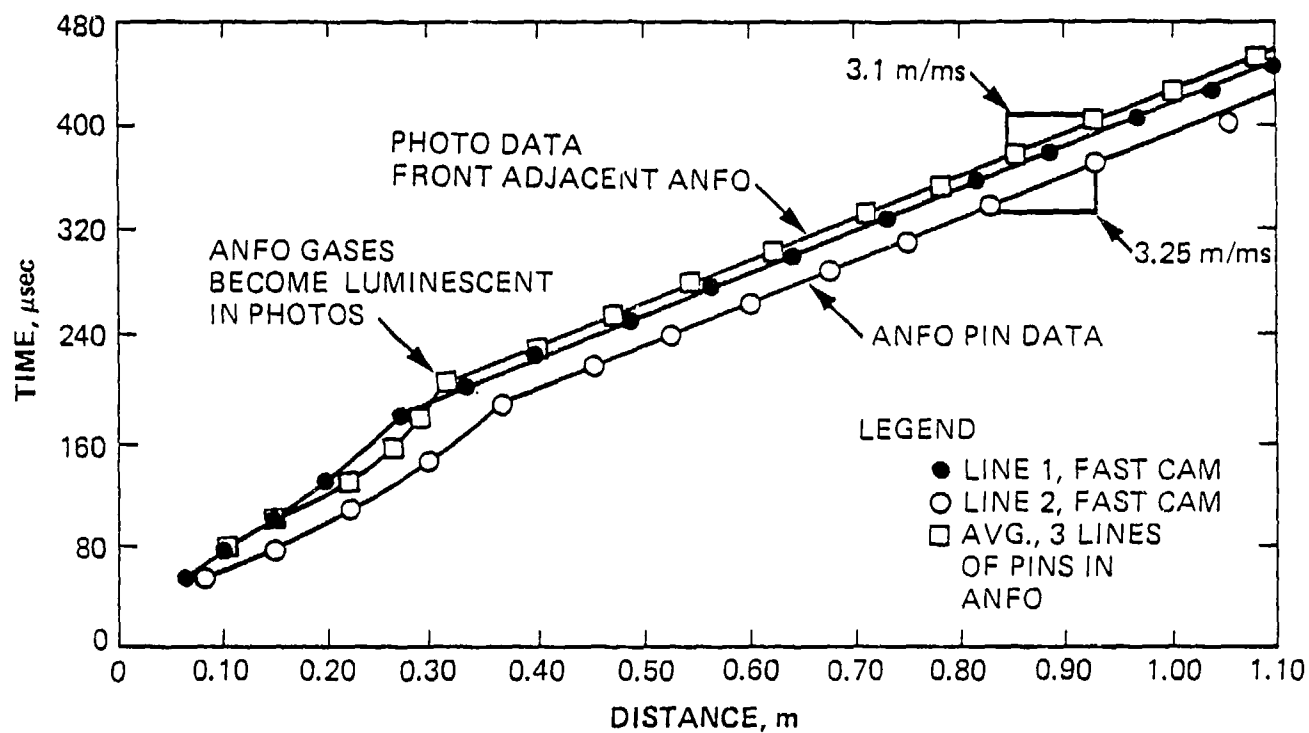


Figure 3-26 Comparison of average ANFO pin data in charge with data from framing camera photographs.

79-4-128

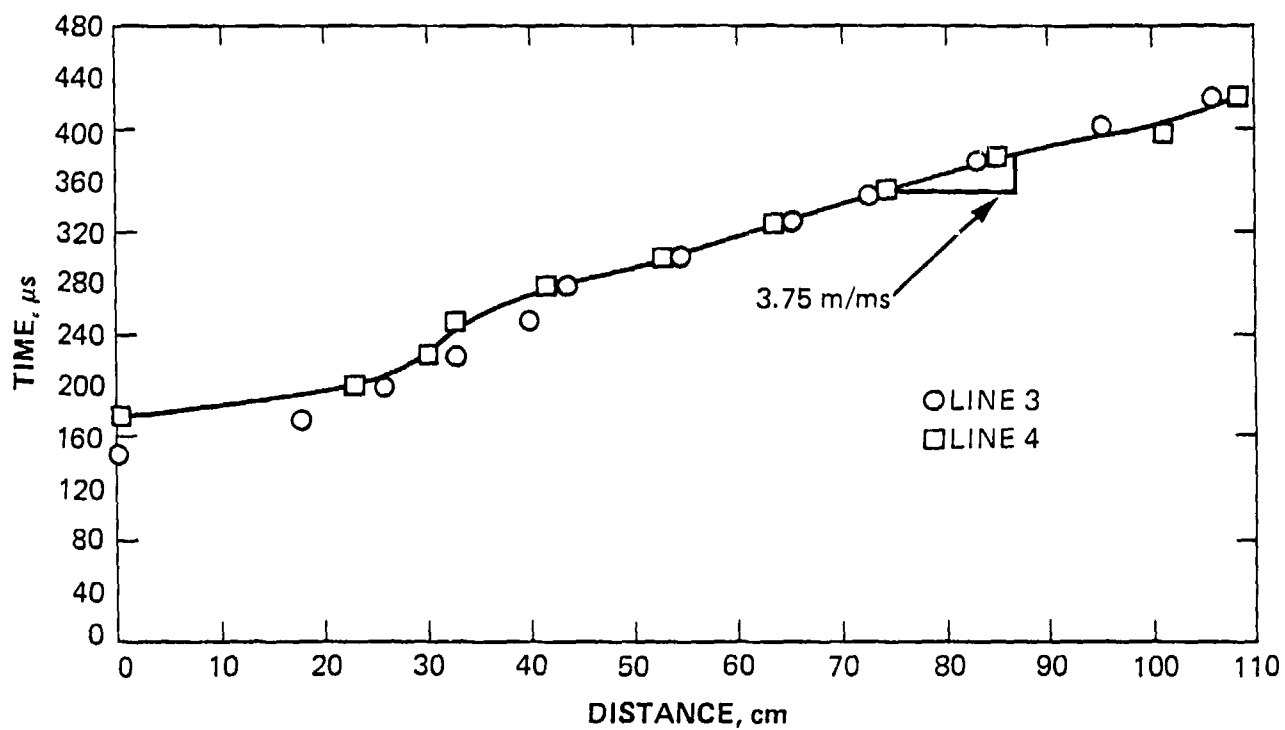


Figure 3-27 Data digitized from framing camera photos along lines 3 and 4, near the aluminum plate.

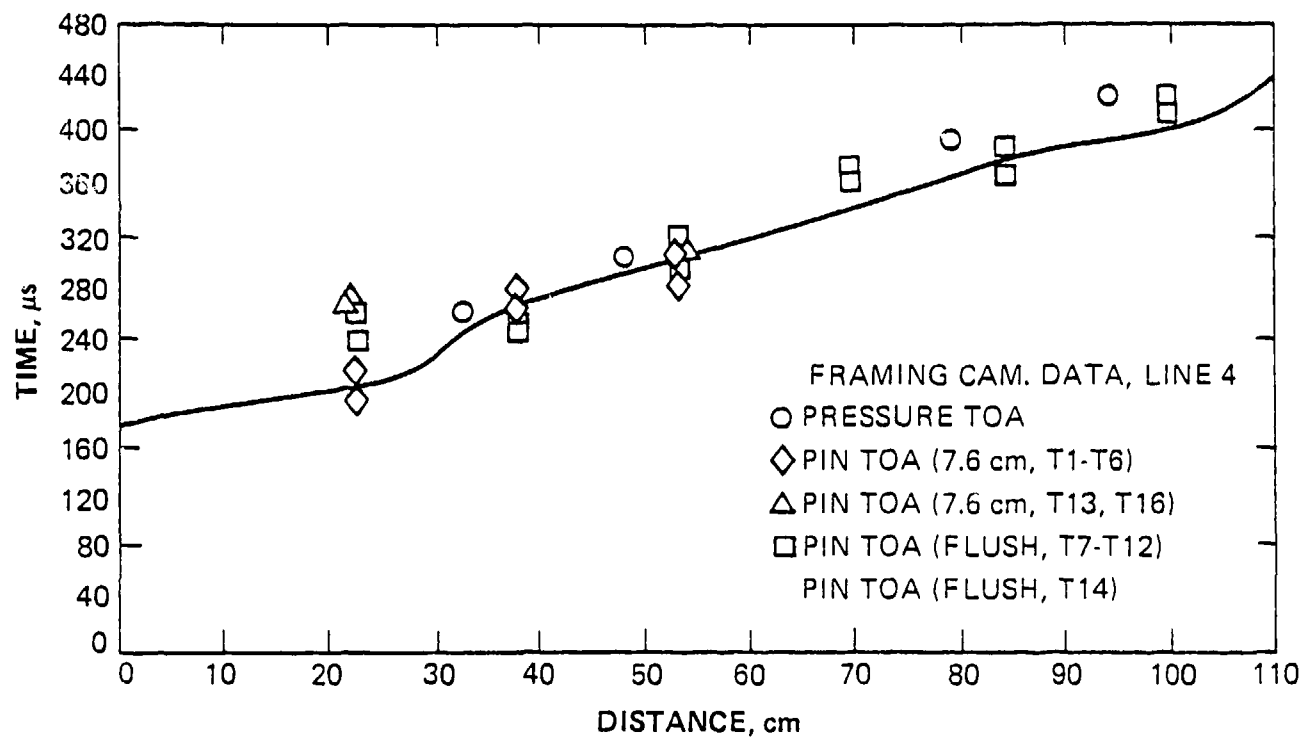


Figure 3-28 Comparison of gage and framing camera TOA data near the aluminum plate.

TABLE 3-6  
SUMMARY OF TOA MEASUREMENTS  
ON AND NEAR THE SEGMENTED ALUMINUM PLATE, TEST 26

| <u>PIN TOA DATA</u> |                              |                             |            |                              |                             |
|---------------------|------------------------------|-----------------------------|------------|------------------------------|-----------------------------|
| Range (cm)          | <u>Line 1</u>                |                             | Range (cm) | <u>Line 2</u>                |                             |
|                     | 7.6 cm Pin<br>TOA ( $\mu$ s) | Flush Pin<br>TOA ( $\mu$ s) |            | 7.6 cm Pin<br>TOA ( $\mu$ s) | Flush Pin<br>TOA ( $\mu$ s) |
| 23                  | T1, 200                      | T7, 240                     | 23.1       | T13, 262                     |                             |
| 38                  | T2, 260                      | T8, 241                     |            |                              |                             |
| 53.3                | T3, 291                      | T9, 298                     | 53.1       | T16, 305                     | T14, 294                    |
| 69.5                | T4, *                        | T10, 366                    |            |                              |                             |
| 84.7                | T5, *                        | T11, 370                    | 84.2       | T17, *                       | T15, *                      |
| 99.8                | T6, *                        | T12, 294                    |            |                              |                             |

PRESSURE GAGE TOA DATA

| <u>Gage</u> | <u>Range (cm)</u> | <u>TOA (<math>\mu</math>s)</u> |
|-------------|-------------------|--------------------------------|
| 1           | 33                | 253                            |
| 2           | 48                | 302                            |
| 3           | 79                | 393                            |
| 4           | 94                | 427                            |

\* No data obtained.

The formation of a Mach stem between the ANFO charge and the plate was suspected, based on the results of Test 25\* and some theoretical work performed previously by Leigh (Reference 10). Its formation has important implications concerning the design of the initiation system and detonator spacing for the STANDARD SOURCE charge. The data show that towards the end of the charge the detonation velocity in the ANFO for a thickness of 7.5 cm is slower than the velocity of the detonation products and the air shock in the region between the charge and the plate. This indicates that at some point the ANFO detonation products would begin to outrun the detonation wave in the ANFO, leading to the possibility that the ANFO charge would be destroyed before the detonation wave reaches the end of the charge. Obviously, the detonator spacing would have to be close enough to eliminate this possibility. Another result was that the detonation velocity in the ANFO charge itself was higher using the line detonation in Test 26 than had been measured previously using the point detonation (the early ANFO experiments), and that the charge design is not 1D but 2D.

### 3.3 INITIATION SYSTEM

The initiation design concept called for 4080 detonation points on 31 separate rings. This further required 31 separate times ranging from 4.8  $\mu$ s to 95  $\mu$ s between rings. It was possible to meet these requirements using electronic delay and 31 separate remote detonation units (see Figure 3-29). However, due

---

\*But timing uncertainties precluded any conclusions to be drawn from this test.

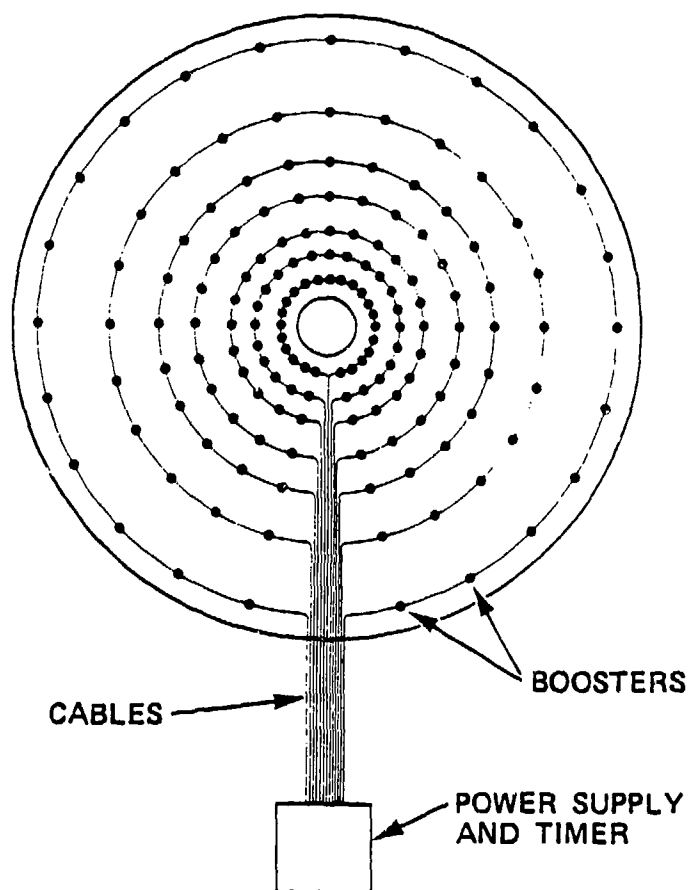


Figure 3-29 Concept of initiation geometry.

to the complication of sheer numbers, it was decided to design a simpler detonation system using a network of primacord and mild detonating fuse (MDF). It was felt that such a system would have the required accuracy and reliability and would offer several advantages such as being able to use one detonator for the entire shot. Such a system was designed for 4200 initiation points. It was required that accuracies for each point be within  $\pm 1 \mu s$  for the first 6 rings,  $\pm 1.5 \mu s$  for the next five rings, etc., up to a maximum of  $5 \mu s$  for the last few outer rings. The proposed system was designed around 400 grain Primacord and MDF with 5 grains HMX in an aluminum sheath. It was expected that the MDF would have the required accuracy and have no problem detonating the 400 grain Primacord rings. Suitable fittings were designed and fabricated for the Primacord-to-MDF junctions and the MDF-to-MDF junctions.

An experiment was performed at the Tracy Test Site to confirm the detonation across the Primacord-to-MDF junctions and the MDF-to-MDF junctions. The experiment (shown in Figure 3-30) used 4.6 m of 400 grain Primacord between the detonator and the first junctions. Typical junctions and links of primacord and MDF were used as shown. Ionization pins were used at the numbers 1 through 6 to determine time-of-arrival. The results of these experiments are summarized in Table 3-7. As can be seen from these tests, this initiator design meets all the requirements known at this time.

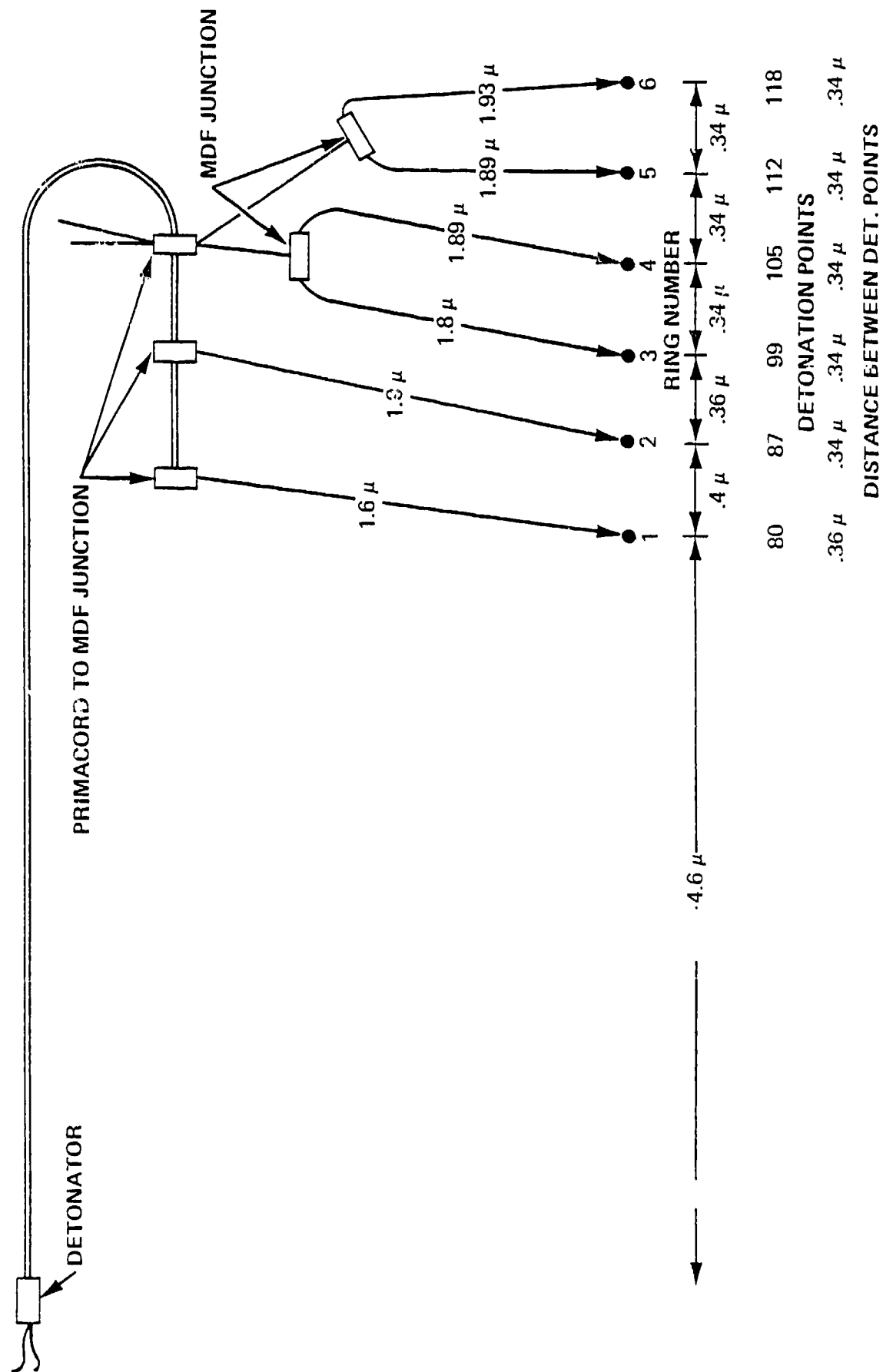


Figure 3-30 Initiation system test layout.



TABLE 3-7  
DATA SUMMARY INITIATION SYSTEM TESTS

| <u>RING NUMBER</u> | <u>CALCULATED<br/>ARRIVAL TIME<br/>(<math>\mu</math>s)</u> | <u>MEASURED ARRIVAL TIME (<math>\mu</math>s)</u> |               |               |
|--------------------|--|--|---------------|---------------|
|                    |  | <u>Test 1</u>                                    | <u>Test 2</u> | <u>Test 3</u> |
| 1                  | 0  | 0  | 0             | 0             |
| 2                  | 4.8  | 4.6  | 4.8           | 4.7           |
| 3                  | 10.0   | 7.3  | -             | 7.9           |
| 4                  | 20.0   | 17.8   | 17.3          | 17.5          |
| 5                  | 23.6   | 21.2   | 22.6          | 22.6          |
| 6                  | 29.0   | 25.0   | 24.7          | 24.7          |

### 3.4 LOW OVERPRESSURE AIRBLAST CHARACTERISTICS

Three experiments were performed to determine the low overpressure airblast produced by a charge shaped like the standard source surface charge. This charge was designed to produce the correct airblast-induced ground motions. To produce a time simulation of the surface airblast from a 1-kiloton nuclear surface burst, particularly in the overpressure range of 60 to 680 kPa (10 to 100 psi), a 500-ton spherical TNT charge is required. The designed surface charge consisted of only 103 tons of HE, but the shape of the charge (roughly that of a thin disc) might provide some enhancement of the surface airblast. It was concluded that to determine the airblast characteristics of this charge, a small-scale experiment was required. Therefore, a small airblast pad was constructed at the Tracy Test Site and an airblast line was installed in it. This section describes the three tests (Tests 18, 19, and 20 of Table 3-1). Two of these used a spherical HE charge (Tests 18 and 20) intended to normalize the airblast; the other (Test 19) used a scale model standard source charge constructed with thin layers of sheet explosive.

A 45.5 kg (100 lb) spherical TNT charge was available for the airblast normalization experiment, so the model standard source charge was designed with that in mind. To keep the same total charge ratio between current large-scale HE detonation

(500-ton spheres or cylinders) and the designed standard source surface charge (~100 tons), a total model charge explosive weight of 9 to 11 kg (20 to 25 lbs) was required. Calculated scaled charge dimensions are shown in Table 3-9. The model charge sheet had a maximum thickness of 0.44 cm for ranges up to 0.214 m, and a minimum thickness of 0.17 cm at a range of 0.928 m. This design was then meshed with the particular sheet explosive selected for the experiment, Dupont EL506 C-1, which is produced in a sheet thickness of 0.107 cm. It was found that a good approximation of the scaled charge could be obtained by stacking layers of circular sheet explosive sections (see Figure 3-31) as summarized in Table 3-8. The calculated weight of the charge was 10.5 kg (23 lbs). The scaled height of the model charge was small enough to permit placing the charge directly on the ground. Likewise, the charge timing was scaled and a series of detonation rings designed to allow the model charge to be detonated sequentially (as would be the case with the full size surface charge). There were 238 detonation points located in 6 circular rings with relative firing times ranging from 0  $\mu$ s (close in) to 36.28  $\mu$ s (edge of the charge). Strips of EL506 C-1 explosive were used as initiators. Figure 3-32 shows a photograph of the model charge (Test 19).

Test 18 employed a 10.5 kg (23 lb) cylindrical nitromethane charge and was intended primarily for system checkout and airblast gage calibration. Test 20 was the 45.5 kg (100 lb) sphere of TNT. Due to a recording error on Test 20, no data were obtained, and Test 18 was subsequently used for further normalization and comparison with the scaled model charge (Test 19).

TABLE 3-8  
 DIMENSIONS AND DESIGN OF THE  
 SCALE MODEL STANDARD SOURCE SURFACE CHARGE (TEST 19)

| Range, m | Charge Thickness |       | Number of           |                  |
|----------|------------------|-------|---------------------|------------------|
|          | cm               | in    | Layers of EL506 C-1 | Sheet Explosive* |
| 0.214    | 0.44             | 0.173 | 4.12                | 4                |
| 0.232    | 0.42             | 0.165 | 3.93                |                  |
| 0.278    | 0.39             | 0.154 | 3.67                |                  |
| 0.325    | 0.36             | 0.142 | 3.38                |                  |
| 0.371    | 0.34             | 0.134 | 3.19                | 3                |
| 0.418    | 0.32             | 0.126 | 3.00                |                  |
| 0.464    | 0.30             | 0.118 | 2.81                |                  |
| 0.511    | 0.28             | 0.110 | 2.62                |                  |
| 0.557    | 0.27             | 0.106 | 2.52                | 2                |
| 0.603    | 0.25             | 0.098 | 2.33                |                  |
| 0.650    | 0.23             | 0.090 | 2.14                |                  |
| 0.696    | 0.22             | 0.087 | 2.07                |                  |
| 0.743    | 0.21             | 0.083 | 1.98                | 2                |
| 0.789    | 0.20             | 0.079 | 1.88                |                  |
| 0.835    | 0.19             | 0.075 | 1.79                |                  |
| 0.882    | 0.18             | 0.071 | 1.69                |                  |
| 0.928    | 0.17             | 0.067 | 1.60                |                  |

\*Sheet thickness of 0.107 cm (0.042 inch).

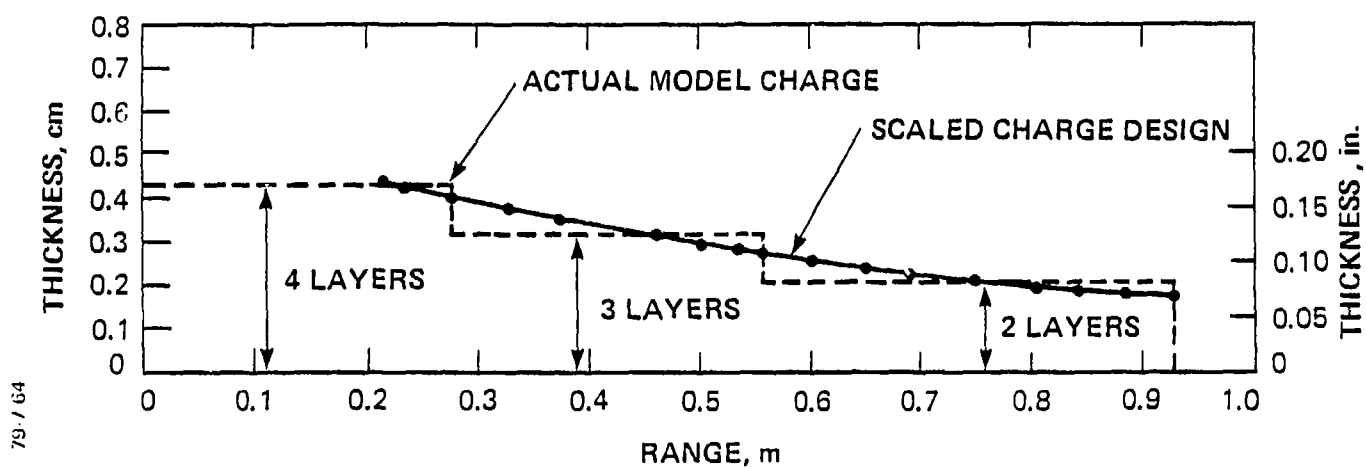


Figure 3-31 Design of model standard source surface charge using layers of EL506C-1 sheet explosive.



Figure 3-32 Model standard source charge, Test 19.

The airblast line consisted of six airblast measurement stations. Their ranges and the predicted overpressures are given in Tables 3-9 and 3-10 for tests 18 and 19, and 20, respectively. Two types of high resolution PCB\* airblast gages were used; Type 102-A02 (0-0.7 MPa [0-100 psi] overpressure range) and Type 102-A12 (0-1.7 MPa [0-250 psi] overpressure range).

Results for Tests 18 and 19 are presented in Tables 3-11 and 3-12, respectively; the peak overpressures for both the 10.5 kg nitromethane charge (Test 18) and the model standard source charge (Test 19) are plotted in Figure 3-33. No data were recorded on Test 20 (the 45.5 kg TNT sphere); however, a prediction curve is given in Figure 3-33. The measured peak overpressures from the 10.5 kg nitromethane charge agreed well with the prediction. The measured peak overpressures from the model standard source charge are higher than the nitromethane charge data for ranges less than 5 m. At ranges greater than 5 m, they appear to be consistent with the 10.5 kg spherical charge data which indicate no air blast enhancement.

The pressure gage records were digitized and these data integrated to obtain the total positive phase impulse (Tables 3-11 and 3-12). These data are plotted in Figure 3-34 for the two charges. Although the data spread is large, it is felt that it is sufficient to determine that no significant enhancement of positive phase impulse occurs at any range. All digitized overpressure records and associated impulse curves are

---

\*Manufactured by PCB Piezotronics, Inc., Buffalo, N.Y.

TABLE 3-9  
EXPERIMENT PLAN FOR TESTS 18 AND 19

| Range<br>m | ft | Gage Range |      | Expected Peak* |     | Set Range |      |           |     |
|------------|----|------------|------|----------------|-----|-----------|------|-----------|-----|
|            |    | MPa        | psi  | MPa            | psi | Primary   |      | Secondary |     |
| 1.83       | 6  | 13.6       | 2000 | 2.7            | 400 | 6.8       | 1000 | 2.7       | 400 |
| 3.66       | 12 | 1.36       | 200  | 0.6            | 90  | 1.36      | 200  | 0.7       | 100 |
| 4.57       | 15 | 1.36       | 200  | 0.33           | 48  | 1.36      | 200  | 0.54      | 80  |
| 5.49       | 18 | 1.36       | 200  | 0.20           | 30  | 0.68      | 100  | 0.34      | 50  |
| 8.53       | 28 | 0.14       | 20   | 0.075          | 11  | 0.14      | 20   | 0.07      | 10  |
| 13.11      | 43 | 0.14       | 20   | ~0.041         | ~6  | 0.14      | 20   | 0.07      | 10  |

\*Based on 10.5 kg tangent sphere of TNT.



TABLE 3-10  
EXPERIMENT PLAN FOR TEST 20

| Range | Gage Range |    | Expected Peak* |      | Set Range |     |                |                  |      |     |
|-------|------------|----|----------------|------|-----------|-----|----------------|------------------|------|-----|
|       | m          | ft | MPa            | psi  | MPa       | psi | Primary<br>MPa | Secondary<br>psi |      |     |
| 3.96  | 13         |    | 13.6           | 2000 | 2.0       | 300 | 6.8            | 1000             | 2.7  | 400 |
| 5.79  | 19         |    | 1.36           | 200  | 0.7       | 100 | 1.36           | 200              | 0.7  | 100 |
| 6.71  | 22         |    | 1.36           | 200  | 0.44      | 64  | 1.36           | 200              | 0.54 | 80  |
| 7.62  | 25         |    | 1.36           | 200  | 0.30      | 44  | 0.68           | 100              | 0.34 | 50  |
| 10.67 | 35         |    | 1.36           | 200  | 0.12      | 18  | 0.27           | 40               | 0.14 | 20  |
| 15.24 | 50         |    | 0.14           | 20   | 0.06      | 9.5 | 0.14           | 20               | 0.07 | 10  |

\*Based on 45.5 kg tangent sphere of TNT.

TABLE 3-11

SUMMARY RESULTS FOR  
10.5 kg NITROMETHANE CHARGE (TEST 18)

| Range<br>m | ft | Peak Overpressure |     |          |       | Total Impulse, I <sup>+</sup> |        |          |        |
|------------|----|-------------------|-----|----------|-------|-------------------------------|--------|----------|--------|
|            |    | Expected          |     | Measured |       | Expected                      |        | Measured |        |
|            |    | kPa               | psi | kPa      | psi   | kPa-ms                        | psi-ms | kPa-ms   | ms-psi |
| 1.83       | 6  | 2720              | 400 | 1709     | 263.2 |                               |        | 904      | 133    |
| 3.66       | 12 | 612               | 90  | 700      | 103.0 | 380                           | 55.9   | 476      | 70     |
| 4.57       | 15 | 326               | 48  | 411      | 60.5  | 280                           | 41.2   | 360      | 52.9   |
| 5.49       | 18 | 204               | 30  | 291      | 42.8  | 245                           | 36.0   | 358      | 52.7   |
| 8.53       | 28 | 75                | 11  | 62.6     | 9.2   | 160                           | 23.5   | 131      | 19.3   |
| 13.10      | 43 | 41                | 6   | 51.0     | 7.5   | 109                           | 16.0   | 226      | 33.2   |

TABLE 3-12  
SUMMARY RESULTS FOR  
10.5 kg MODEL CHARGE (TEST 19)

| Range<br><u>m</u> | <u>(ft)</u> | Peak Overpressure |            | Total Impulse, I <sup>+</sup> |               |
|-------------------|-------------|-------------------|------------|-------------------------------|---------------|
|                   |             | <u>kPa</u>        | <u>psi</u> | <u>kPa-ms</u>                 | <u>psi-ms</u> |
| 1.83              | 6           | 4223              | 621        | 447                           | 65.7          |
| 3.66              | 12          | 1197              | 176        | 411                           | 60.5          |
| 4.57              | 15          | 560-583           | 82.3-85.8  | 204-249                       | 30.0-36.6     |
| 5.49              | 18          | 233               | 34.3       | 219                           | 32.2          |
| 8.53              | 28          | 86.4              | 12.7       | 133                           | 19.5          |
| 13.10             | 43          | 34.0              | 5.0        | 81.6                          | 12.0          |

79-7-36

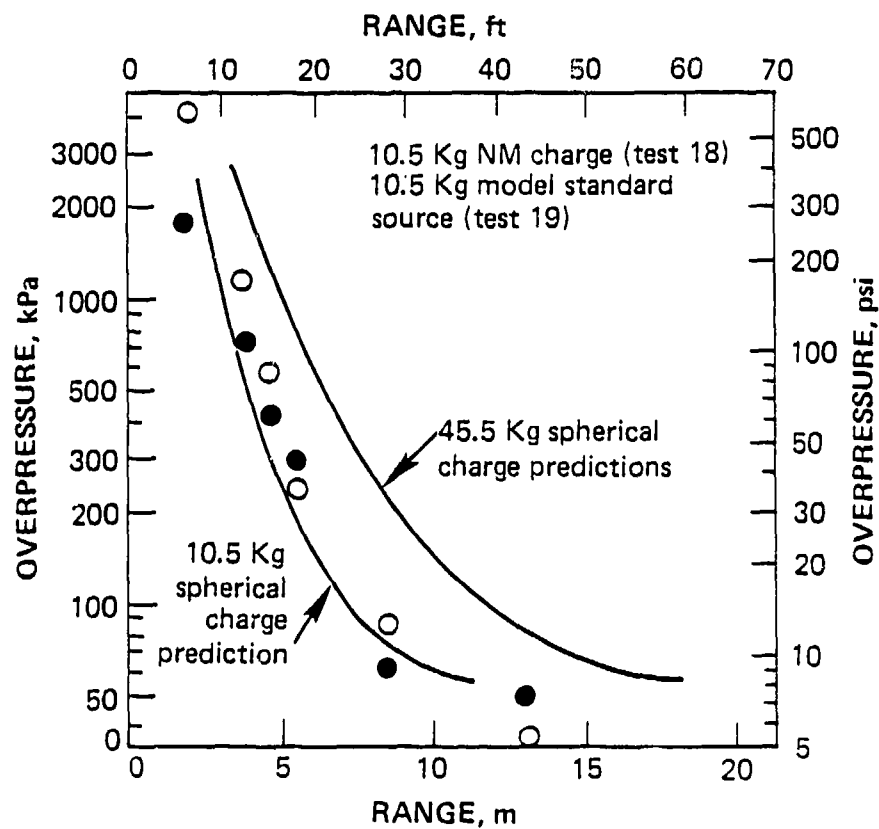


Figure 3-33 Comparison of Test 18 and Test 19 measured peak overpressures with predictions.

79-7-38

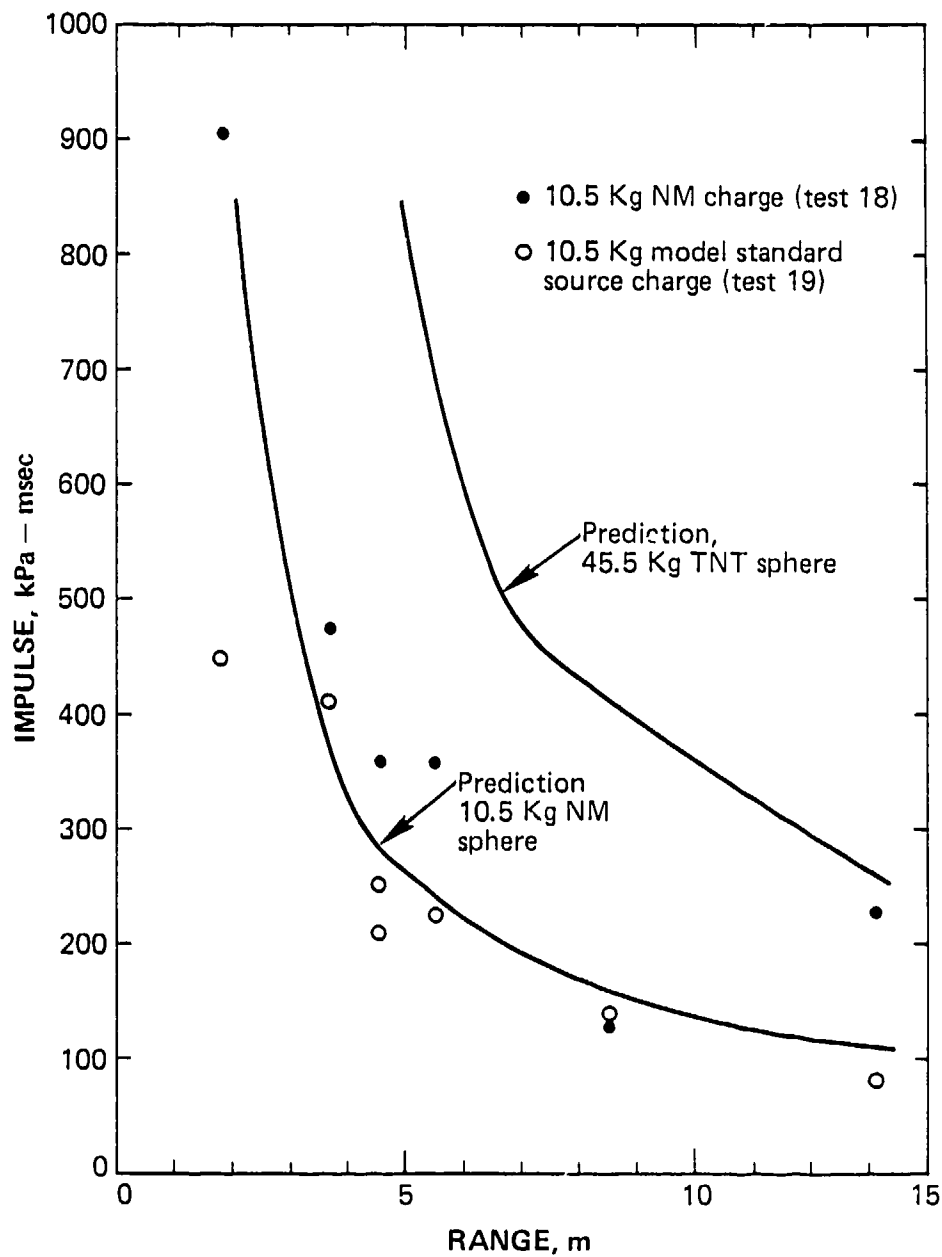


Figure 3-34 Comparison of expected and measured positive phase impulse ( $I^+$ ), Tests 18 and 19.

presented in the Appendix.

In summary, the small scale experiments examining the low overpressure behavior of the standard source charge show that some enhancement of peak overpressure occurs at ranges close to the charge, but for peak overpressures lower than 200 kPa (30 psi), the standard source charge at best "looks like" an equal-weight spherical HE detonation. Thus, more HE must be added to the standard source charge to produce the airblast from a 1 kt nuclear detonation in the low overpressure range (68 to 680 kPa [10 to 100 psi]).

## SECTION 4

### A SIMULATION OF DIRECTLY COUPLED ENERGY FROM A NUCLEAR EVENT

#### 4.1 TWO-DIMENSIONAL CALCULATION OF JANGLE S

The specific objectives of the JANGLE S calculation, following those used in the Mine Throw I design effort (Reference 1), are listed below:

1. Calculate the total fraction of the nuclear source energy coupled to the alluvium.
2. Calculate the two-dimensional contour in the alluvium corresponding to a peak pressure of 7.2 GPa (72 kbar) and the arrival time of the shock front at this contour.
3. Calculate the total impulse delivered across the above contour.

The above information from the nuclear calculation is sufficient to design the ANFO charge required to simulate the cratering and direct-induced ground motion, a necessary part of the total STANDARD SOURCE simulation. To obtain this information it is necessary only to investigate the coupling process during its early formative stages, i.e., the first 1 or 2 ms. Therefore, the calculation was not carried to late times and the processes associated with late stage crater development were not investigated as part of this effort.

4.1.1 Zoning and Initial Conditions. PISCES 2DELK is a coupled Euler-Lagrange two-dimensional continuum mechanics

computer code. This is extremely advantageous for surface-burst cratering calculations for two reasons. First, Euler differencing (where the zone size remains fixed in time, but the mass of each zone varies with time) can be used in the region close to and including the explosive source, where violent, turbulent motions associated with shock vaporization or detonation predominate. Second, Lagrange differencing (where the mass of each zone remains constant but the zone shape can change) can be used for other regions, enabling one to accurately monitor pressure and velocity waveforms at specified positions within the grid. Euler and Lagrange regions can be coupled across mutual interfaces, allowing transmission of shock waves from one region to the other.

The coupled Euler-Lagrange option in 2DELK was used effectively in the JANGLE 3 calculation. Figure 4-1 shows the initial geometry and Euler zoning. The grid extended to a range of 1.5 to 4.5 meters above the ground surface and 0.7 meter below the ground surface. The calculation was conducted in cylindrical symmetry, with the axis of symmetry located at  $R = 0.0$  m. The nuclear source was modeled as a sphere with an initial radius of 0.690 meter centered on the axis at a distance of 1.0670 meter above the ground surface. This geometry is consistent with the actual nuclear device geometry. The initial Euler zoning in the vicinity of the nuclear source and the alluvium was 50 mm (4R) by 52.5 mm (4Z). Beginning at a distance of 2.135 m above the ground surface, the zoning in the Z-direction was geometrically increased by a ratio of 1.045:1. The total number of zones in the R direction, initially, was 50, and in the Z-direction, 78.



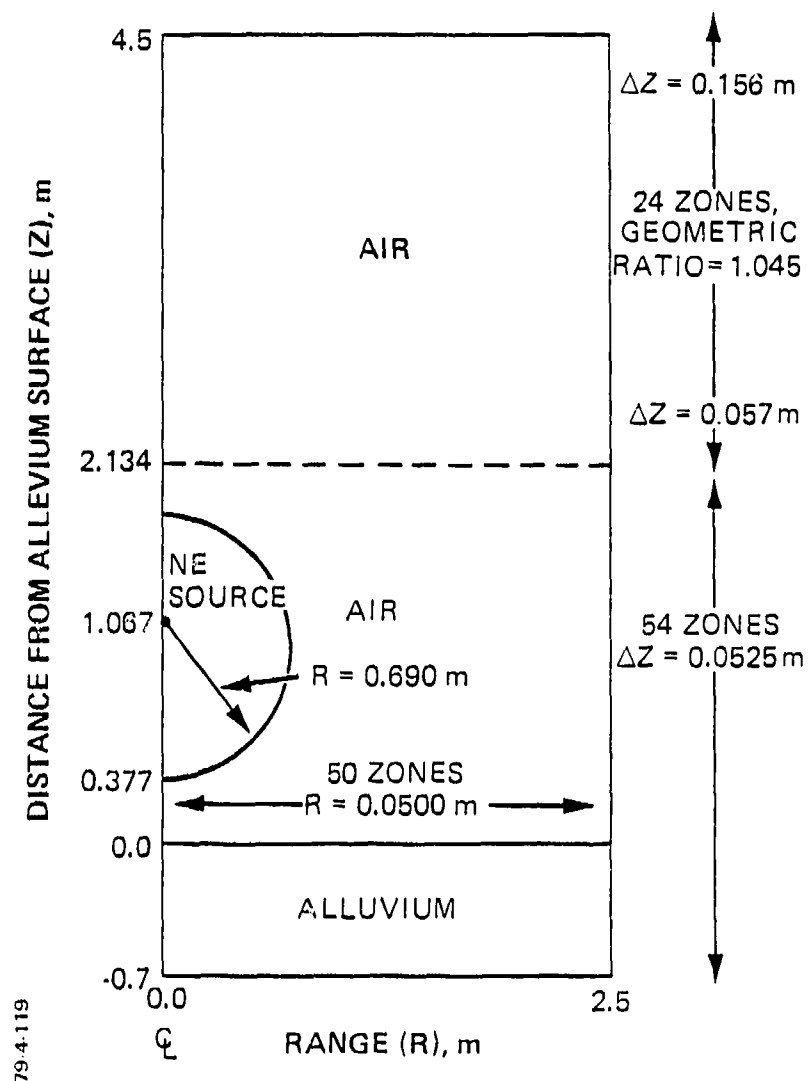


Figure 4-1 Initial geometry and Euler zoning for JANGLE S 2DELK calculation.

The spherical nuclear source was assumed to have a uniform initial density (2.16834 g/cc) and internal energy ( $1.6806 \times 10^{13}$  ergs/gm), but no initial velocities. Initial conditions for the nuclear source, air, and alluvium are summarized in Table 4-1.

As the calculation progressed, the size of the Euler grid was increased in order to follow the shock wave in the air close to the ground surface and in the underlying alluvium. To aid in this rezone effort, two one-dimensional calculations were performed to conservatively estimate shock arrival times.

The first calculation contained only the nuclear source surrounded by a large void region. Its purpose was to obtain the rate of free expansion of the nuclear source. The initial conditions for the nuclear source were the same as for the two-dimensional calculation. A gamma-law equation of state (EOS) was used (constant  $\gamma = 1.5$ ). This will be discussed in more detail in Section 4.3. The result of this calculation was that at about 10  $\mu$ s, the nuclear source debris reached a limiting velocity of about 9 cm/ $\mu$ s. The second calculation, also performed in spherical symmetry, placed alluvium beyond the void region at a range of 1.067 meter. The purpose of this calculation was to obtain a conservative estimate of the shock arrival time and peak shock pressure in the alluvium directly beneath the nuclear source. The nuclear source was again treated as a gamma-law gas; the alluvium EOS model was the same as used in the two-dimensional calculation. It will be discussed in Section 4.3. A result of this calculation is summarized in Figure 4-2, which plots the calculated arrival time of the peak pressure in the ground.

TABLE 4-1

## INITIAL CONDITIONS FOR MATERIALS IN JANGLE S CALCULATION

| <u>MATERIAL</u>   | <u>INITIAL<br/>DENSITY</u>                 | <u>INITIAL<br/>INTERNAL ENERGY</u> | <u>INITIAL<br/>VELOCITY</u> |
|-------------------|--|------------------------------------|-----------------------------|
| Nuclear<br>Source | 2.16834 Mg/m <sup>3</sup>                  | 15.806 eu*/g                       | 0.0 cm/us                   |
| Air               | 1.293 x 10 <sup>-3</sup> Mg/m <sup>3</sup> | 0.002 eu/g                         | 0.0 cm/us                   |
| Alluvium          | 2.13 Mg/m <sup>3</sup>                     | 0.0 eu/g                           | 0.0 cm/us                   |

\*1 eu/g = 10<sup>12</sup> ergs/gm

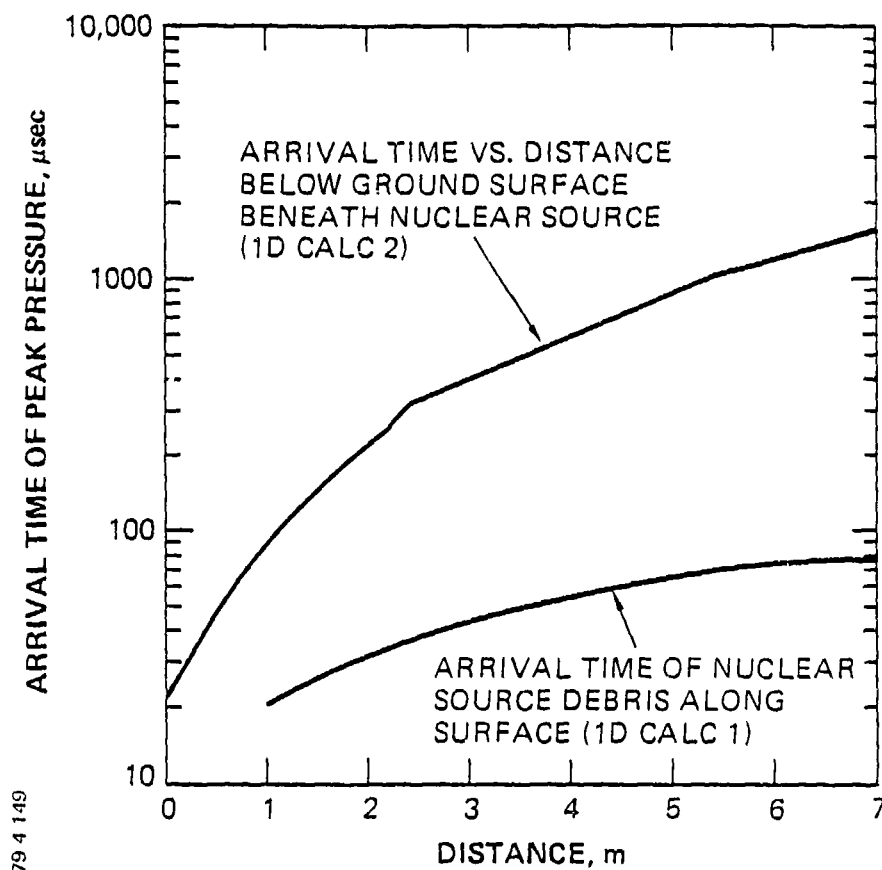


Figure 4-2 Shock arrival time in the vicinity of the JANGLE S nuclear source, based on one-dimensional calculations.

Also plotted in this figure is the arrival time of the nuclear source debris close to the surface as obtained from the first one-dimensional calculation. It is easily seen that the expansion of the debris is much more rapid than the propagation of the direct-induced shock into the alluvium. For example, the debris arrives at a point 2 meters from the center of the source at a time of about 30  $\mu$ s, whereas the shock wave reaches a point 2 meters below the ground surface directly below the device in about 220  $\mu$ s.

Figure 4-2 aided considerably in design the rezone schedule for the Euler grid. This schedule is shown in Table 4-2. It can be seen from this table and Figure 4-2 that Euler rezones were performed before the shock reached the edge of the grid during the first 0.6 ms of the calculation. When coupling from the airblast and source debris predominate. The extent of the grid above the ground surface was held constant at 4.5 meters, so that after about 0.6 ms, energy was allowed to escape through this boundary.

Below the ground surface, a Lagrange grid was dimensioned to monitor the shock wave for peak shock pressures of less than or equal to 7.2 GPa (72 kbar) and to monitor the total impulse delivered to the alluvium beyond the 7.2 GPa peak pressure contour. As shown in Figure 4-3, the Lagrange grid was a hemispherical shell lying below the ground surface with an initial inner radius of 2.0 meters and an outer radius of 5.0 meters. There were 21 zones in the circumferential ( $\theta$ ) direction and 15 zones in the radial direction. In the circumferential direction, the zone size was a constant 0.20 meter; in the radial direction,

TABLE 4-2  
SUMMARY OF EULER REZONES PERFORMED IN THE 2DELK JANGLE S CALCULATION

| Time           | Extent of Grid   |                  | approximate zone size<br>in source region<br>( $\Delta R \times \Delta Z$ ) |       | Total number<br>of zones |              |
|----------------|------------------|------------------|---|-------|--------------------------|--------------|
|                | above<br>surface | below<br>surface |   |       | # $\Delta R$             | # $\Delta Z$ |
| 0 - .023 ms    | 4.5 m            | 0.7 m            | 0.5 m x   | .05 m | 78                       | 50           |
| .023 - .067 ms | 4.5 m            | 2.8 m            | .10 m x   | .10 m | 61                       | 50           |
| .067 - .796 ms | 4.5 m            | 2.8 m            | .15 m x   | .10 m | 61                       | 50           |
| .796 - 2.0 ms  | 4.5 m            | 4.0 m            | .15 m x   | .10 m | 73                       | 50           |

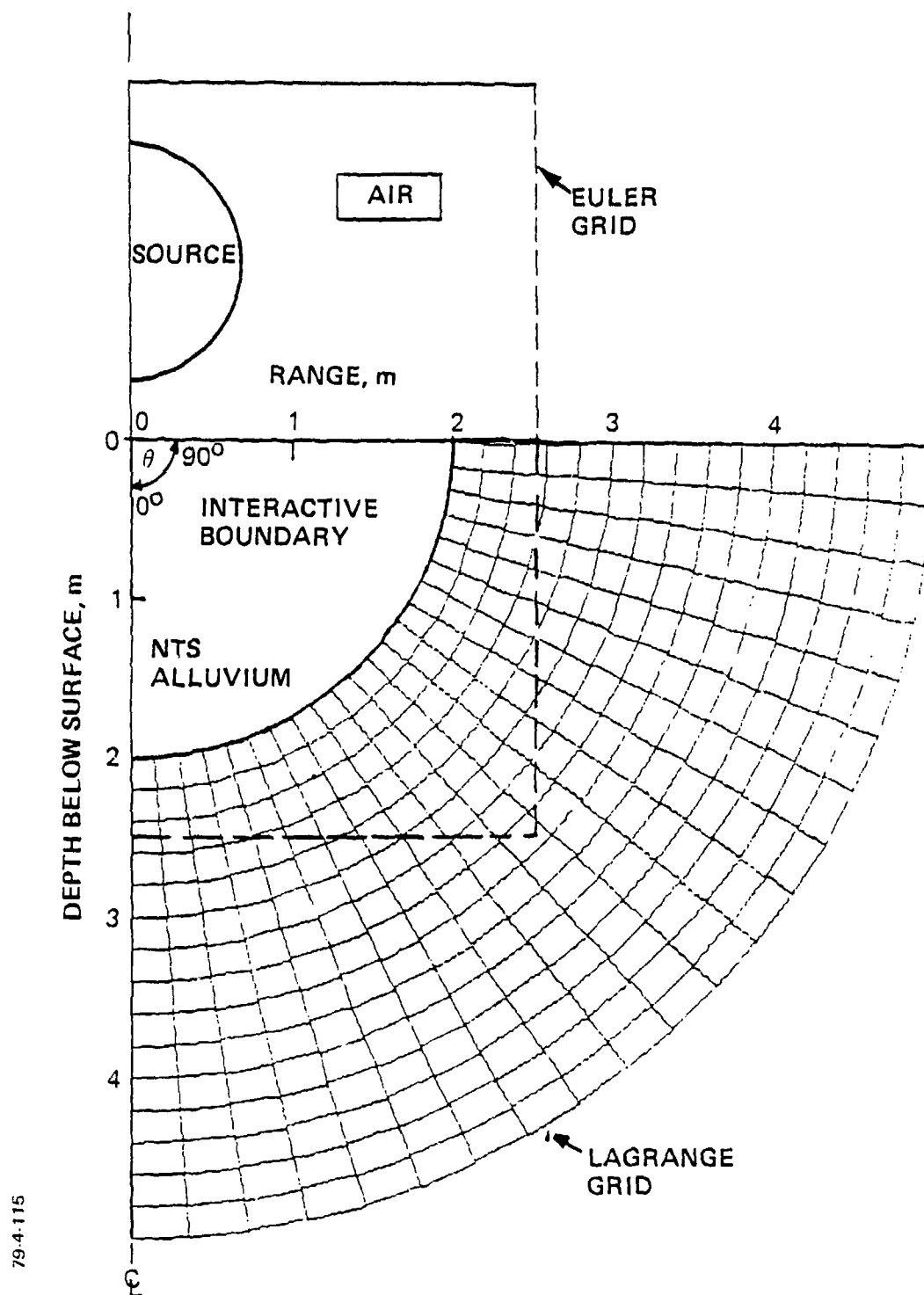


Figure 4-3 Initial coupled Lagrange/Euler grid for the JANGLE S 2DELK calculation.

the zone size varied from about 0.15 meter at  $R = 2.0$  meters to about 0.4 meter at  $R = 5.0$  meters. Also shown in Figure 4-3 is a sketch of the Euler grid discussed previously. The interactive boundary defined between the Euler and Lagrange regions is also indicated. The number of radial Lagrange zones was increased and the size of the grid expanded as the calculation progressed. The maximum number of radial Lagrange zones was 33, and the maximum radial extent of the grid was 10 meters.

4.1.2 Equations of State. To perform the JANGLE S calculation, equations of state for the nuclear source material, air, and NTS alluvium are required. This section describes the equations of state for each of these materials.

Briefly summarizing, the alluvium model used was the CIST15 model developed at the Air Force Weapons Laboratory (References 11 and 12) to characterize layered alluviums found at the White Sands Missile Range. The nuclear source was described by the ideal gas EOS with a constant gamma. The air was also described as an ideal gas, but with variable gamma. Because all three materials exist in the Euler grid, and only two materials per cell are currently allowed, both the air and the source were designated to be the same material in the computational description and a criterion based on the cell material density was devised to differentiate between the two.

NTS Alluvium EOS. The AFWL CIST (Cylindrical In-situ Test) soil model was programmed for 2DELK in order to describe the NTS alluvium. It calculates pressure as a function of  $\mu$  (compression) and, optionally, as a function of  $e$  (specific



internal energy). The pressure is the sum of two components: a hydrostatic component which depends only on  $\mu$ , and an energy dependent term. The hydrostatic component,  $p_H$ , is calculated directly using a piecewise continuous fit to experimental data. The hydrostatic loading/unloading curves are history-dependent. The energy-dependent pressure term is a standard, condensed phase Tillotson form equation-of-state (Reference 13). The general form of the pressure equation is:

$$p = p_H + Goe + \left[ \frac{T}{\frac{e}{e_o \eta^2} + 1} \right] oe,$$

- $p$   $\equiv$  total pressure
- $p_H$   $\equiv$  hydrostatic pressure
- $G$   $\equiv$  Gruneisen coefficient
- $T$   $\equiv$  Tillotson Coefficient
- $e_o$   $\equiv$  constant
- $\eta$   $\equiv$   $\mu + 1 \equiv \rho/\rho_o$
- $e$   $\equiv$  specific internal energy
- $\rho$   $\equiv$  mass density

The hydrostatic pressure versus compressibility equations comprise a four interval, piecewise, continuous function. Figure 4-4 shows a generalized plot of the hydrostatic pressure,  $p_H$ , versus compression,  $\mu$ . The equations are listed below:

79 4 137

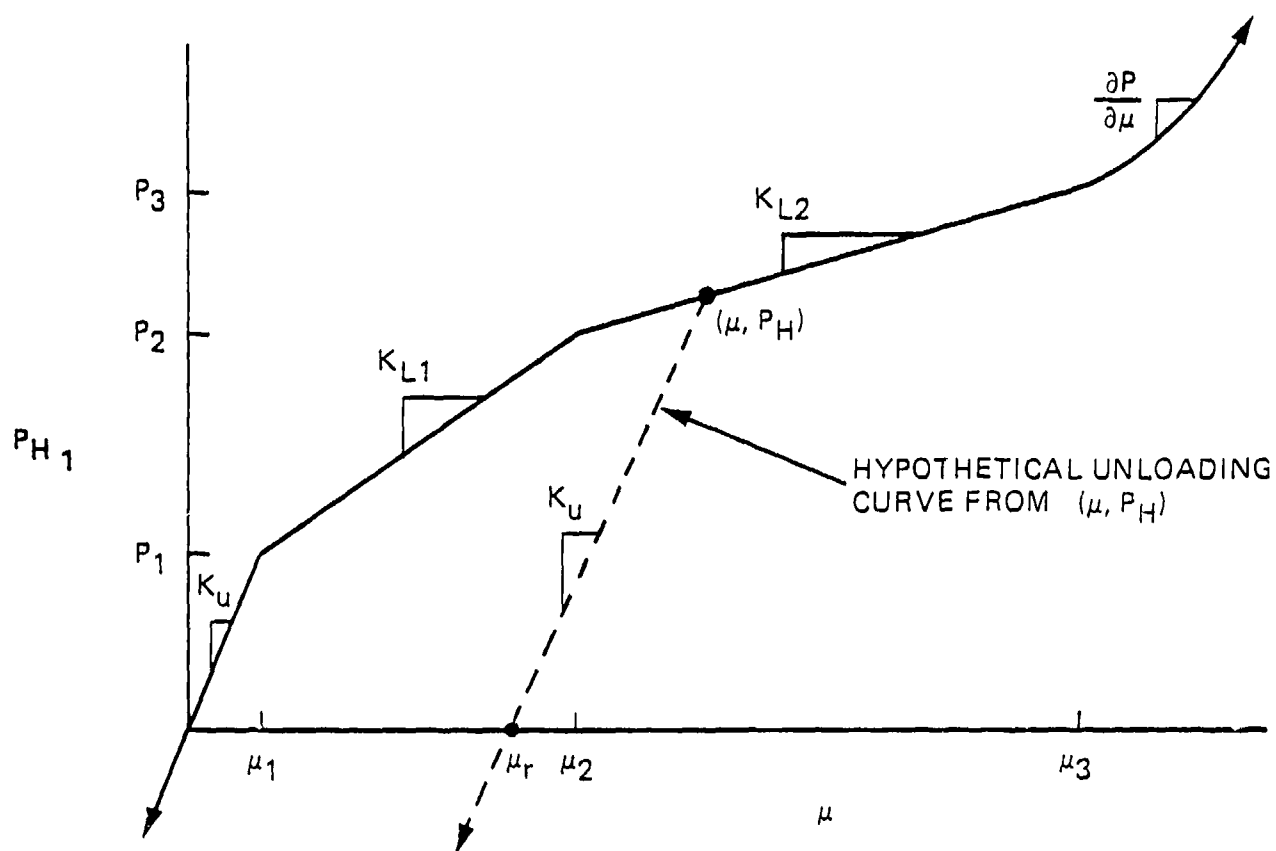


Figure 4-4 Schematic of CIST-15 hydrostat.

1.  $\mu > \mu_3$ , loading and unloading

$$p_H = p_3 + K_m(\mu - \mu_3) - (K_m - K_z) \mu_s (1 - A_e)$$

$$A_e = \exp [(\mu_3 - \mu)/\mu_s]$$

2.  $\mu^* < \mu \leq \mu_3$  (virgin loading curve)

$$p_H = \begin{cases} K_U \mu & \mu \leq \mu_1 \\ p_1 + K_{L1} (\mu - \mu_1) & \mu_1 < \mu \leq \mu_2 \\ p_2 + K_{L2} (\mu - \mu_2) & \mu_2 < \mu \leq \mu_3 \end{cases}$$

3.  $\mu \leq \mu^*$  (unloading curve)

$$p_H = K_U (\mu - \mu_r)$$

$$\mu_r = \mu^* - p_H^*/K_U$$

$\mu_r$  is the x-intercept of the unloading curve of slope  $K_U$  which passes through  $(\mu^*, p_H^*)$ , where  $\mu^*$  is the lesser of the two values of  $\mu_{\max}$ , the maximum compression the soil element has experienced, and the current value of  $\mu$ .

The constants,  $\mu_1, \mu_2, \mu_3, \mu_s, K_m, K_z, K_U, K_{L1}, K_{L2}, p_1, p_2, p_3, G, T$ , and  $e_0$  are defined separately for each CIST test.

The shear modulus is calculated as a function of  $\mu$ , and is the lesser of the values of  $\Delta \times K$  and  $\Delta \times K_z$ , where

$$\Delta = \frac{3}{2} \left( \frac{1-2\nu}{1+\nu} \right),$$

and

$$K = \begin{matrix} K_U & \mu & \mu_1 \\ K_{L1} & \mu_1 < \mu & \mu_3 \\ K_{L2} & \mu_2 < \mu & \mu_3 \\ K_m - (K_m - K_z) \exp [(\mu_3 - \mu)/\mu_s] & \mu > \mu_3 \end{matrix}$$

and  $K_z$  and  $\nu$  (Poisson's ratio) are constants.

The yield stress is calculated as a function of  $p$ , and optionally,  $e$ . Figure 4-5 shows a generalized plot of yield stress versus pressure. The equations are:

$$Y = Y' \quad (\text{no energy dependence})$$

$$Y = Y' \times (1 - e/e_s) \quad (\text{with energy dependence}), \text{ and}$$

$$Y' = \begin{matrix} \max & 0, & c_1 (1 - P/T_1) & P & 0 \\ \min & (c_1 + s_1 P, Y_1) & P & > 0 \end{matrix}$$

The constants  $C_1$ ,  $T_1$ ,  $Y_1$  and  $S_1$  describe the unconfined compressive strength, the tensile strength, the maximum yield strength, and the shape of the failure curve in the intermediate pressure region, respectively.

The CIST data used were those derived for the top soil layer for Event 15, performed at the White Sands Missile Range. The constants used in the calculation are summarized in Table 4-3. Figure 4-6 shows the CIST-15 compressibility curve from 0 to 20.0 GPa (0 to 200 kbar). It is this region which is important for the JANGLE S calculation because the pressure contour of interest (7.2 GPa) and the total impulse across it are defined by the hydrostat in this pressure region.

79-4-128

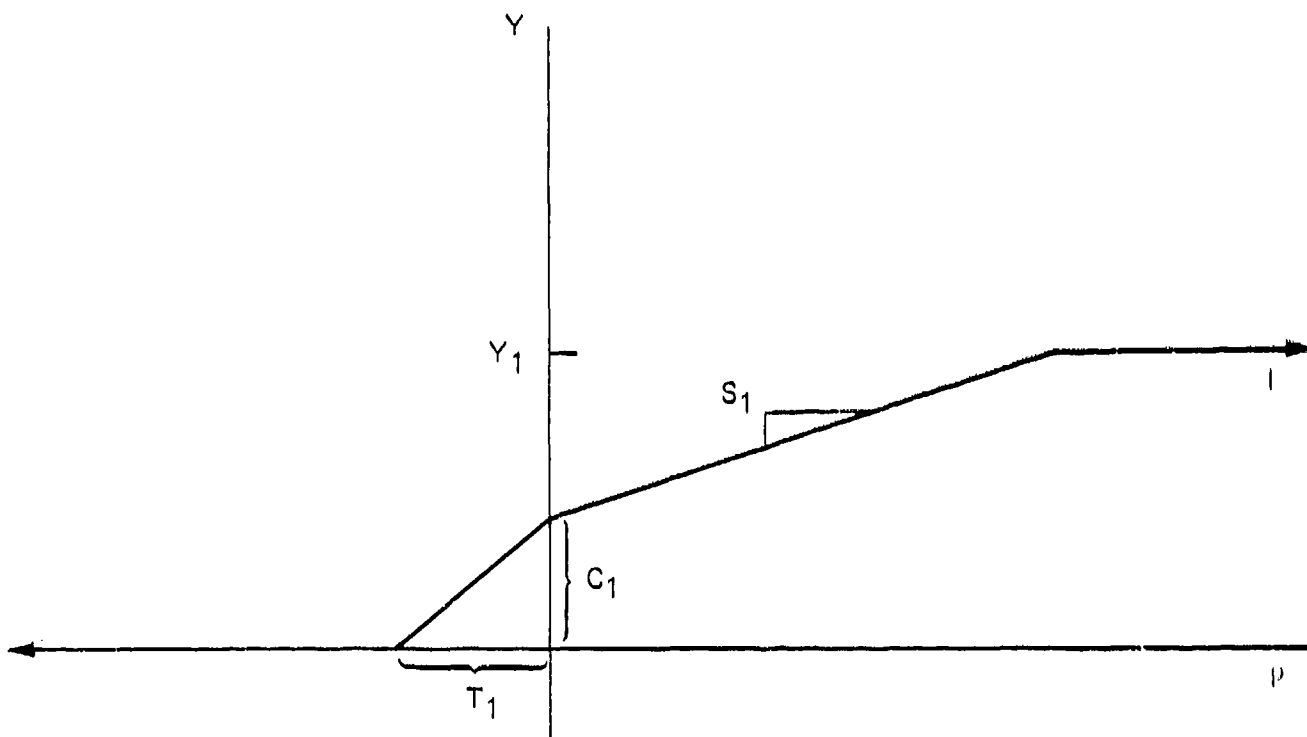


Figure 4-5 Schematic of CIST-15 yield surface.

TABLE 4-3

CIST MODEL CONSTANTS FOR EVENT 15,  
USED TO DESCRIBE THE ALLUVIUM AT THE JANGLE S SITE

| CIST Constant | 2DELK Value                    | SI Value                |
|---------------|--------------------------------|-------------------------|
| $\rho_c$      | 2.13 g/cm <sup>3</sup>         | 2.13 Mg/M <sup>3</sup>  |
| $\nu$         | 0.3                            | 0.3                     |
| $K_u$         | 0.01588 Mbar                   | 1.588 GPa               |
| $K_z$         | 0.01588 Mbar                   | 1.588 GPa               |
| $K_L^1$       | $4.9 \times 10^{-3}$ Mbar      | 0.49 GPa                |
| $K_L^2$       | $1.764 \times 10^{-3}$ Mbar    | 0.176 GPa               |
| $K_m$         | .6897 Mbar                     | 68.97 GPa               |
| $P_1$         | $6.897 \times 10^{-8}$ Mbar    | 6.897 kPa               |
| $P_2$         | $6.8969 \times 10^{-7}$ Mbar   | 68.97 kPa               |
| $P_3$         | $2.650586 \times 10^{-4}$ Mbar | 26.5 MPa                |
| $\mu_1$       | $4.3432 \times 10^{-6}$        | $4.3432 \times 10^{-6}$ |
| $\mu_2$       | $1.3102 \times 10^{-4}$        | $1.3102 \times 10^{-4}$ |
| $\mu_3$       | 0.15                           | 0.15                    |
| $\mu_s$       | 0.25                           | 0.25                    |
| A             | 0.5                            | 0.5                     |
| B             | 1.3                            | 1.3                     |
| $C_1$         | $6.897 \times 10^{-7}$ Mbar    | 68.97 kPa               |
| $T_1$         | $-6.897 \times 10^{-7}$ Mbar   | -68.97 kPa              |
| $S_1$         | 0.6                            | 0.6                     |
| $Y_1$         | $1.38 \times 10^{-4}$ Mbar     | 13.8 MPa                |
| $e_o$         | $1.0 \times 10^{-3}$ eu/g      | 100 joules/g            |
| $e_s$         | 0.1 eu/g                       | 10,000 joules/g         |
| $\mu_o$       | 0.1333                         | 0.1333                  |

79.4-155

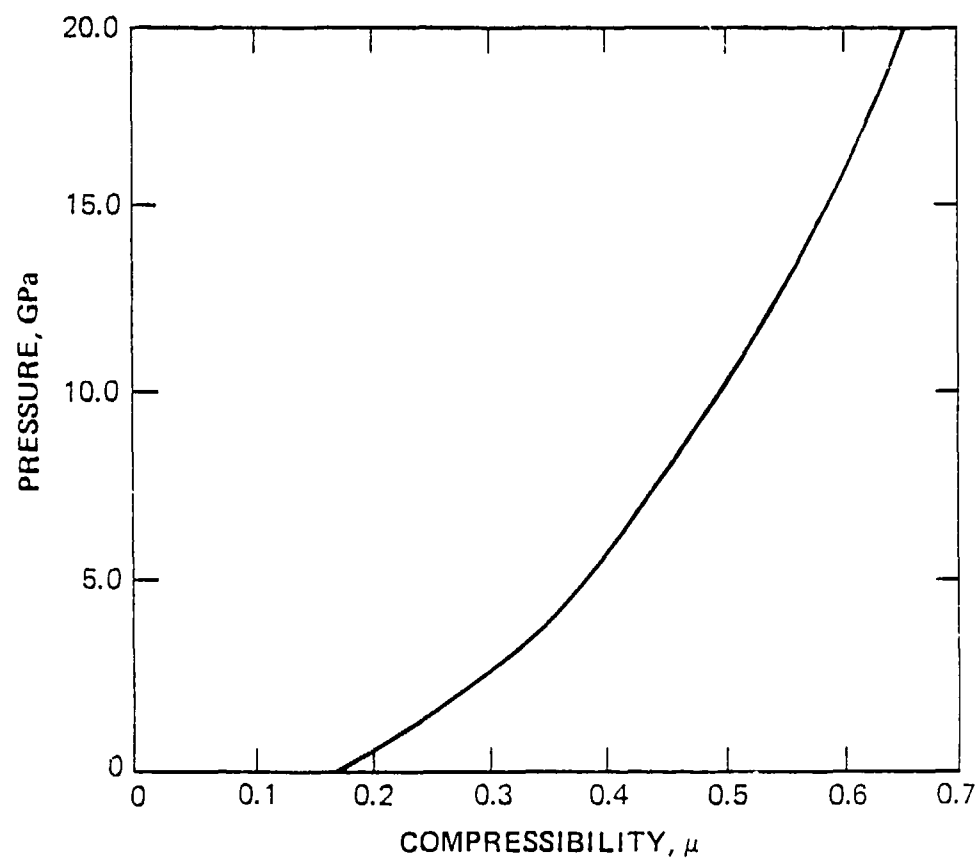


Figure 4-6 CIST-15 hydrostatic compressibility curve.

After the JANGLE 5 calculations were completed, information from CIST Event 5, performed in Area 10 of the Nevada Test Site, was made available. The compressibility curve from this test is given in Figure 4-7. The data from CIST Event 15 are also included for comparison. The Event 15 data are very similar to the Event 5 data; thus, it was unnecessary to rerun the JANGLE 5 calculation. The CIST 15 data were used throughout the program to assure consistency and comparability of results.

Nuclear Source and Air EOS. To model both the nuclear source material and the air as a single material, a special equation-of-state routine was written for PISCES 2DELK. The following information was relied upon in developing the model:

1. The nuclear source can be treated as iron using an ideal gas EOS with a constant gamma ( $\gamma = 1.5$ ).
2. Initially, there is a considerable density mismatch between the air and nuclear source.
3. Once the nuclear source material expanded to 2 to 3 times its initial radius, it could be treated as air.

The model consisted of the following density criteria:

1. For  $\rho < 0.204$  g/cc, cell is nuclear source material (iron). Use ideal gas EOS with a constant  $\gamma = 1.5$ .
2. For  $\rho < 0.08159$  g/cc, cell is air, use ideal gas EOS with a variable gamma, corresponding to a real air EOS.
3. For  $0.08159$  g/cc  $< \rho < 0.204$  g/cc, cell is mixed air and nuclear source material. Use an ideal gas with variable gamma in this "transition region," with gamma given by:

$$\gamma = \gamma_A + \left[ 1.5 - \gamma_A \right] \left[ \frac{\rho - 0.08159}{0.12241} \right]$$



79-4-151

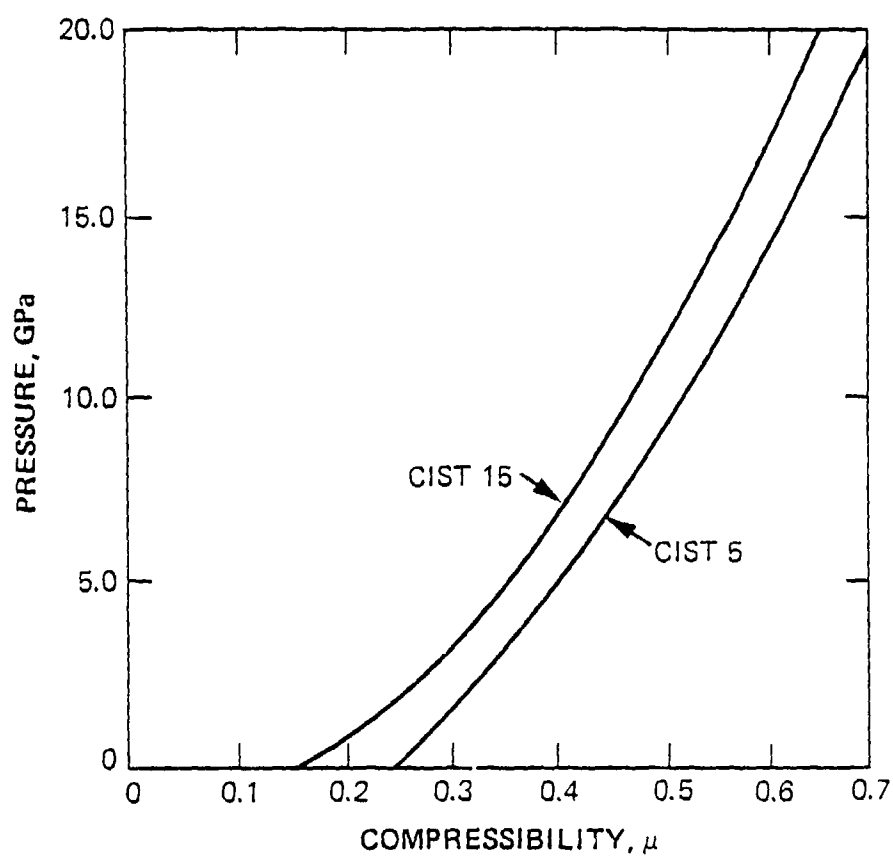


Figure 4-7 Comparison of CIST-5 and CIST-15 compressibility curves.

where  $\gamma_A$  is equal to the real air EOS  $\gamma$  at  $\rho = 0.08159$  g/cc and the current cell internal energy,  $e$ .

A check was made to ensure that the above EOS formulation did not introduce large artificial gradients into the pressure.

4.1.3 Some Results of the JANGLE S 2DELK Calculation. From the JANGLE S calculation the specific results required to design the high explosive charge, as discussed in Section 4.1.1, are the contour in the ground on which the peak pressure was 7.2 GPa (72 kbar), the time of arrival (TOA) of the peak pressure on that contour, and the total impulse delivered across the contour. These results were obtained and are compared in Section 4.2 with the results of the HE calculations performed in order to design the "MINE THROW" charge.

Figure 4-8 shows a two-dimensional vector velocity and material boundary plot at 15  $\mu$ s. The nuclear source has expanded radially outward and vertically upward to a distance of about 2 meters, and has begun to interact with the alluvium below.

The total energy coupled to the alluvium reached a peak of 0.044 kt (3.67 percent of the total yield of 1.2 kt) at 0.067 ms, and then slowly decreased, leveling off at 0.0328 kt (2.73 percent of the total yield) at 0.8 ms.

For the HE simulation, the contour of the ANFO/Soil interface is determined by the requirement that the peak pressure along the contour should be the same in both the MINE THROW simu-

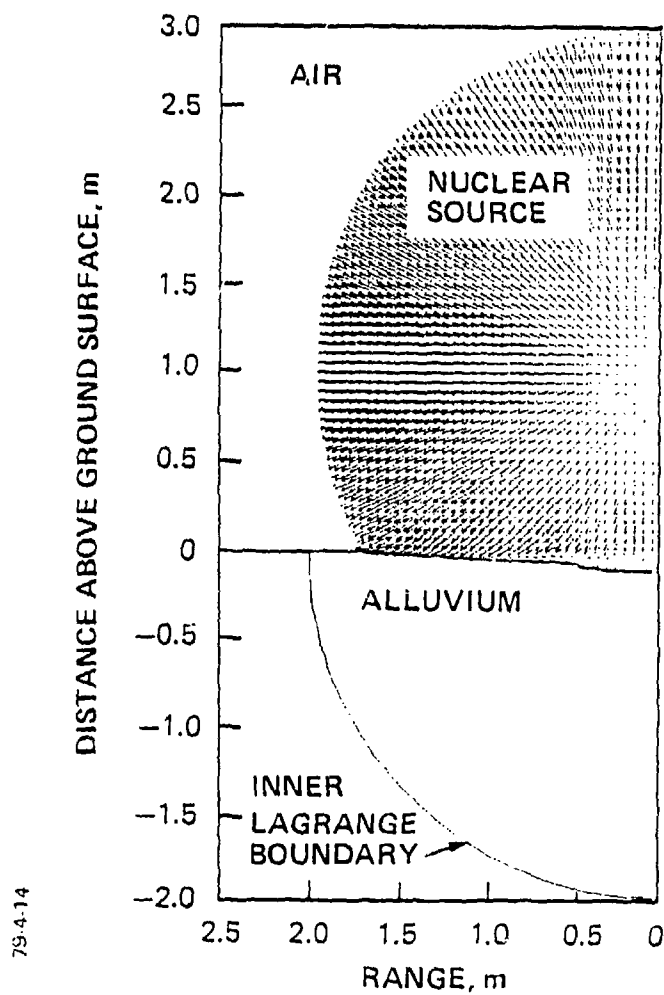


Figure 4-3 PISCES 2DELK vector velocity and material boundary plot from JANGLE S calculation.

lation and in the nuclear event. The value of the peak pressure will be equal to the pressure which occurs when a detonation wave in ANFO reflects from the ANFO/soil interface.

The pressure of reflection of a normally incident detonation wave in ANFO on a soil interface can be found graphically as the intersection of the Hugoniot curves of the two materials in pressure velocity space. Figure 4-9 shows the Hugoniot curves for the CIST-15 soil model and the ANFO, which is modeled with a JWL equation-of-state. The pressure at the intersection of these curves is 7.2 GPa (72 kbar). This value was confirmed with a one-dimensional hydrodynamic calculation.

Since the peak pressure in the MINE THROW simulation and the nuclear event should be equal, the ANFO/soil contour should be taken to be the contour of the JANGLE S calculation where the peak pressure equals 7.2 GPa (72 kbar). (The complexity of a non-normally incident detonation wave is not considered in the MINE THROW simulation method.) The 7.2 GPa pressure contour from the nuclear calculation is shown in Figure 4-10. This contour is irregular near the surface and was replaced with a contour which was smoothed in that region. Figure 4-11 shows the time of arrival and impulse per unit area around the smoothed contour. Table 4-4 gives the coordinates, impulse and arrival times around the smoothed contour.

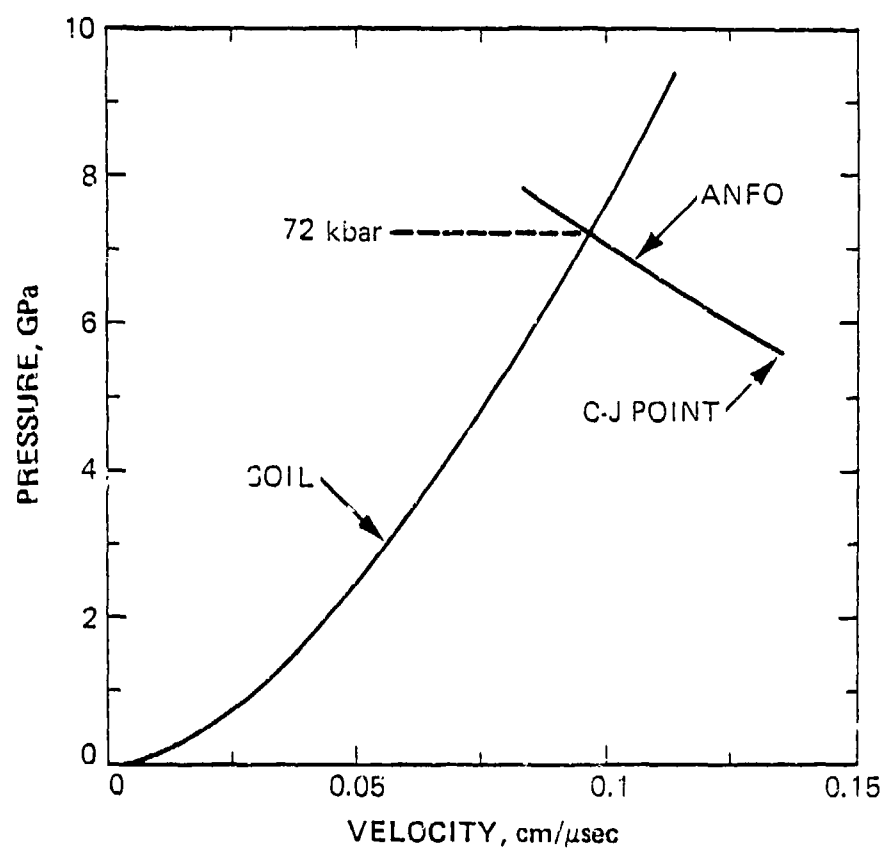
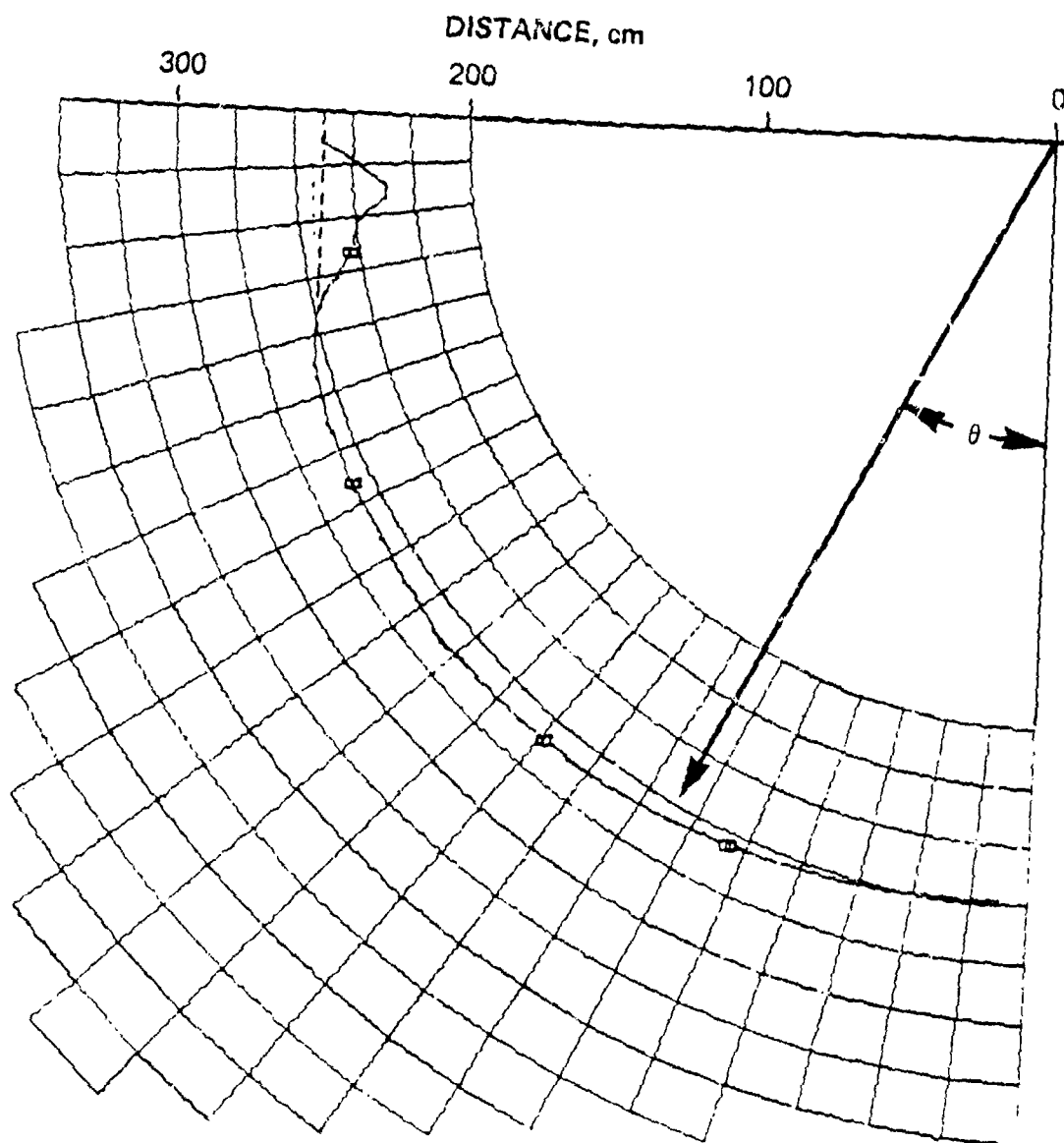


Figure 4-9 The intersection of the Hugoniot curves for the CIST-15 soil and ANFO yields a pressure of 7.2 GPa for the reflection of the detonation wave.



79-4-25

Figure 4-10 The 7.2 GPa contour for the nuclear source calculation. (The dashed line near the surface indicates the smoothed contour.)

7S-4 150

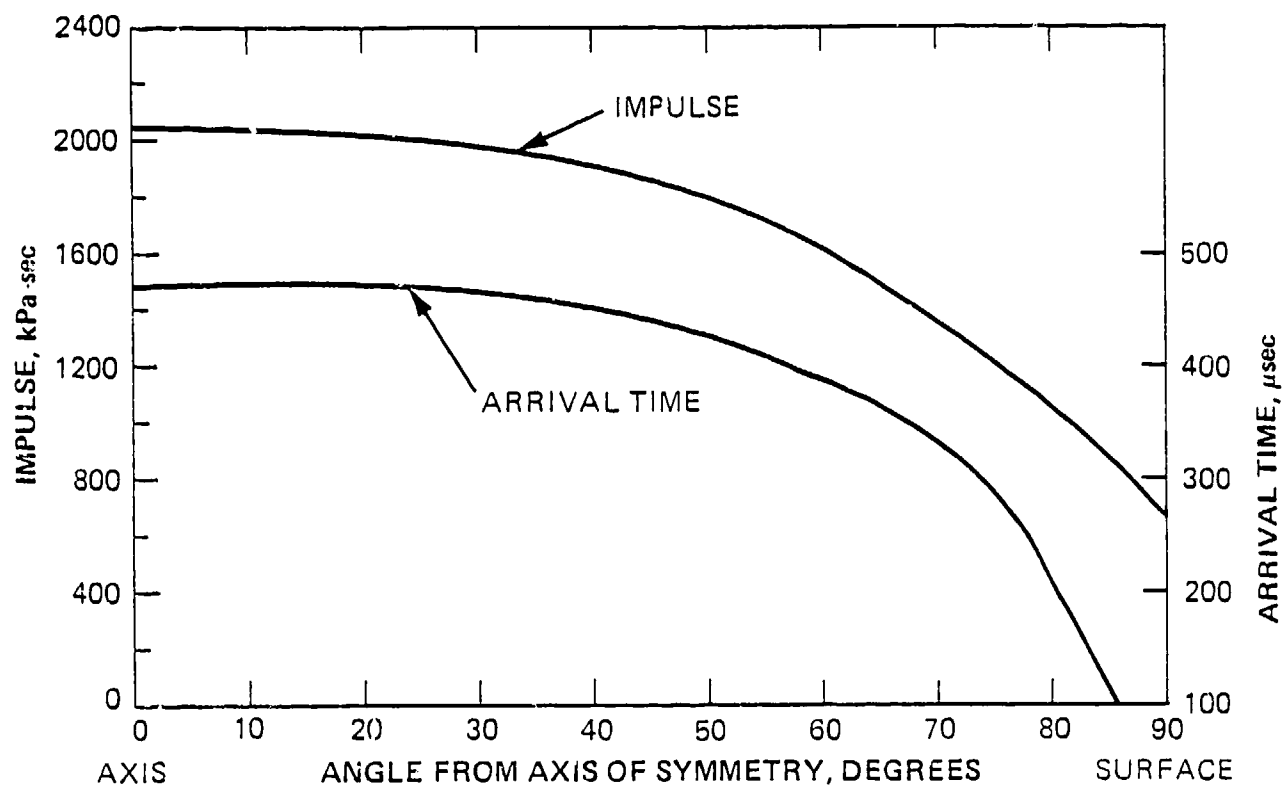


Figure 4-11 Arrival time and impulse along smoothed 7.2 GPa contour from JANGLE S nuclear source calculation.

TABLE 4-4

COORDINATES, IMPULSE, AND ARRIVAL TIME  
ALONG THE SMOOTHED 7.2 GPa CONTOUR - JANGLE S.

| $\theta$<br>(degrees) | radius<br>(cm) | x<br>( $r\cos\theta$ ) | y<br>( $r\sin\theta$ ) | arrival<br>time<br>( $\mu s$ ) | $\int p dt$<br>(kPa-sec) |
|-----------------------|----------------|------------------------|------------------------|--------------------------------|--------------------------|
| 0                     | 259            | 259                    | 0                      | 470                            | 2060                     |
| 5                     | 259            | 259                    | 22.6                   | 470                            | 2050                     |
| 10                    | 260            | 256                    | 45.2                   | 470                            | 2050                     |
| 15                    | 262            | 254                    | 68                     | 470                            | 2030                     |
| 20                    | 263            | 247                    | 90                     | 470                            | 2020                     |
| 25                    | 265            | 240                    | 112                    | 470                            | 2000                     |
| 30                    | 266            | 230                    | 133                    | 466                            | 1980                     |
| 35                    | 268            | 220                    | 154                    | 462                            | 1930                     |
| 40                    | 268            | 205                    | 172                    | 450                            | 1900                     |
| 45                    | 268            | 190                    | 190                    | 435                            | 1860                     |
| 50                    | 269            | 173                    | 206                    | 425                            | 1790                     |
| 55                    | 267            | 153                    | 219                    | 406                            | 1730                     |
| 60                    | 266            | 133                    | 230                    | 385                            | 1620                     |
| 65                    | 266            | 112                    | 241                    | 365                            | 1490                     |
| 70                    | 264            | 90                     | 248                    | 335                            | 1350                     |
| 75                    | 257            | 67                     | 248                    | 285                            | 1220                     |
| 80                    | 252            | 44                     | 248                    | 220                            | 1060                     |
| 85                    | 249            | 22                     | 248                    | 135                            | 860                      |
| 90                    | 248            | 0                      | 248                    | 49                             | 660                      |



#### 4.2 HE SIMULATION OF DIRECT- AND CRATERING-INDUCED GROUND MOTIONS

A one-dimensional calculation in slab symmetry showed that the impulse per unit area delivered to the CIST-15 soil was approximately 16 bar-seconds per meter of ANFO thickness. This value was used to obtain a first approximation to an ANFO thickness profile which would reproduce the desired impulse curve. This first design is shown in Figure 4-12. Detonation times around the inner surface of the ANFO were selected in such a way as to give the correct wave arrival times at the outer contour.

A two-dimensional calculation was made of this first design using the PISCES 2DELK program. The ANFO was computed in an Eulerian grid and the soil was computed in a Lagrangian grid. The impulse for this first design is shown in Figure 4-13. The impulse is low by about twenty-five percent on the axis symmetry and is high near the surface.

To compensate for the deviation of the impulse of design No. 1 from the desired impulse curve, a second calculation was made with an increased explosive thickness near the axis of symmetry and a decreased explosive thickness near the surface. The detonation times for the inner contour of ANFO were adjusted in such a way as to give the correct wave arrival times at the outer contour. A two-dimensional calculation of this design gave virtually the same impulse around the outer contour as design No. 1.

The failure of the increased explosive thickness to increase the impulse near the axis of symmetry seems to be due to a two-dimensional effect. As a result of the 1.067 meter (42 inch)

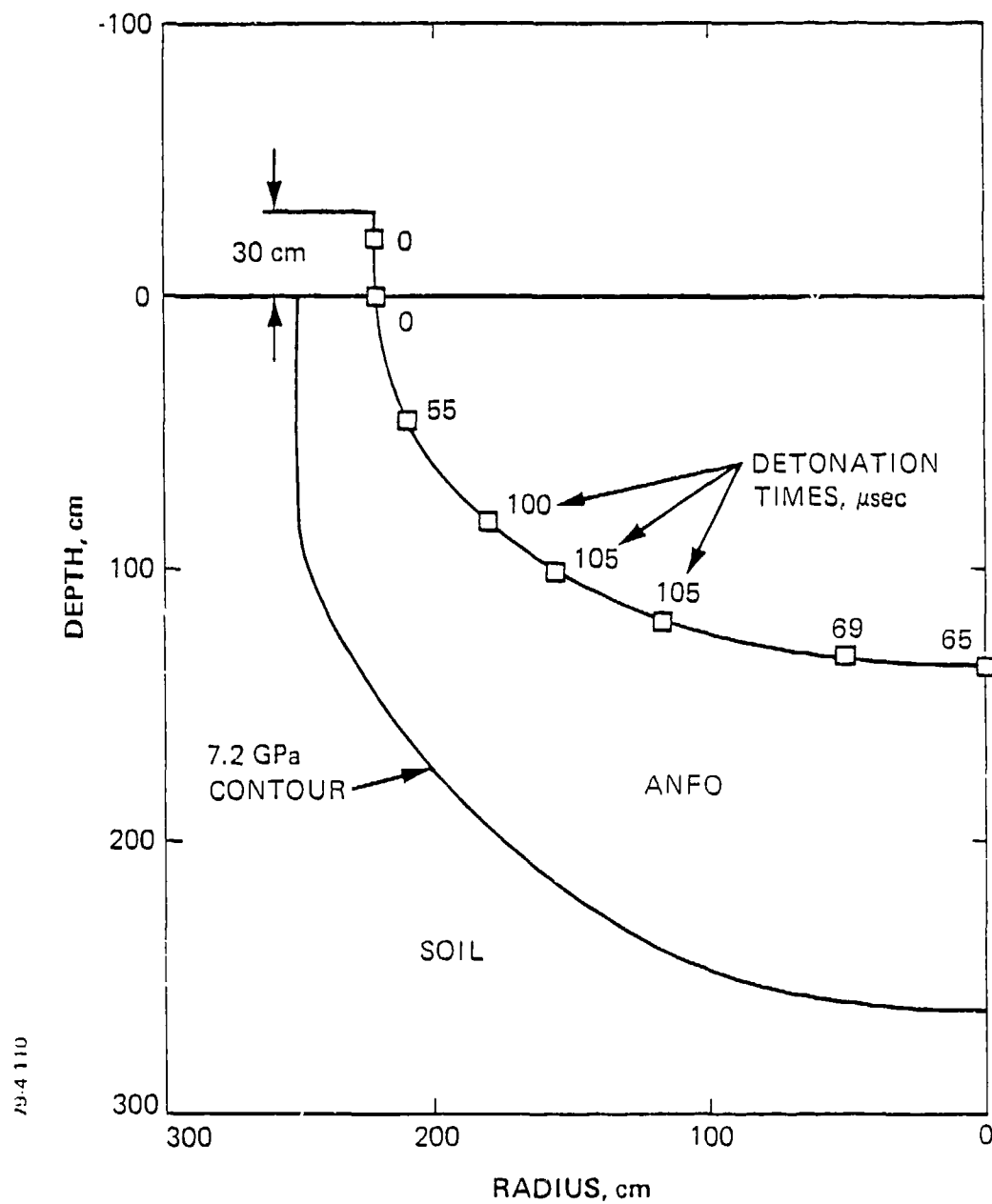


Figure 4-12 Geometry of Design 1.

79.4 148

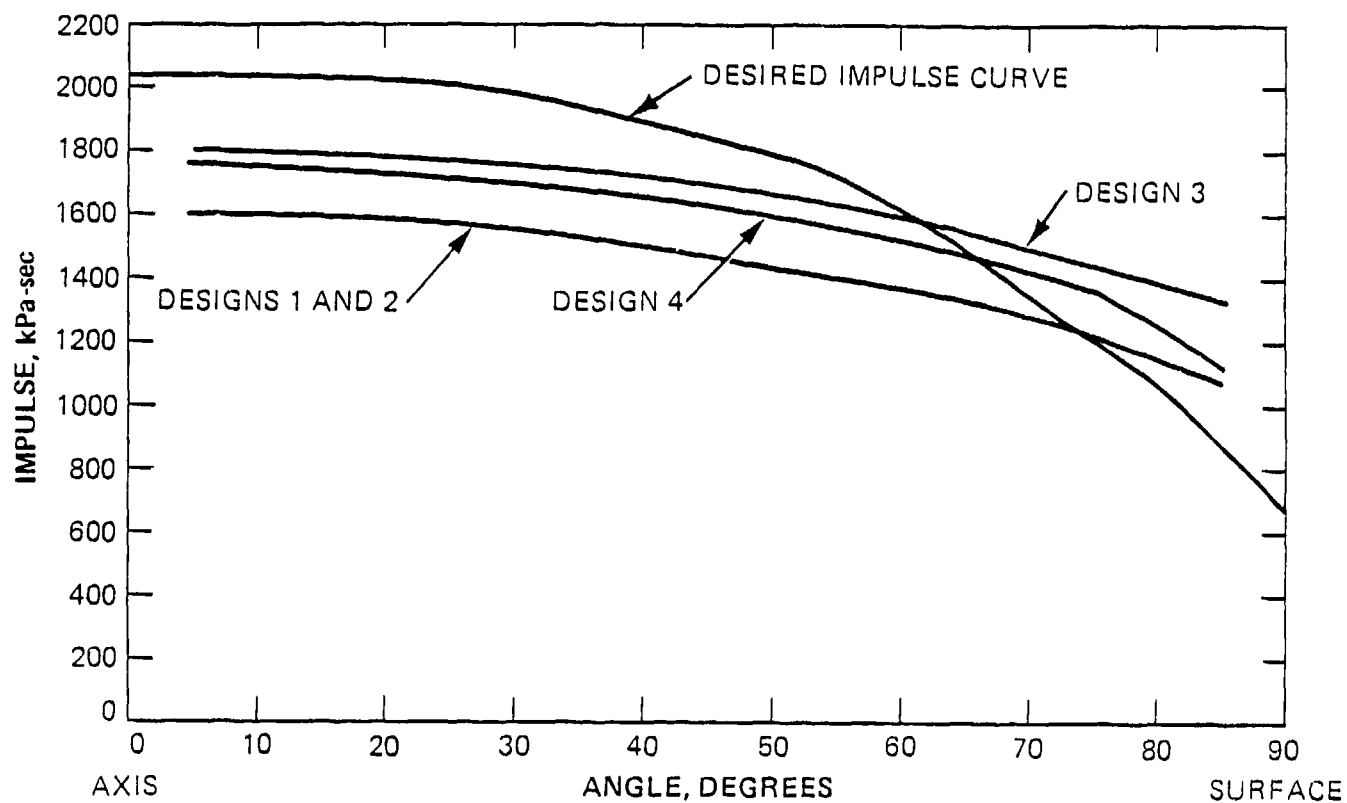


Figure 4-13 Comparison of the impulse for Designs 1, 2, 3 and 4 with the desired impulse curve.

height-of-burst of the nuclear device, the wave arrival time along the ANFO/soil interface is much later on the axis of symmetry than at the surface. As a result, the crater begins forming near the surface earlier than on the axis of symmetry. The widening crater radius near the surface provides an early escape path for the detonation products from the deeper regions of the explosive charge, thereby decreasing the efficiency of the charge there.

This two-dimensional effect is verified by the results of a calculation for a design which used soil tamping. This design, labeled design 2, is shown in Figure 4-14. It is the same as design 1 except for the soil tamping. The impulse computed for this design is virtually the same as for design 1.

To increase the impulse on the axis of symmetry, the soil tamping was extended radially to block the escape path of the detonation products. This design is labeled design 3 and is shown in Figure 4-15. The impulse resulting from this is shown in Figure 4-13. The impulse on the axis of symmetry is indeed increased by this design, but unfortunately the impulse near the surface is also increased. Thus, the effect of blocking the escape path of the detonation products is to increase the impulse everywhere around the outer contour of the explosive.

Figures 4-16 and 4-17 compare the impulse versus time curves for design 3 and the nuclear calculation on the axis of symmetry ( $\theta = 0^\circ$ ) and at  $\theta = 70^\circ$ . The risetime for the nuclear source is much shorter than for the chemical explosive source.

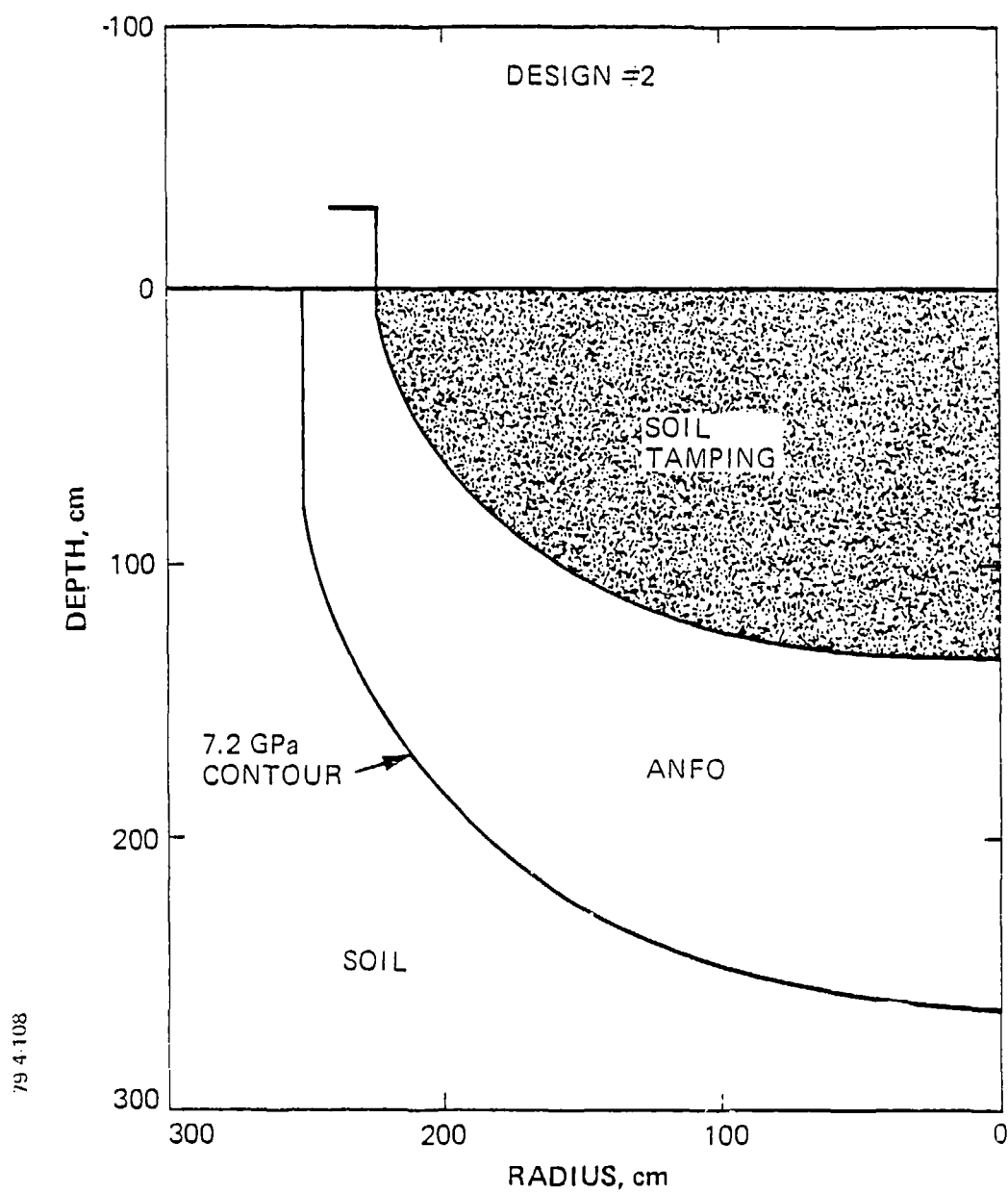


Figure 4-14 Geometry of Design 2 (detonation items same as for Design 1).

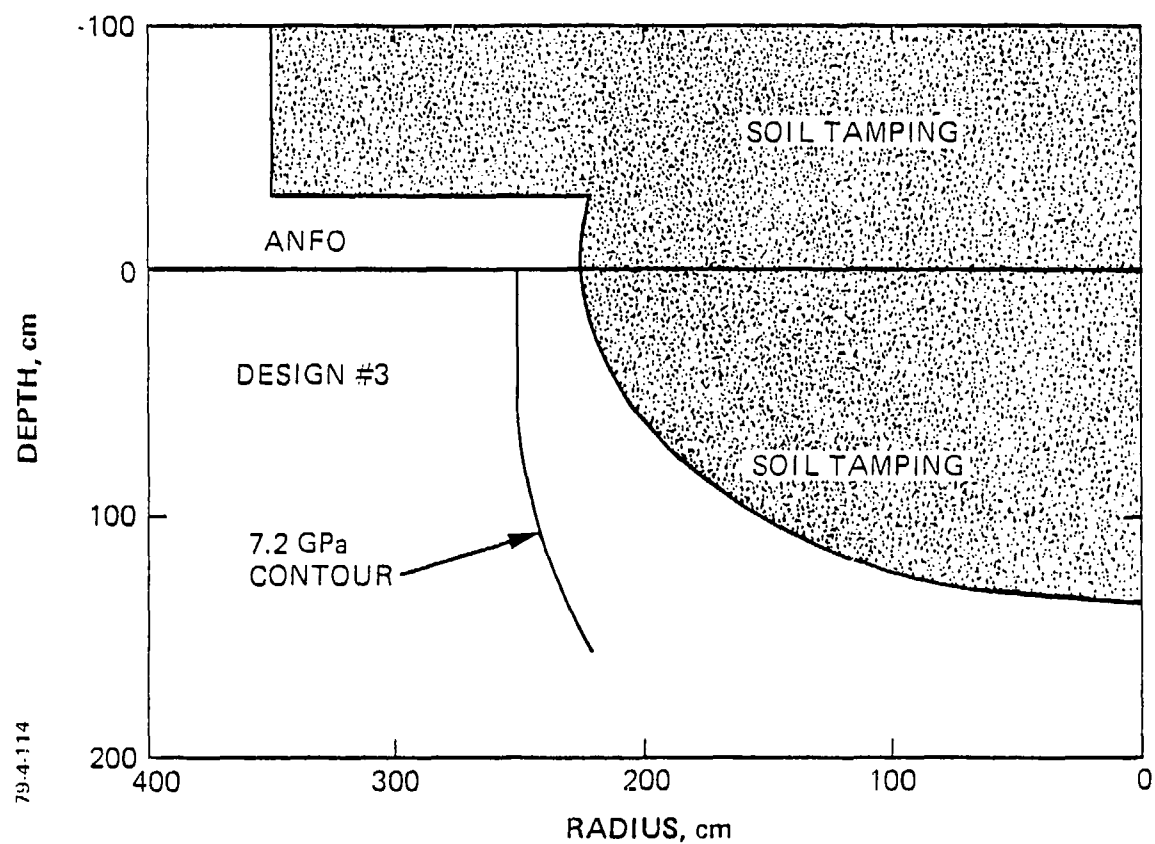


Figure 4-15 Geometry of Design 3 (detonation times same as for Design 1).

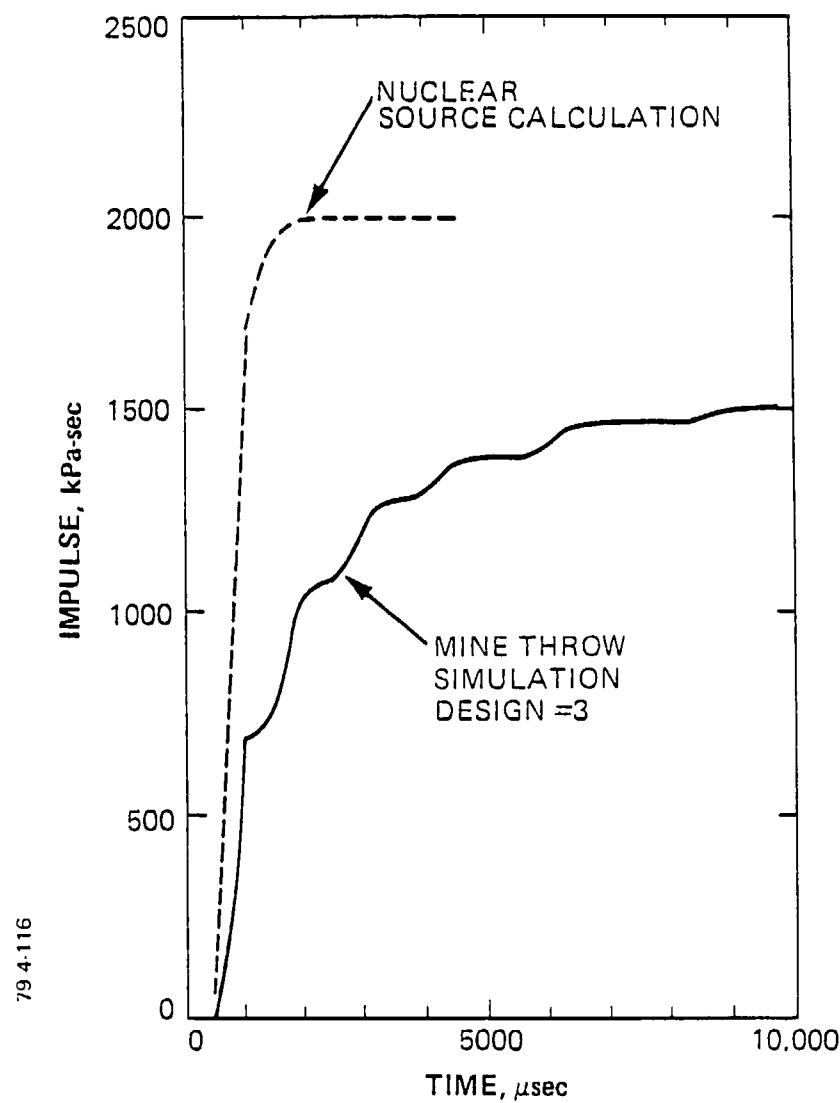


Figure 4-16 Comparison of the impulse versus time curves for the nuclear source calculation and Design 3 on the axis of symmetry.

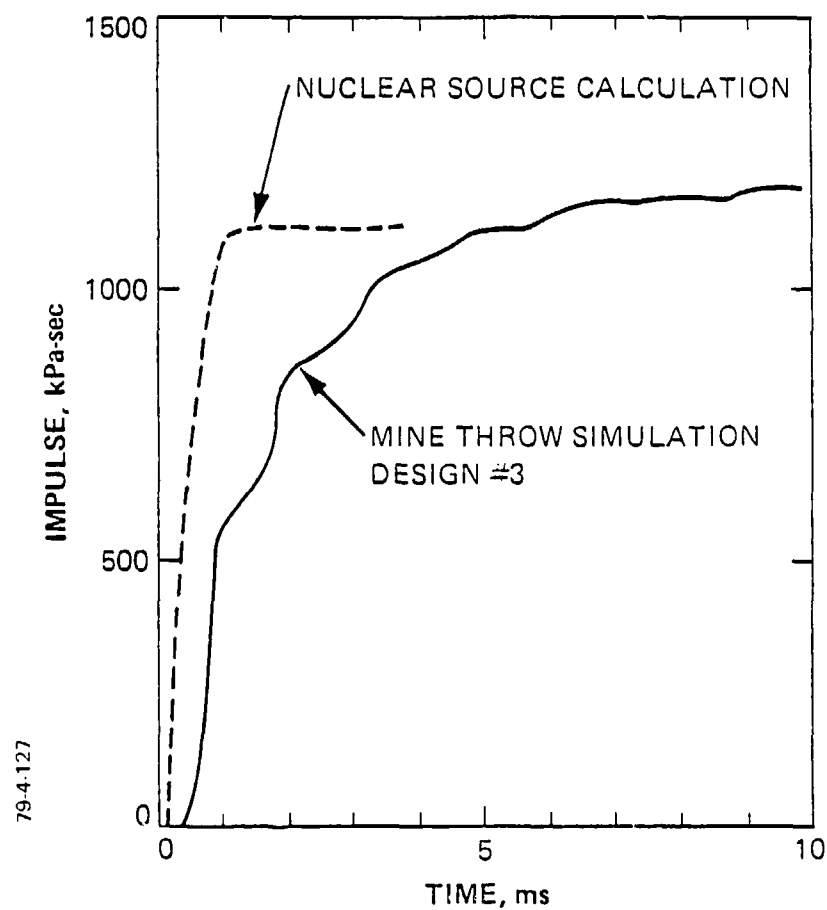


Figure 4-17 Comparison of the impulse versus time curves for the nuclear source calculation and Design 3 at  $\theta = 70$  degrees.



A final design (design 4) attempted to increase the impulse on the axis of symmetry without increasing the impulse near the surface. This design, shown in Figure 4-18 consists of soil tamping up to 1 meter above the ground surface plus an additional meter of ANFO above the surface. The purpose of the upper layer of ANFO is to improve the efficiency of the tamping. Since this design does not block the escape path of the detonation products near the ground surface, it should not raise the impulse there. Figure 4-14 compares the impulse computed for this design with the desired impulse curve and with the other designs. The impulse for this design is lower than design 3 near the surface, as expected.

In conclusion, of the four charge designs studied here, two should be eliminated from further consideration. Design 2 should not be considered because it gives the same results as the simpler design 1, and design 4 should not be considered because it yields only a marginal improvement over the other designs with the addition of the major complexity of a second layer of ANFO. The remaining two designs each have their respective advantages. Design 1 is the simplest design and gives the best comparison with the JANGLE S source calculation near the ground surface. Design 3, which uses tamping, gives the best comparison on the axis of symmetry.

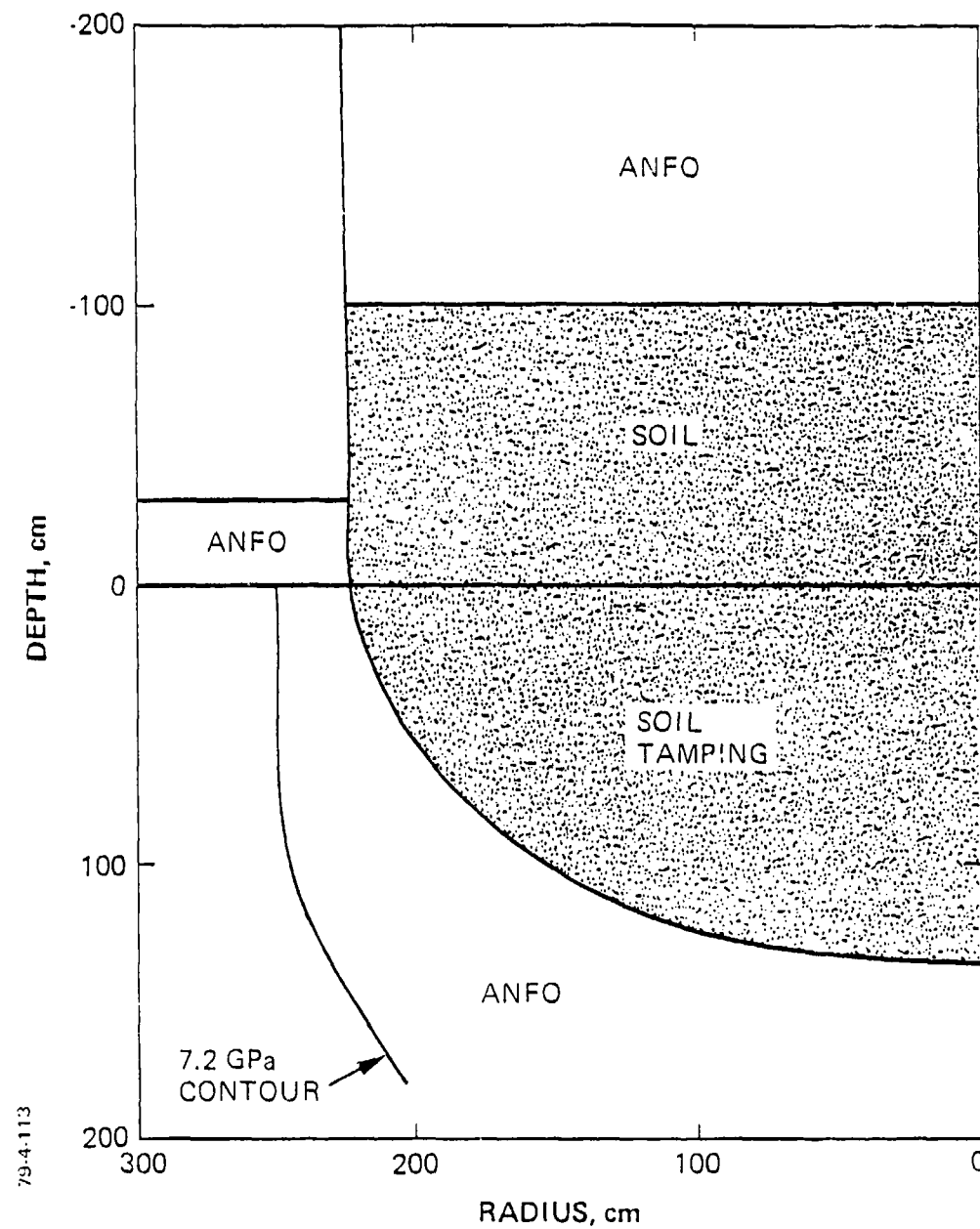


Figure 4-13 Geometry of Design 4 (detonation times around inner contour same as for Design 1); upper layer of ANFO is detonated at  $t = 0$ .

## SECTION 5

### SUMMARY AND RECOMMENDATIONS

Physics International Company supported a DNA-sponsored effort to investigate the feasibility of performing a high explosive experiment which would simulate the direct- and airblast-induced ground motions from a 1-kt nuclear event. A preliminary investigation relying on simple one-dimensional calculations indicated that such a simulation was possible, and a first order design for such a charge was derived. Certain technical problems remained which required further experimental work. These were pointed out at the end of the feasibility study. In order of importance, the areas recommended for further experimental and design work are:

- determination of the detonation properties of ANFO in thin sheets
- design of a multipoint initiation system
- assessment of proper number and spacing of the detonators
- evaluation of the low overpressure characteristics of the surface charge.

Substantial progress was made towards determining the detonation properties of thin ANFO sheets, although not enough information was obtained to allow for the design of a more

accurate surface charge. It was found that the detonation velocity of the ANFO in thin sheets is a function of the absolute thickness of the charge. Multiple interactions of the ANFO detonation products and the air shock with the ground surface in the region between the charge and the surface produced higher pressures than expected, and very little pressure data were obtained.

An acceptable initiation system was designed and tested. Detonator spacing was investigated calculationally, and an acceptable formula for determining the detonator spacing for the surface charge found, provided that ANFO behaved in a "semi-ideal" manner. Testing of the detonator spacing formula was not carried out because the difficulties in determining the actual detonation properties of thin sheets of ANFO made such testing useless.

The future need for nuclear effects simulation will probably require additional work in this area, and we believe that it is feasible to construct an HE charge which would adequately simulate the effects addressed in this report. Different types of explosives (as opposed to ANFO) would probably be better candidates for HE simulations requiring thin sheets of explosives. Gelled, diluted nitromethane was detonated in thin sheets as part of this program, and its detonation properties were found to be very close to ideal. This explosive might therefore be a good candidate for further investigation.

From scale model tests it was found that some enhancement of peak surface overpressures in the 680 kPa (100 psi) range can be

obtained from sheet charges, but little or no enhancement is found at overpressures lower than 680 kPa. Thus, an additional high explosive charge would have to be designed to simulate the 1 kt nuclear airblast.

Based on the results obtained in the course of this investigation, we make the following specific recommendations for a continued effort to develop a high explosive source which will simulate the airblast-induced ground motion and cratering resulting from a 1-kt nuclear surface burst:

1. Investigate the use of explosives other than ANFO for charge geometries requiring thin sheets (less than 1-m-thick).

2. Coordinate the current charge design with a large, spherical or cylindrical HE charge to simulate the surface airblast below 680 kPa.

3. Perform a smaller size (1/4 to 1/3 full size) test of the entire charge system prior to inclusion of a full size event in any future DNA field test program.

## REFERENCES

1. T. F. Stubbs, J. A. Kochly, D. S. Randall, F. M. Sauer, and C. T. Vincent, MINE THROW I--A Cratering and Ground Motion Simulation Technique, DNA 3365F, Defense Nuclear Agency, July, 1974.
2. A. C. Buckingham, S. L. Hancock, M. W. McKay, and D. L. Orphal, Calculations of CACTUS Ground Motion and Design of the MINE THROW II Charge, PIFR-383 Volume III, Physics International Company, March, 1973.
3. H. L. Brode, Height of Burst Effects at High Overpressures, DASA 2506, Defense Atomic Support Agency, 1970.
4. Maj. W. Ullrich, private communication, 8 September 1976.
5. E. L. Lee, H. C. Horning, and J. W. Kury, Adiabatic Expansion of High Explosive Detonation Products, UCRL-50422, Lawrence Livermore Laboratory, May, 1968.
6. L. Penn, F. Helen, M. Finger, and E. Lee, Determination of Equation-of-State Parameters for Four Types of Explosive, UCRL-51892, Lawrence Livermore Laboratory, August, 1975.
7. M. W. McKay, S. L. Hancock, and D. Randall, Development of a Low-Density Ammonium Nitrate/Fuel Oil Explosive and Modeling of its Detonation Properties, DNA3351F, Defense Nuclear Agency, October, 1974.
8. R. H. Cole, Underwater Explosions, Princeton University Press, Princeton, N. J. 1948.
9. M. McKay, S. Hancock, and D. Randall, A Numerical Study of Detonations in a Slow Burning Explosive, DNA3351F, Defense Nuclear Agency, October, 1974.
10. Maj. G. G. Leigh, A Calculation of the Blast Wave from the Constant Velocity Detonation of an Explosive Sheet, AFWL-TR-71-137, AFWL, November, 1971.
11. J. Amend III, Cylindrical In-Situ Tests at Selected Nuclear and High Explosive Test Sites, AFWL-TR76-209, AFWL, February, 1977.
12. Capt. W. Ullrich, AFWL/DES, private communication, September, 1976.
13. J. H. Tillotson, Metallic Equations of State for Hypervelocity Impact, General Atomic Report GA-3216, 1962.

## APPENDIX

### OVERPRESSURE WAVEFORMS AND OVERPRESSURE IMPULSE FROM STANDARD SOURCE AIRBLAST TESTS

Test 18: 10.5 kilogram (23 lb) nitromethane  
cylinder

Test 19: 10.5 kilogram (23 lb) model standard  
source charge, EL 506 C-1 sheet  
explosive

79-7-51

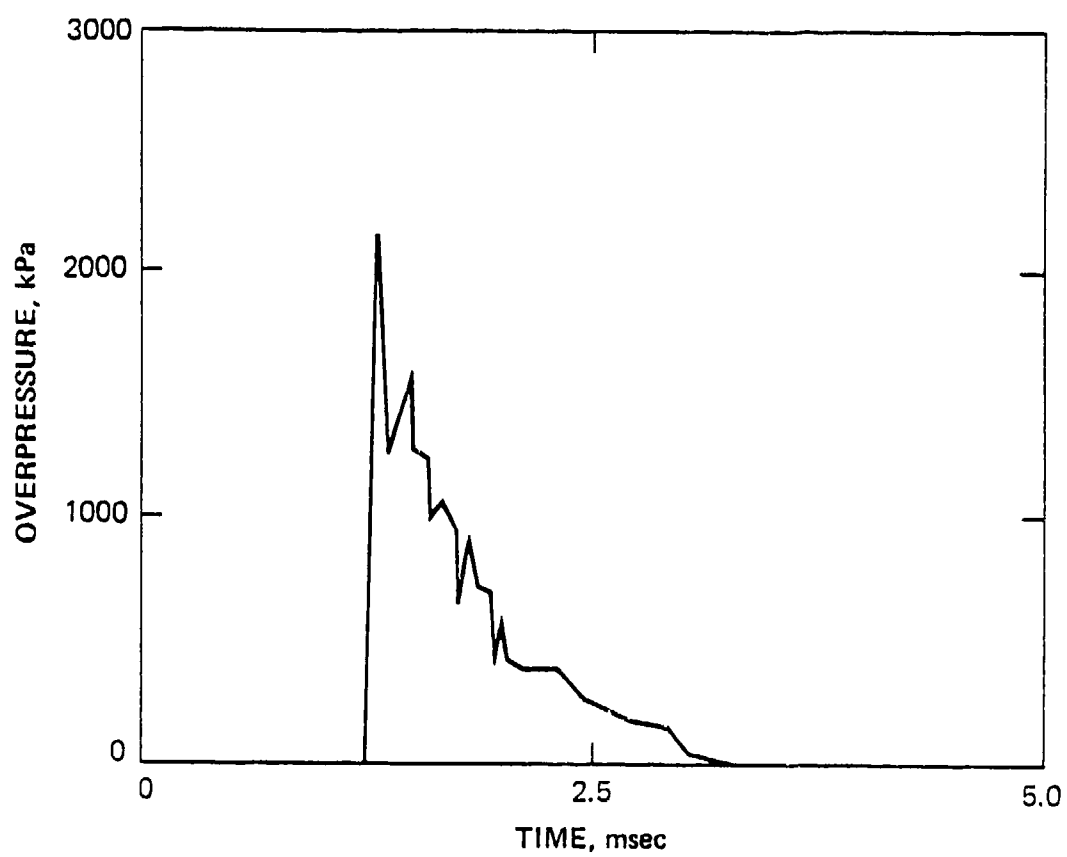


Figure A-1 Overpressure at 1.33 m (6 ft) station, Test 18.



79.741

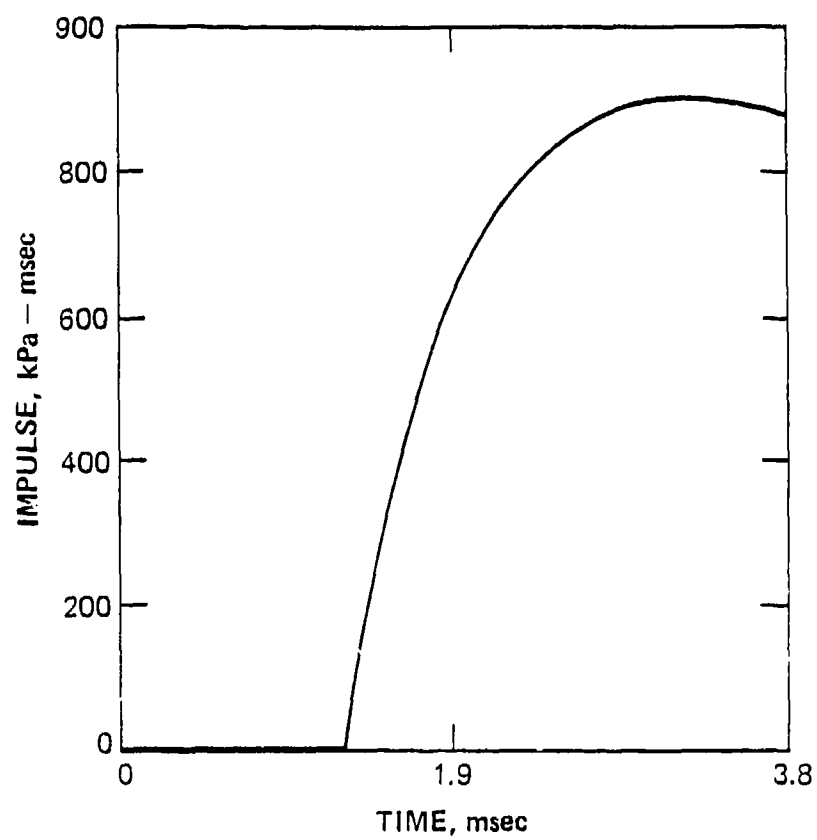


Figure A-2 Impulse at 1.33 m (6 ft) station,  
Test 18.

79 7-62

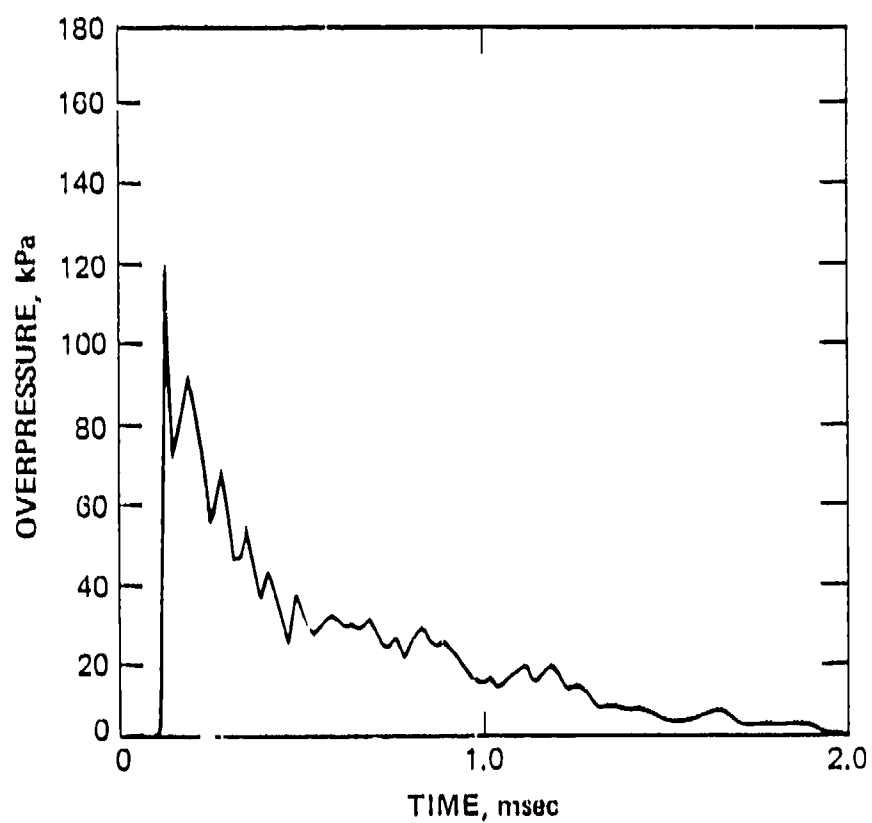


Figure A-3 Overpressure at 3.66 m (12 ft) station, Test 18.

79.7.57

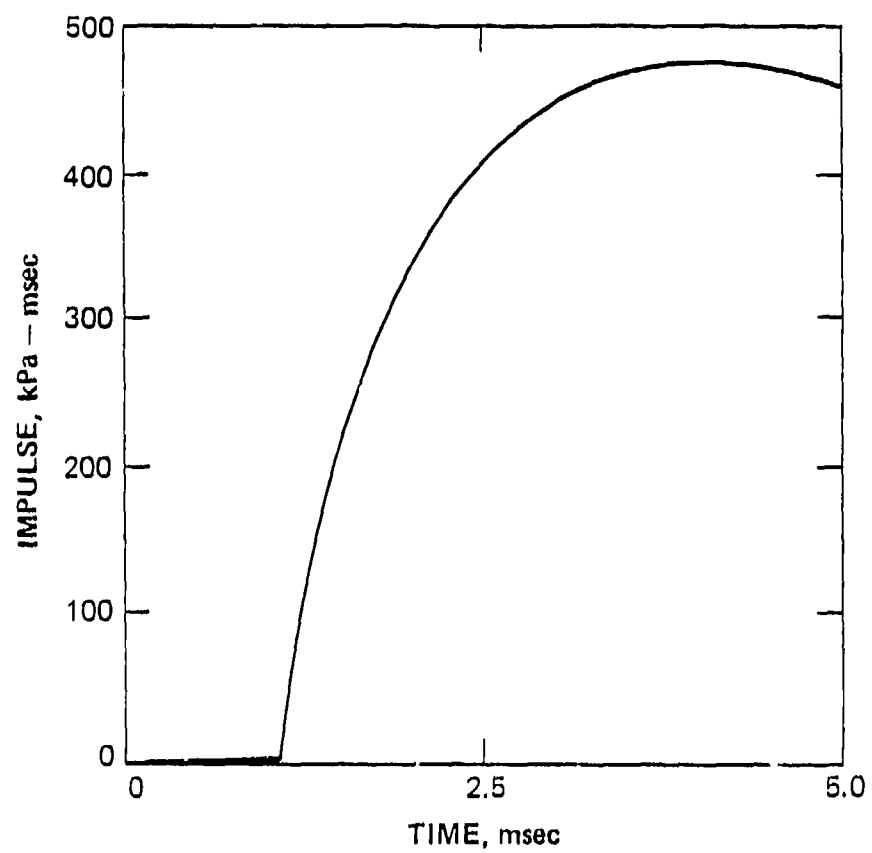


Figure A-4 Impulse at 3.66 m (12 ft) station, Test 18.

79-7-59

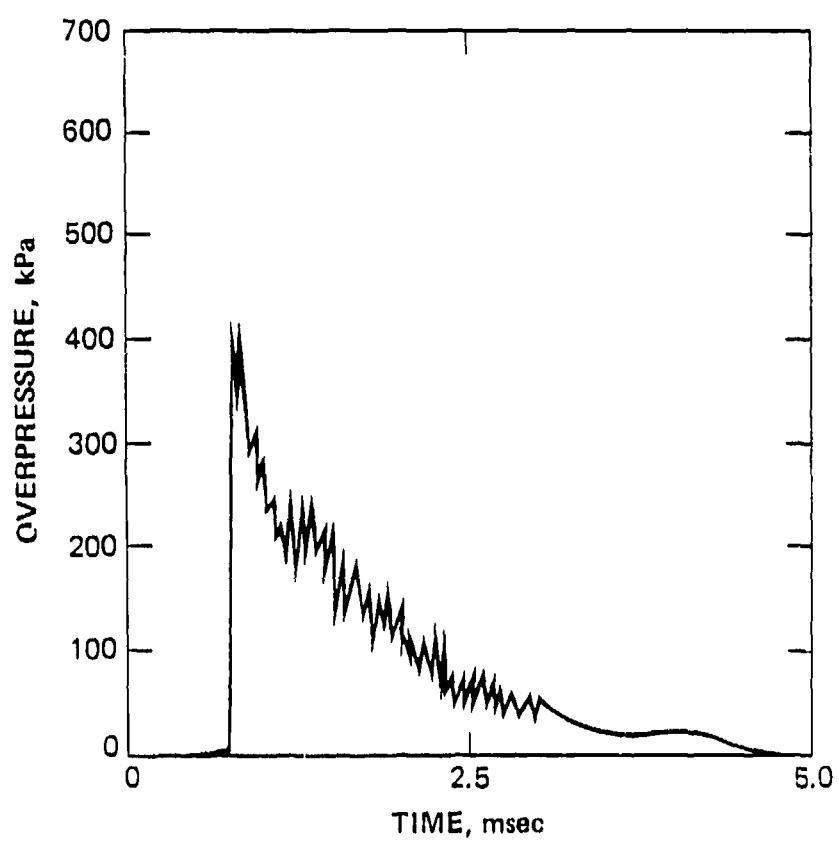


Figure A-5 Overpressure at 4.57 m  
(15 ft) station, Test 18.

79 7 54

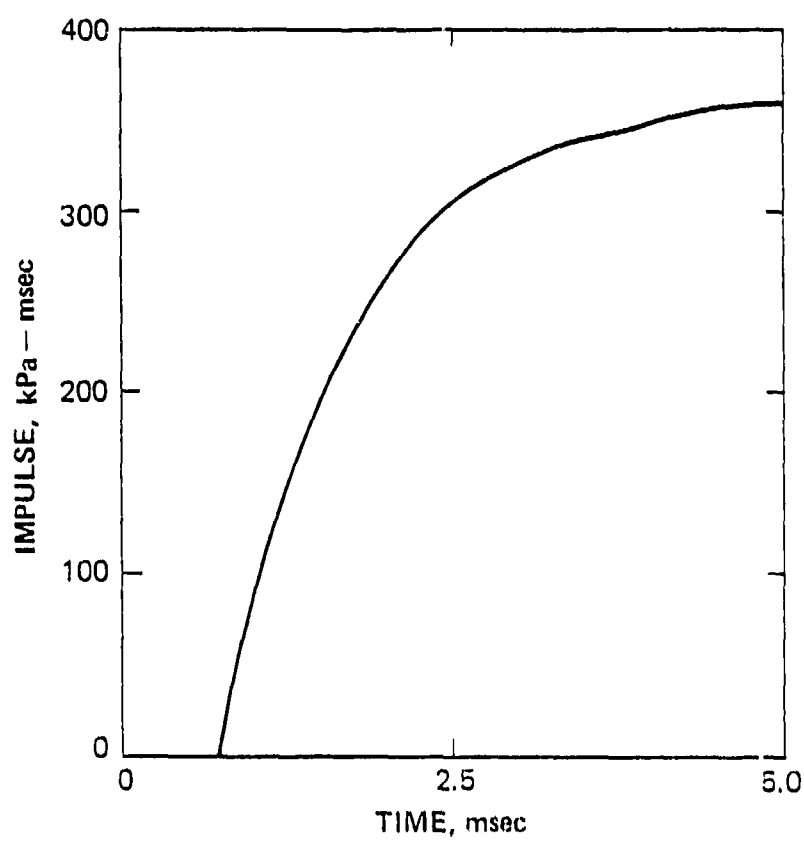


Figure A-6 Impulse at 4.57 m (15 ft) station, Test 18.

79 7 52

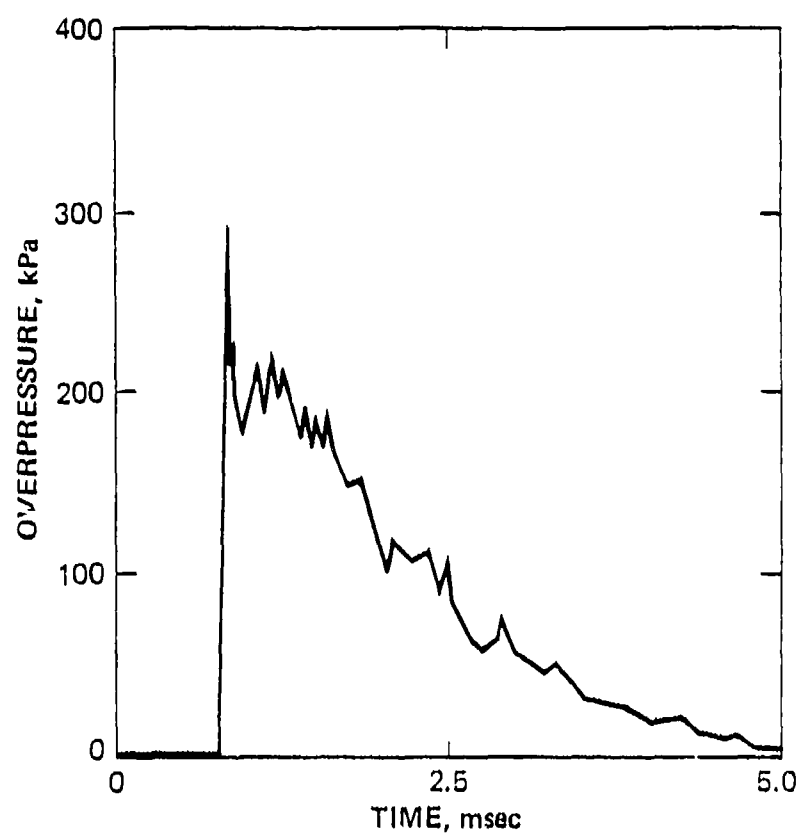


Figure A-7 Overpressure at 5.49 m  
(18 ft) station, Test 13.

79 7 52

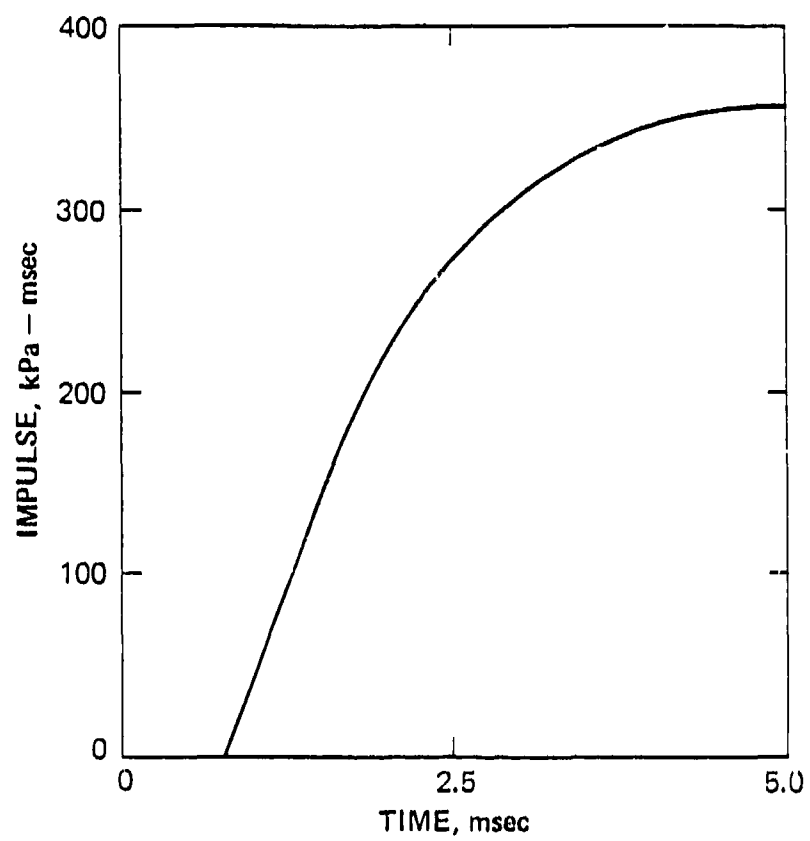


Figure A-8 Impulse at 5.49 m (18 ft) station, Test 18.

79-746

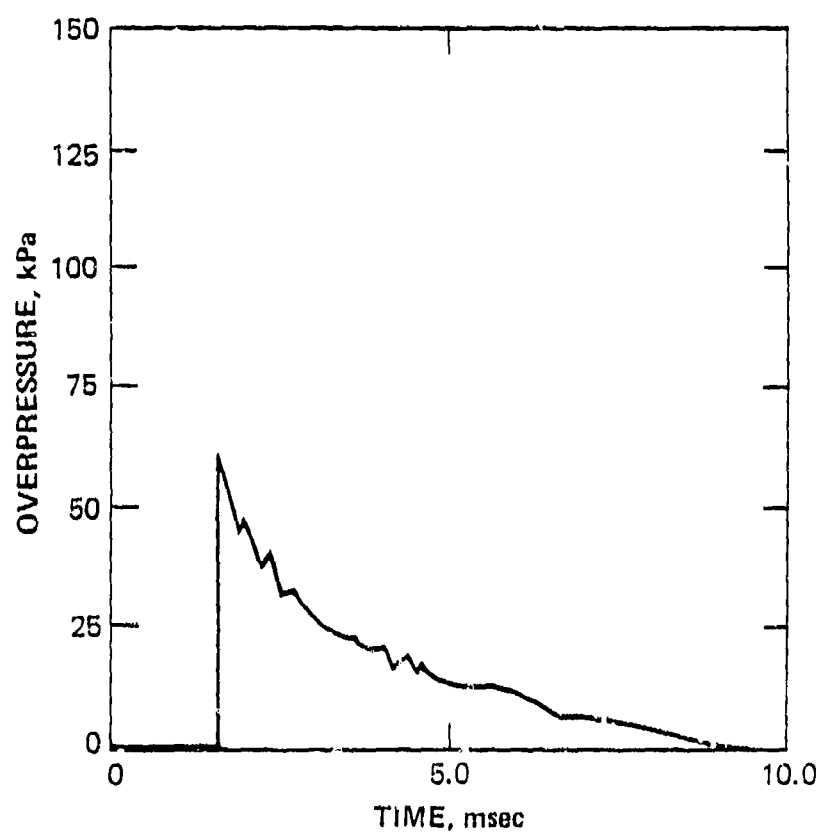


Figure A-9 Overpressure at 8.53 m (28 ft) station, Test 18.



79 7-45

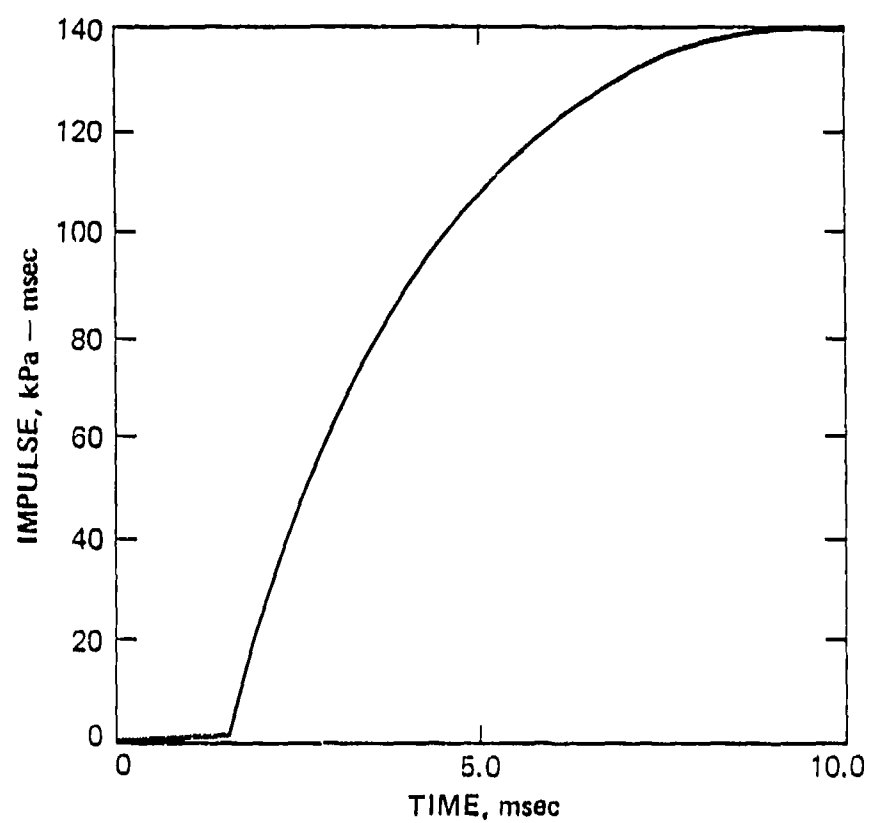


Figure A-10 Impulse at 8.53 m (28 ft) station,  
Test 18.

79.7.61

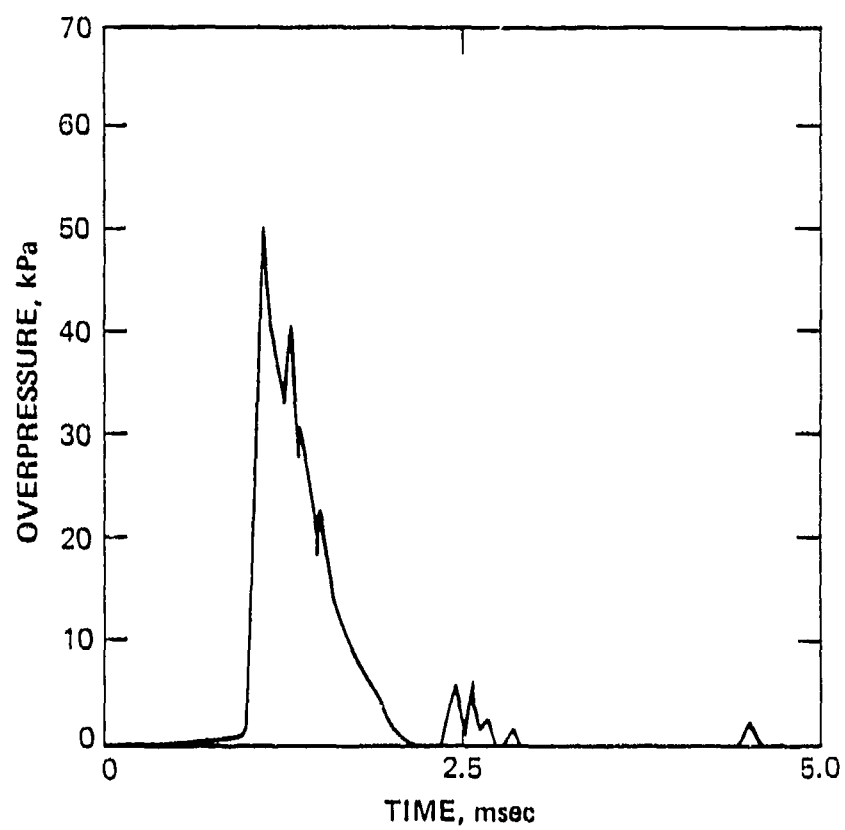


Figure A-11 Overpressure at 13.1 m (43 ft) station, Test 18.

79 7 55

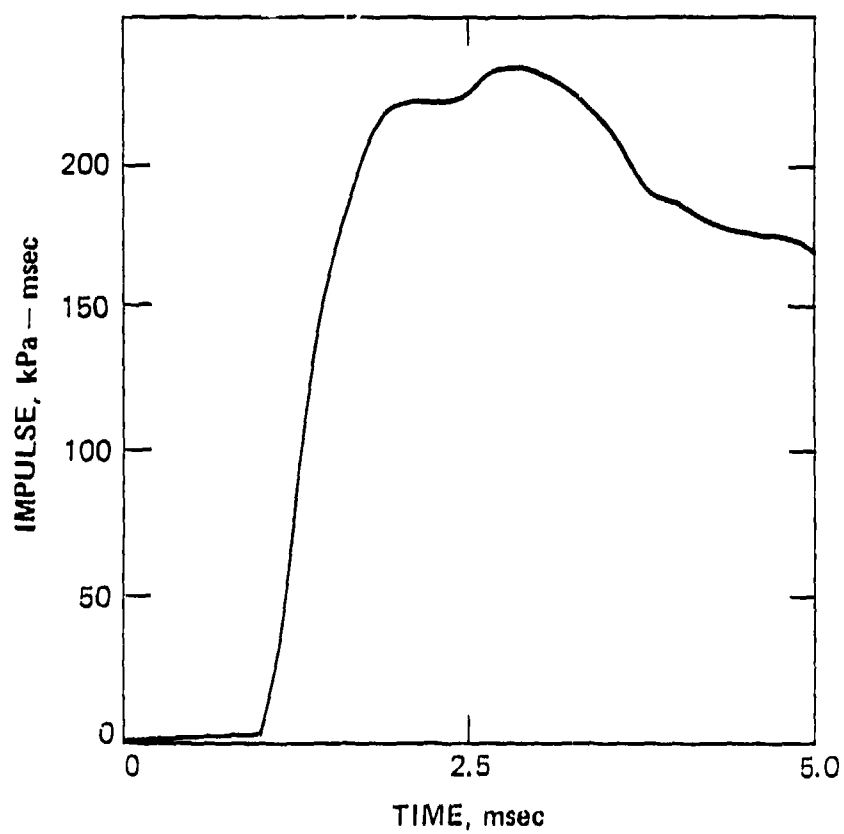


Figure A-12 Impulse at 13.1 (43 ft) station, Test 18.

79 7 39

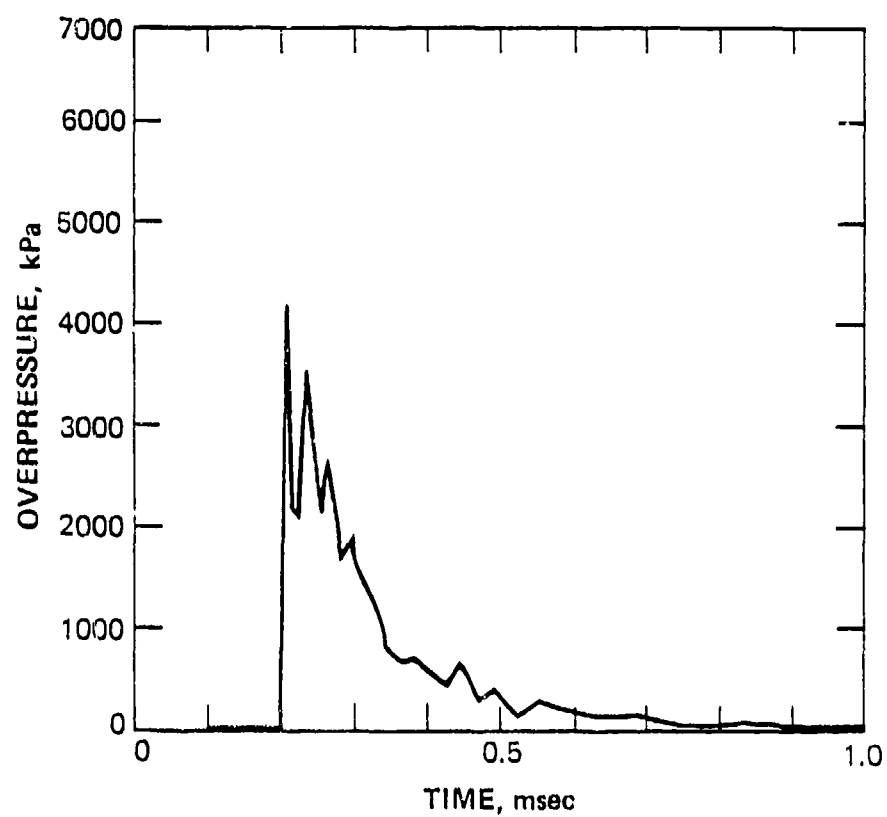


Figure A-13 Overpressure at 1.33 m (6 ft) station, Test 19.

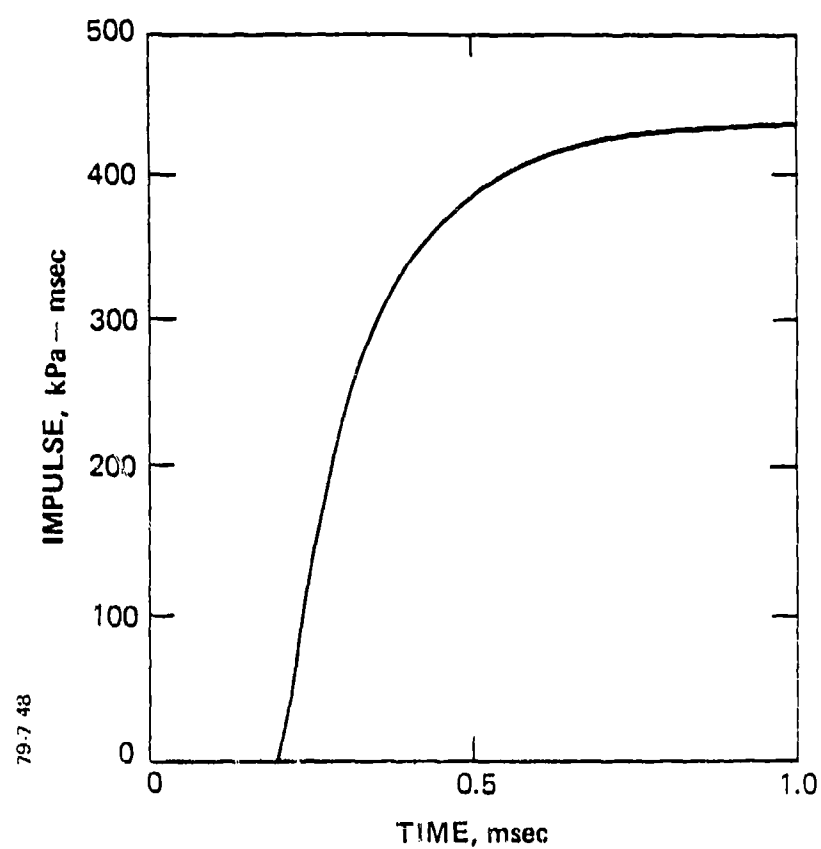


Figure A-14 Impulse at 1.33 m (6 ft) station, Test 19.

79-7463

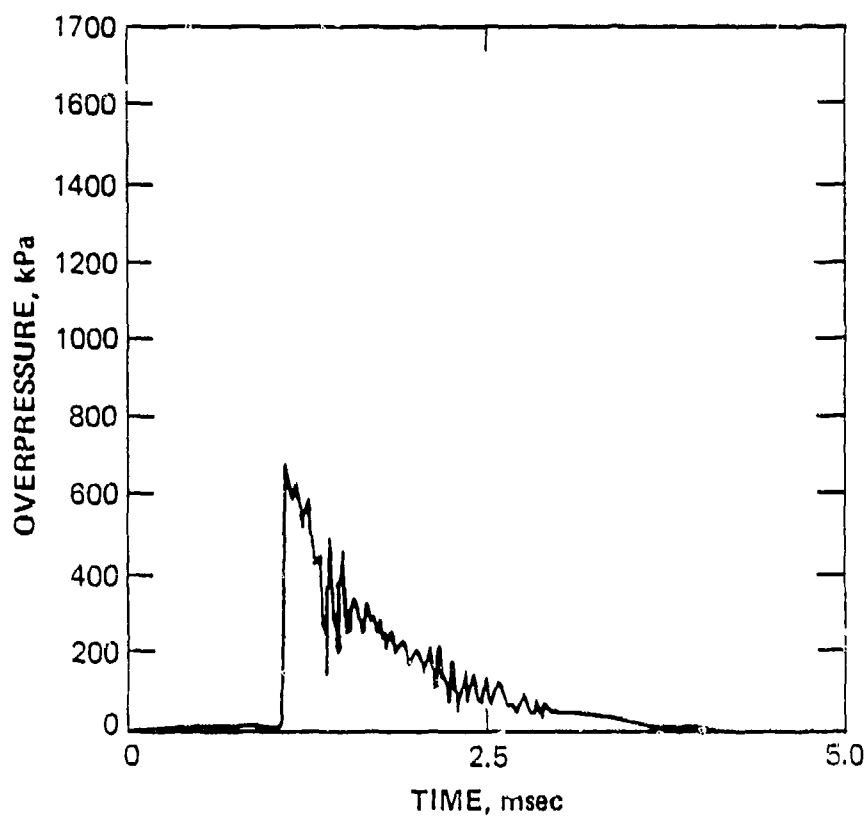


Figure A-15 Overpressure at 3.66 m (12 ft) station, Test 19.

5

79 / 42

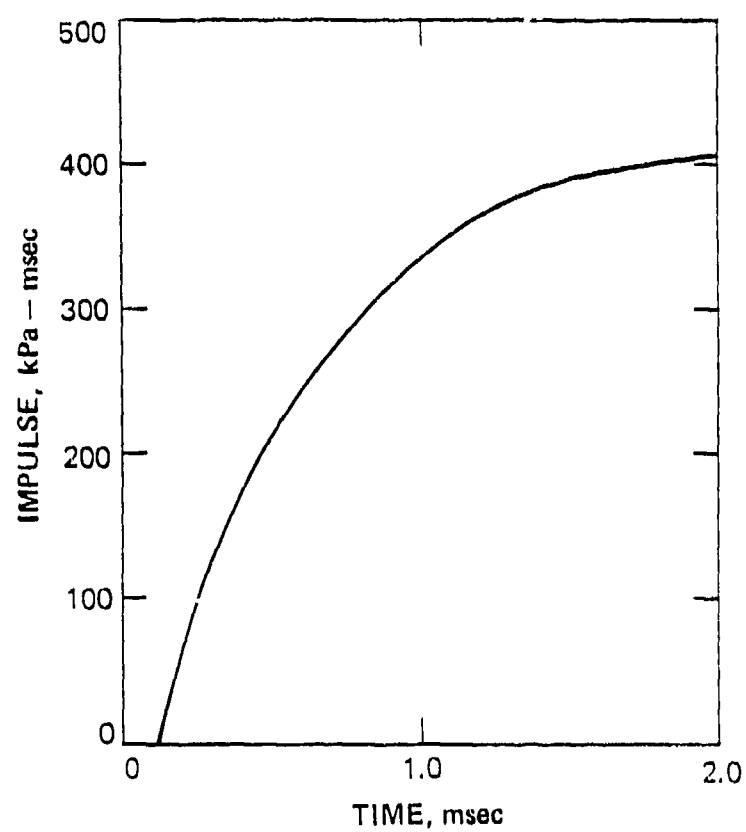


Figure A-16 Impulse at 3.66 m (12 ft) station, Test 19.

79. / 47

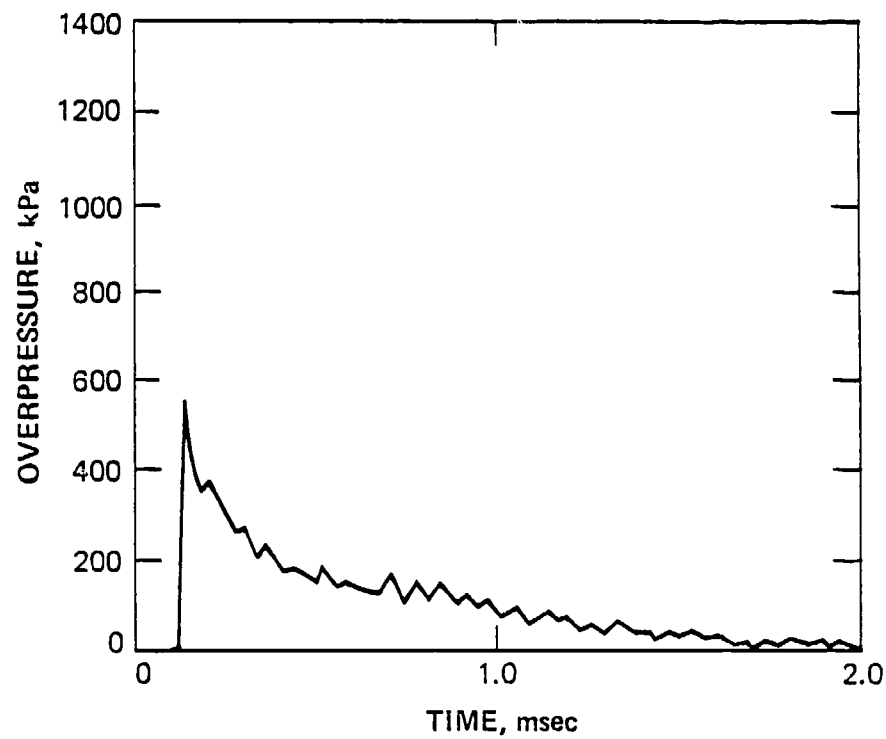


Figure A-17 Overpressure at 4.57 m (15 ft) station, Test 19.



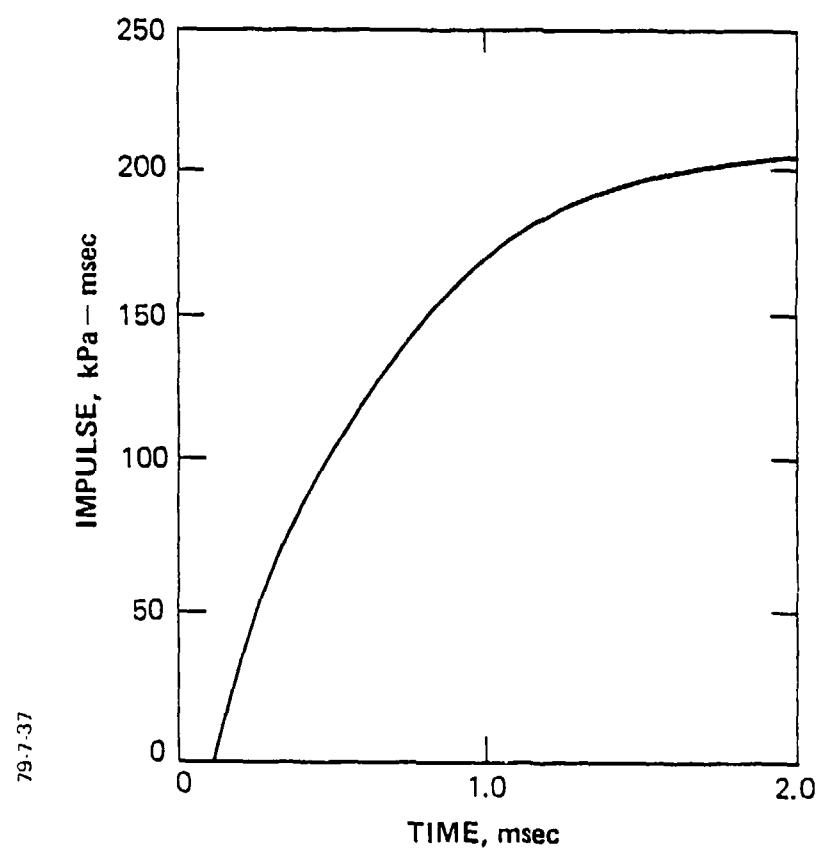


Figure A-18 Impulse at 4.57 m (15 ft) station, Test 19.

79.7.40

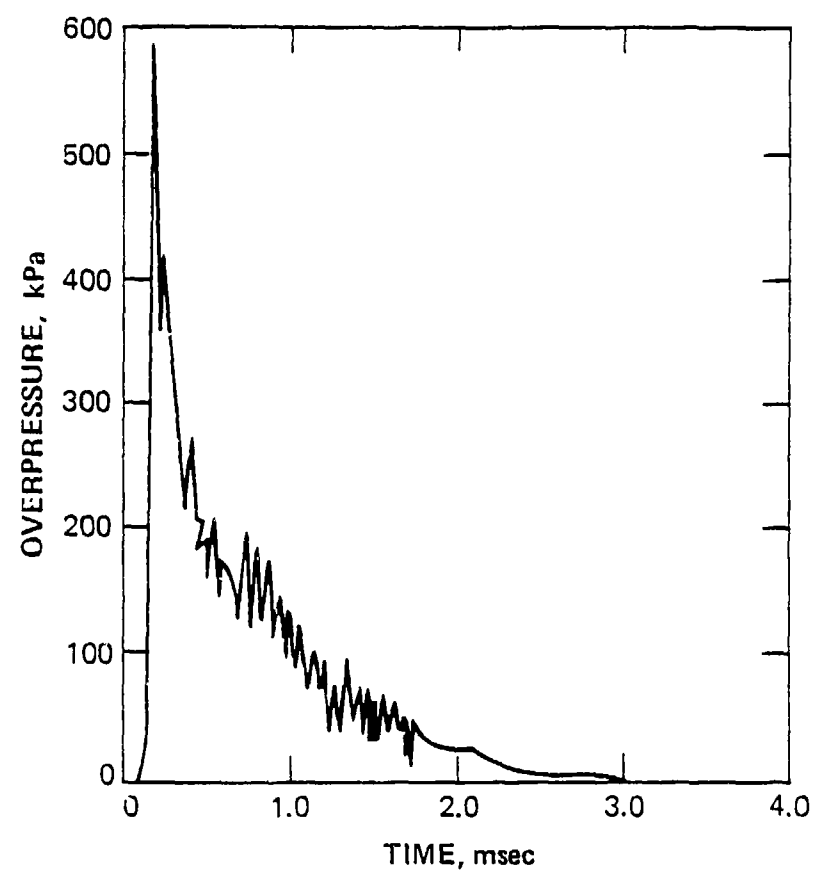


Figure A-19 Overpressure at 4.57 m (15 ft) station, Test 19.

79.760

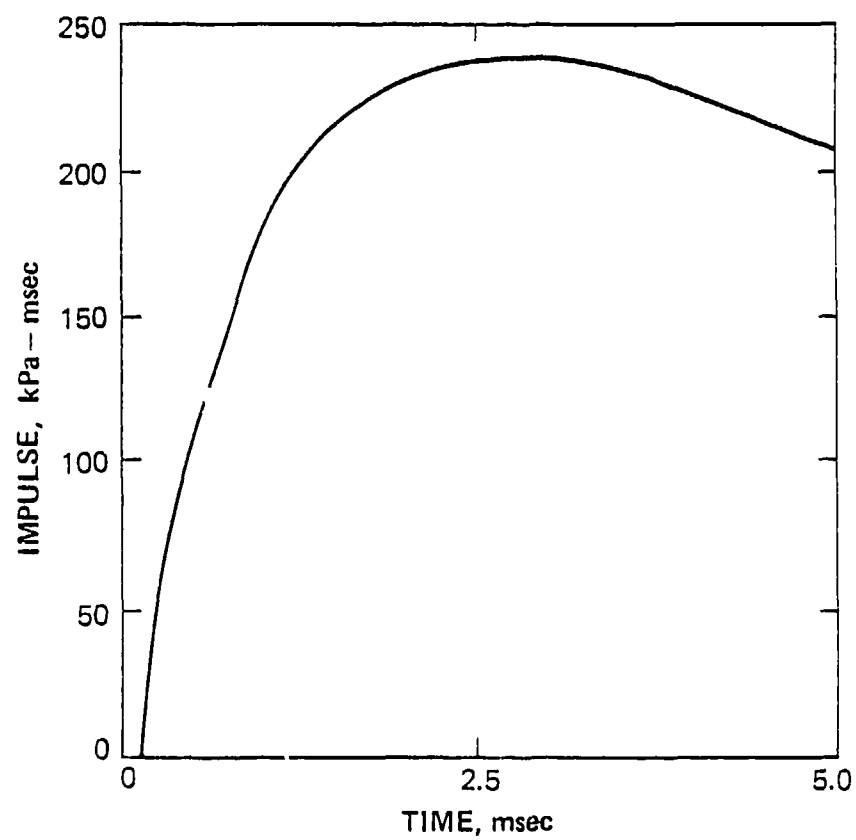


Figure A-20 Impulse at 4.57 m (15 ft) station, Test 19.

79.7.50

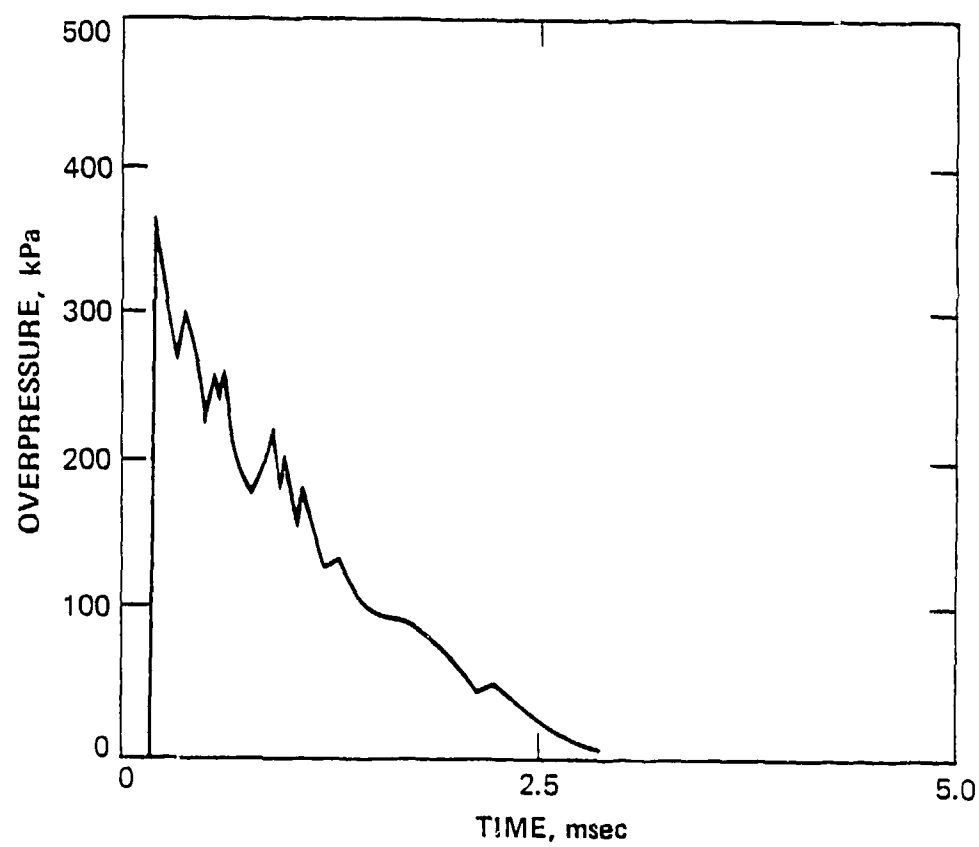


Figure A-21 Overpressure at 5.49 m (18 ft) station, Test 19.

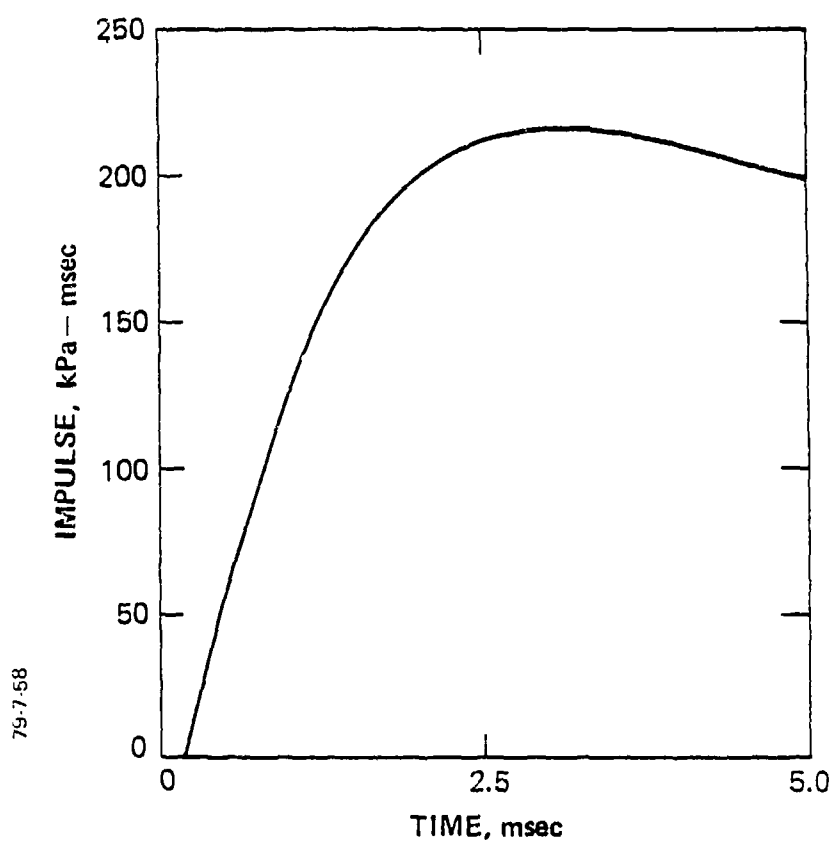


Figure A-22 Impulse at 5.49 m (18 ft) station, Test 19.

79.7.44

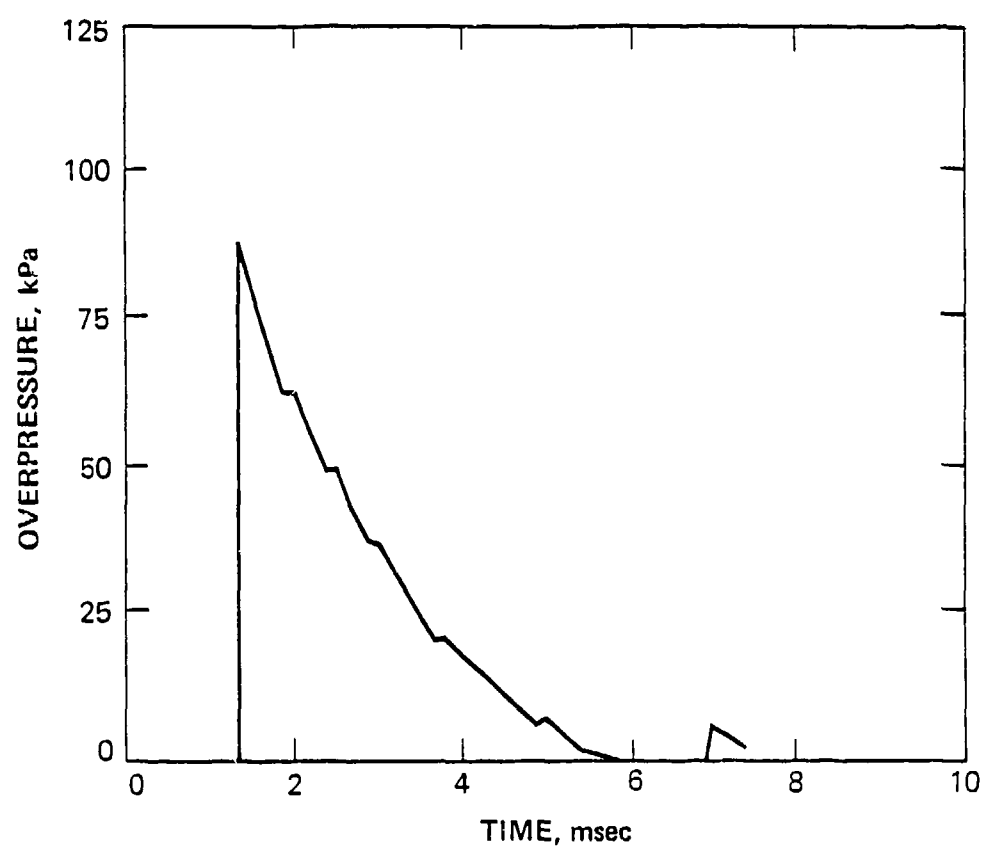


Figure A-23 Overpressure at 8.53 m (28 ft) station, Test 19.

79 7.49

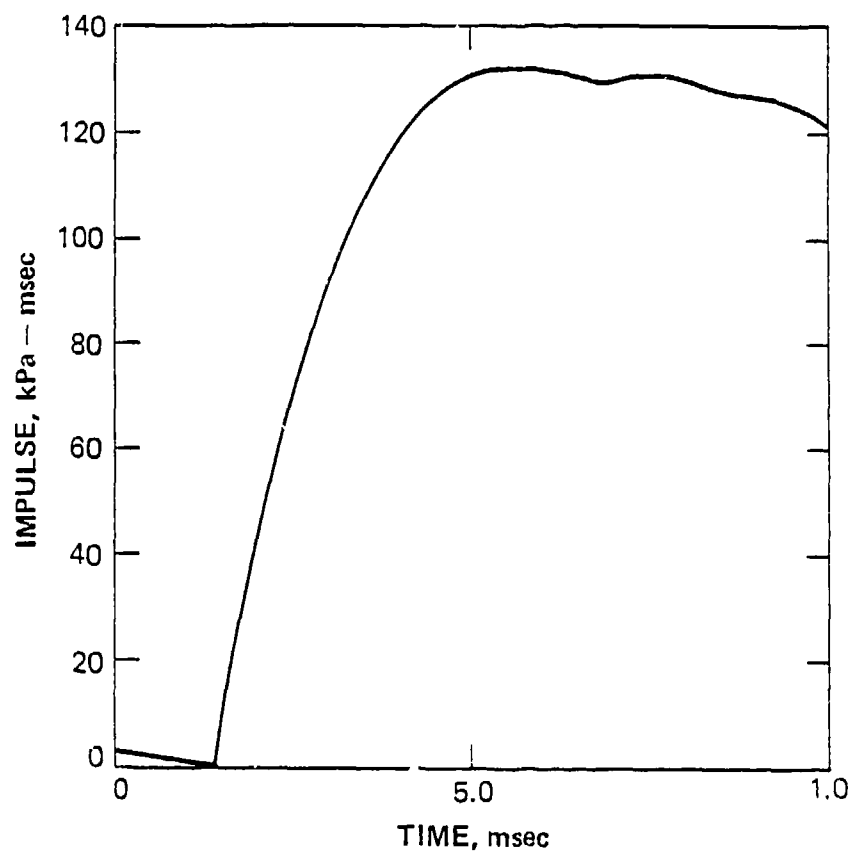


Figure A-24 Impulse at 8.53 m (28 ft) station, Test 19.

79743

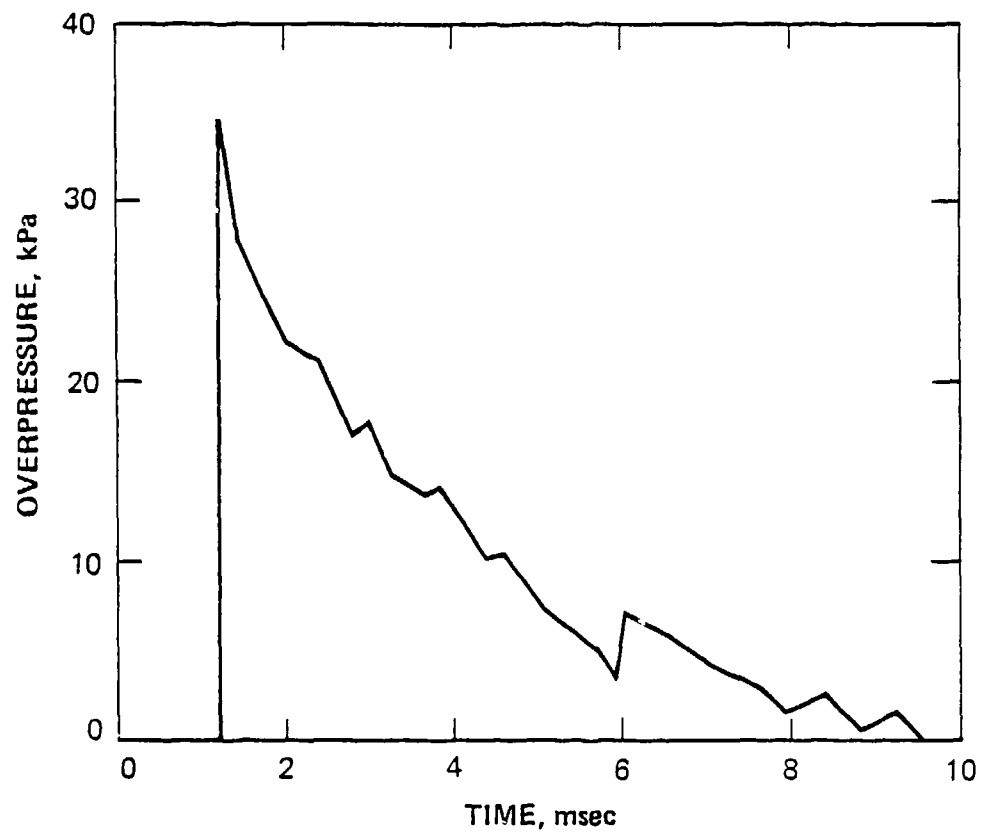


Figure A-25 Overpressure at 13.1 m (43 ft) station, Test 19.



79-7-56

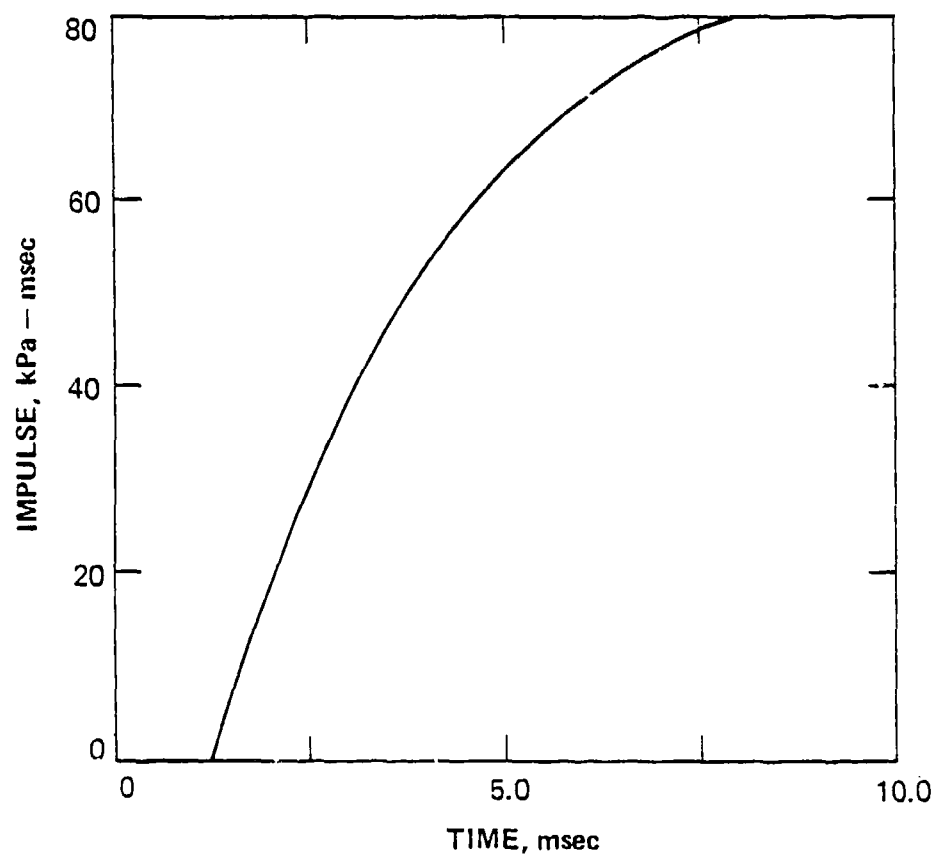


Figure A-26 Impulse at 13.1 m (43 ft) station, Test 19.

## DISTRIBUTION LIST

### DEPARTMENT OF DEFENSE

Assistant to the Secretary of Defense  
Atomic Energy  
ATTN: Executive Assistant

Defense Advanced Rsch. Proj. Agency  
ATTN: TIO

Defense Intelligence Agency  
ATTN: DB-4C, E O'Farrell  
ATTN: DT-1C  
ATTN: DT-2  
ATTN: DB-4N

Defense Nuclear Agency  
ATTN: SPTD  
2 cy ATTN: SPSS  
4 cy ATTN: TITL

Defense Technical Information Center  
12 cy ATTN: DD

Department of Defense Explo. Safety Board  
ATTN: Chairman

Field Command  
Defense Nuclear Agency  
ATTN: FCTMOF  
ATTN: FCT  
ATTN: FCPR  
ATTN: FCTK

Field Command  
Defense Nuclear Agency  
Livermore Division  
ATTN: FCPRL

Field Command Test Directorate  
Defense Nuclear Agency  
ATTN: FCTC

Interservice Nuclear Weapons School  
ATTN: TTV

Joint Strat. Tgc. Planning Staff  
ATTN: JLA  
ATTN: NRI-STINFO Library

NATO School (SHAPE)  
ATTN: U.S. Documents Officer

Undersecretary of Defense for Rsch. & Engrg.  
ATTN: Strategic & Space Systems (OS)

### DEPARTMENT OF THE ARMY

BMD Advanced Technology Center  
Department of the Army  
ATTN: 1CRDABH-X  
ATTN: ATC-T

Chief of Engineers  
Department of the Army  
ATTN: DAEN-MCE-D  
ATTN: DAEN-RDM

### DEPARTMENT OF THE ARMY (Continued)

Deputy Chief of Staff for Ops. & Plans  
Department of the Army  
ATTN: MOCA-ADL

Harry Diamond Laboratories  
Department of the Army  
ATTN: DELHD-N-P  
ATTN: DELHD-I-TL

U.S. Army Ballistic Research Labs  
ATTN: DRDAR-TSB-S  
ATTN: DRDAR-BLT, W. Taylor  
ATTN: DRDAR-BLE, J. Keefer  
ATTN: DRDAR-BLV

U.S. Army Engineer Center  
ATTN: DT-LRC

U.S. Army Engineer Div., Huntsville  
ATTN: HNDED-SR

U.S. Army Engineer Div., Ohio River  
ATTN: ORDAS-L

U.S. Army Engr. Waterways Exper. Station  
ATTN: WESSE, L. Ingram  
ATTN: J. Strange  
ATTN: WESSD, G. Jackson  
ATTN: Library  
ATTN: WESSA, W. Flathau

U.S. Army Material & Mechanics Rsch. Ctr.  
ATTN: Technical Library

U.S. Army Materiel Dev. & Readiness Command  
ATTN: DRXAM-TL

U.S. Army Missile Command  
ATTN: RSIC

U.S. Army Mobility Equip. R&D Command  
ATTN: DRDME-WC

U.S. Army Nuclear & Chemical Agency  
ATTN: Library

XVIII Airborne Corps  
Department of the Army  
ATTN: F. Ford

### DEPARTMENT OF THE NAVY

David Taylor Naval Ship R&D Center  
ATTN: Code 1844  
ATTN: Code L42-3  
ATTN: Code 17  
2 cy ATTN: Code 1740.5, B. Whang

Naval Construction Battalion Center  
ATTN: Code LC8A  
ATTN: Code L51, R. Odello  
ATTN: Code L51, S. Takahashi

Naval Electronic Systems Command  
ATTN: PNE 117-21

DEPARTMENT OF THE NAVY (Continued)

Naval Facilities Engineering Command  
ATTN: Code 09M22C  
ATTN: Code 04B  
ATTN: Code 03T

Naval Material Command  
ATTN: MAT 08T-22

Naval Postgraduate School  
ATTN: Code 0142 Library

Naval Research Laboratory  
ATTN: Code 8440, G. O'Hara  
ATTN: Code 2627

Naval Sea Systems Command  
ATTN: SEA-0351  
ATTN: SEA-09G53  
2 cy ATTN: SEA-322

Naval Surface Weapons Center  
ATTN: Code F31  
ATTN: Code R14  
ATTN: Code R14, I. Blatstein

Naval Surface Weapons Center  
ATTN: Tech. Library & Info. Services Branch

Naval War College  
ATTN: Code E-11

Naval Weapons Evaluation Facility  
ATTN: Code 10

Office of Naval Research  
ATTN: Code 474, N. Perrone  
ATTN: Code 715

Office of the Chief of Naval Operations  
ATTN: OP 981  
ATTN: OP 03EG

Strategic Systems Project Office  
Department of the Navy  
ATTN: NSP-43  
ATTN: NSP-272

DEPARTMENT OF THE AIR FORCE

Air Force Geophysics Laboratory  
ATTN: LWW, K. Thompson

Air Force Institute of Technology  
ATTN: Library

Air Force Systems Command  
ATTN: DLW

Air Force Weapons Laboratory  
Air Force Systems Command  
ATTN: SUL  
ATTN: NTE, M. Plamondon  
ATTN: DYT  
ATTN: NTES-C, R. Henny  
ATTN: DEX

Assistant Chief of Staff  
Intelligence  
Department of the Air Force  
ATTN: INT

DEPARTMENT OF THE AIR FORCE (Continued)

Ballistic Missile Office  
Air Force Systems Command  
ATTN: MMH

Deputy Chief of Staff  
Research, Development, & Acq.  
Department of the Air Force  
ATTN: AFRDQSM

Deputy Chief of Staff  
Logistics & Engineering  
Department of the Air Force  
ATTN: LEEB

Foreign Technology Division  
Air Force Systems Command  
ATTN: NIIS Library

Rome Air Development Center  
Air Force Systems Command  
ATTN: TSLD

Strategic Air Command  
Department of the Air Force  
ATTN: NRI-STINFO Library

DEPARTMENT OF ENERGY

Department of Energy  
Albuquerque Operations Office  
ATTN: CTID

Department of Energy  
ATTN: OMA/RD&T

Department of Energy  
Nevada Operations Office  
ATTN: Mail & Records for Tech. Library

DEPARTMENT OF ENERGY CONTRACTORS

Lawrence Livermore Laboratory  
ATTN: Technical Info. Dept. Library  
ATTN: L-96, L. Woodruff  
ATTN: L-10, H. Kruger  
ATTN: W. Crowley  
ATTN: J. Nutt

Los Alamos Scientific Laboratory  
ATTN: G. Spillman  
ATTN: R. Bridwell  
ATTN: M. Henderson  
ATTN: MS 362 Librarian

Oak Ridge National Laboratory  
ATTN: Central Research Library  
ATTN: Civil Def. Res. Proj.

Sandia Laboratories  
Livermore Laboratory  
ATTN: Library & Security Classification Div.

Sandia Laboratories  
ATTN: A. Chabai  
ATTN: 3141

OTHER GOVERNMENT AGENCIES

Central Intelligence Agency  
ATTN: OSI/NED, J. Ingley

OTHER GOVERNMENT AGENCIES (Continued)

Department of the Interior  
Bureau of Mines  
ATTN: Tech. Lib.

Federal Emergency Management Agency  
ATTN: Hazard Eval. & Vul Red. Div.

DEPARTMENT OF DEFENSE CONTRACTORS

Acurex Corp.  
ATTN: J. Stockton

Aerospace Corp.  
ATTN: Technical Information Services

Agabian Associates  
ATTN: M. Agabian

Applied Theory, Inc.  
ATTN: J. Trulio

AVCO Research & Systems Group  
ATTN: Library A830

BDM Corp.  
ATTN: T. Neighbors  
ATTN: Corporate Library

Boeing Co.  
ATTN: Aerospace Library  
ATTN: R. Schmidt

California Research & Technology, Inc.  
ATTN: K. Kreyenhagen  
ATTN: Library  
ATTN: M. Rosenblatt  
ATTN: S. Shuster

California Research & Technology, Inc.  
ATTN: D. Orpha

Calspan Corp.  
ATTN: Library

Civil Systems, Inc.  
ATTN: J. Bratton

University of Denver, Colorado Seminary  
ATTN: Sec. Officer for J. Wisotski

EG&G Washington Analytical Services Center, Inc.  
ATTN: Library

Eric H. Wang, Civil Engineering Resch. Fac.  
ATTN: N. Baum

Gard, Inc.  
ATTN: G. Neidhardt

General Electric Company—TEMPO  
ATTN: DASIAC

Geocenters, Inc.  
ATTN: E. Marram

H-Tech Labs, Inc.  
ATTN: B. Hartenbaum

IIT Research Institute  
ATTN: Documents Library

DEPARTMENT OF DEFENSE CONTRACTORS (Continued)

Institute for Defense Analyses  
ATTN: Classified Library

JAYCOR  
ATTN: H. Linnerud

Kaman Avidyne  
ATTN: Library  
ATTN: E. Criscione

Kaman Sciences Corp.  
ATTN: Library

Lockheed Missiles & Space Co., Inc.  
ATTN: Technical Library  
ATTN: T. Coers  
ATTN: Technical Information Center

Lockheed Missiles & Space Co., Inc.  
ATTN: TIC-Library

Lovelace Biomedical & Envir. Research Inst., Inc.  
ATTN: D. Richmond

McDonnell Douglas Corp.  
ATTN: R. Halprin

Merritt CASES, Inc.  
ATTN: Library  
ATTN: J. Merritt

Nathan M. Newmark Consult. Eng. Svcs.  
ATTN: N. Newmark

University of New Mexico  
ATTN: CERF, G. Leigh  
ATTN: CERF, N. Baum

Pacific-Sierra Research Corp.  
ATTN: H. Brode

Pacifica Technology  
ATTN: J. Kent  
ATTN: R. Allen

Physics Applications, Inc.  
ATTN: F. Ford

Physics International Co.  
ATTN: E. Moore  
ATTN: F. Sauer  
ATTN: J. Thomsen  
ATTN: L. Behrmann  
ATTN: Technical Library  
ATTN: R. Franzen

R & D Associates  
ATTN: C. MacDonald  
ATTN: R. Port  
ATTN: A. Latter  
ATTN: J. Carpenter  
ATTN: Technical Information Center  
ATTN: W. Wright, Jr.  
ATTN: J. Lewis

Science Applications, Inc.  
ATTN: Technical Library  
ATTN: H. Wilson

DEPARTMENT OF DEFENSE CONTRACTORS (Continued)

Science Applications, Inc.  
ATTN: J. Dishon

Science Applications, Inc.  
ATTN: D. Bernstein  
ATTN: D. Maxwell

Science Applications, Inc.  
ATTN: M. Knasel

Southwest Research Institute  
ATTN: A. Wenzel  
ATTN: W. Baker

SRI International  
ATTN: G. Abrahamson  
ATTN: G. Gasten

Systems, Science & Software, Inc.  
ATTN: T. Riney  
ATTN: K. Pyatt  
ATTN: Library  
ATTN: R. Lafrenz  
ATTN: D. Grine  
ATTN: T. Cherry

TRW Defense & Space Sys. Group  
ATTN: L. Wong

DEPARTMENT OF DEFENSE CONTRACTORS (Continued)

Terra Tek, Inc.  
ATTN: S. Green  
ATTN: Library

Tetra Tech, Inc.  
ATTN: Library  
ATTN: L. Hwang

TRW Defense & Space Sys. Group  
ATTN: I. Alber  
ATTN: R. Plebuch  
ATTN: Technical Information Center  
ATTN: D. Baer  
ATTN: P. Dai

Universal Analytics, Inc.  
ATTN: E. Field

Weidlinger Assoc., Consulting Engineers  
ATTN: J. Wright  
ATTN: M. Baron

Weidlinger Assoc., Consulting Engineers  
ATTN: J. Isenberg

Westinghouse Electric Corp.  
ATTN: W. Volz